Universidad Carlos III de Madrid
Escuela Politécnica Superior
Aerospace Engineering Department

Aerospace Engineering
Bachelor Thesis

Redesign of the Rotor Head of the C30 Autogyro

Author
Jose Barranco Alba

Supervisor
Pablo Fajardo Peña

September 2018

Abstract

Asociación Juan de la Cierva Codorníu (AJCC) is devoted to the reconstruction of a commemorative replica of the C.30 autogiro to be flown in national aeronautic exhibitions. In collaboration with the association, the present project focusses on two tasks: the research on a material for the disc of the blade friction damper and the design of a model that reproduces the blade motion in the steady forward flight.

A number of candidate materials proposed are ranked according a figure of merit (FoM) which balances thermo-mechanical properties with an index of performance (IoP) and cost. The technique used to weight the properties is a modification of the classical digital logic (DL) method. Mainly aluminium alloys show the optimum balance to manufacture the damper friction disc.

The blade motion, simulated for the steady forward flight (auto-rotation), makes use of Euler's equations for a rotating rigid body. The main assumptions rely on small angle approximation, flat Earth, an ideal 2D aerodynamics model and Coulomb's friction law for damping. The results show the two motions inherently lagged by 90° and absolute compatibility with the theoretical formulation by means of Fourier's series. Simulations are numerically run at eight different airspeeds along the C.30 range of operation. As the inertial forces become dominant over the aerodynamic forces, the amplitude of both motions asymptotically tends to zero. The results render faithfully the blade cyclic motions of the C.30 autogiro under steady forward flight when compared with experimental results.

Acknowledgements

After a few years, today is the day. I find myself reaching the finish line, typing the lines that close my bachelor thesis and conclude a great life feat called University. Academically and personally, the intensive learning period has had a strong impact on myself and I would like to express my gratitude to all those who gave their support.

In the first place, I must thank Universidad Carlos III de Madrid and all the professors. Particularly, I am indebted to my tutor, Pablo Fajardo, who guided me through the project, and to Óscar Flores for his help and involvement. I would also like to blink an eye to Salomé for her assistance in the moments of trouble. It is not in vane that I could not have defended this thesis without her help and the collaboration of Oficina de Alumnos.

It is a honour participating in the ambitious and commemorative project *Juanito C.30* promoted by Asociación Juan de la Cierva Codorníu (AJCC). I cannot forget about another important entity: 2Fly Aerodynamics, the aviation academy in Málaga where I spent a summer doing a professional internship. They made me feel home and taught me about numerous aspects of aviation from the deepest approach.

To Juanma for designing together the most spectacular pedal-car ever. To Alberto for our masterpiece ´chocolate-bar-table', the outstanding spinning-top tip logistics and his unique helicopter demos. To Andrés for his broad knowledge about beer and rest. To Roberto for his distinctive philosophy of life and his endless provision of board games. I had promised to pay especial attention to Álvaro for his dedication those countless times I needed a hand. To all together and the rest of friends and colleagues who made me feel lucky thanks to their generosity, their attention and their teamwork not only as classmates, but as football players too. What those joyful and challenging times as a team with Olympique del Ion and Colonos del Cartojal. To the Queensland University of Technology and the ones who I crossed paths with during my student exchange in Australia. Thanks to all for the trips together and for the moments of fun.

But all my trajectory would not have been possible without my family. I will be forever grateful to my little and only sister, whose company and advise never failed to carry me through the weakest times. Finally, I owe my deepest gratitude to the best teacher in my life: dad. Because everything I am, I owe to him. Despite the distance, his support in every decision I take never ceases. His love is my best luck.

Contents

List of Figures

List of Tables

List of Symbols

A_c	Contact area between washer and disc
b	Blade span
c	Blade chord
C_d	Coefficient of drag (polar)
C_l	Coefficient of lift of blade aerofoil
F_{comp}	Compressive axial force by screw on damper disc and washers
D'	Drag of blade aerofoil
e_h	Hinge eccentricity
F_{aero}	Force by aerodynamics on blade
g	Acceleration of gravity (at SL)
$\bar{\bar{I}}_{H,4}$	Tensor of inertia of blade respect to principal axes ($Hx_4y_4z_4$)
L'	Lift of blade aerofoil
M_f	Moment by friction of damper
R	Radius of disk (length from rotation axis to blade tip)
R_i	Inner radius of washer in the damper
R_o	Outer radius of washer in the damper
S	Pressure or stress of washer on a disc side
S_m	Compression strength of material
t	Blade thickness
U_∞	Free air-stream velocity
α_b	Angle of attack (locally) at each blade section
α	Air velocity angle of rotor disc plane with horizontal (aircraft AoA)
β	Blade flapping angle
β_s	Air velocity angle from horizontal projection to span-axis (sideslip)
λ	Linear density of blade along chordwise
μ	Friction coefficient of material
μ	Tip speed ratio
Ω	Rotor angular speed
Φ	Aircraft roll angle
ψ	Azimuthal angular position of hinge in rotor plane
Ψ	Aircraft yaw angle
σ	Planar density of blade cross section
θ	Blade pitch angle
Θ	Aircraft pitch angle
ξ	Blade lagging angle

List of Abbreviations

AESA	Agencia Estatal de Seguridad Aérea
AJCC	Asociación Juan de la Cierva Codorníu
Al	aluminium
AoA	angle of attack
AW	airworthiness
BET	blade element theory
C	carbon
CA	civil aviation
CoM	center of mass
Cr	chromium
DAE	differential algebraic equation
DL	digital logic
DoF	degree of freedom
EoM	equation of motion
FAI	Fédération Aéronautique Internationale
Fe	iron
FoM	figure of merit
Gö	Göttingen
ICAO	International Civil Aviation Organization
IoP	index of performance
ISA	international standard atmosphere
JAA	Joint Aviation Authorities
JAR	Joint Aviation Requirements
KFM	kynetic friction model
MDL	modified digital logic
Mo	molibdenum
MoI	moment of inertia

MTOM	maximum take-off mass
ODE	ordinary differential equation
SL	sea level
TAT	thin aerofoil theory
TC	type certificate
Ti	titanium
WPM	weighted properties method
WWII	World World II

"*My advice is: keep your lips away from the spinning things.*"

– Adam Savage

1 Introduction

1.1 Background & Motivation

In commemoration to the centenary of Juan de la Cierva's prestigious invention, Asociación Juan de la Cierva Codorníu (AJCC) develops the project *Juanito C.30*, which aims for the reconstruction of a replica of the well known Cierva C.30 Autogiro. Leaded by his great-granddaughter, Laura de la Cierva, the ambitious project aims to "honour" the Spanish inventor taking the first gyroplane ever to the national air shows, "letting people enjoy such a fantastic creation". They hope to build the most reliable copy with renovated mechanisms that ensure and improve safety in performance, keeping faithfulness to the aesthetics and design of the time.

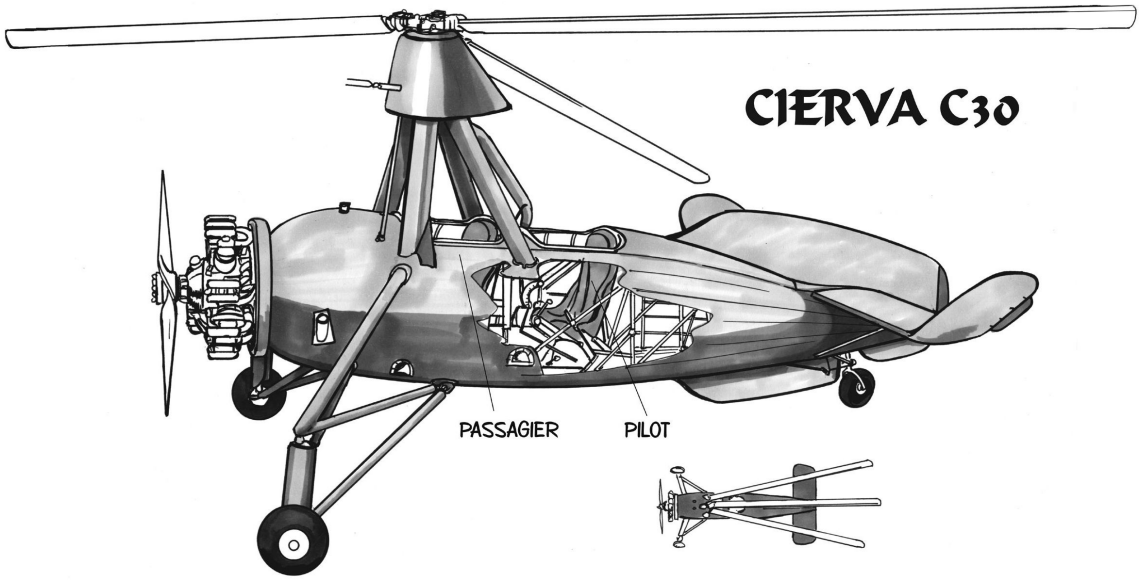

Figure 1.1: Sketch of Juan de la Cierva's C.30 Autogiro [W23].

This project focusses on the **research on the friction damper disc material of the Cierva C.30 Autogiro and simulation of the blade dynamics in flight**. With official documentation and design constrains, the friction damper that the system includes will be redesigned by selecting the appropriate disc material and tested upon validation through a model that simulates its performance in flight.

The following subsections provide a contextualisation of the matter and a brief history review.

1.1.1 The Autogiro: Introduction & Comparison with Similar Aircraft

The *autogiro* (also known as *gyroplane* or *gyrocopter*) is a rotary wing aircraft. As a heavier-than-air vehicle, it must find the way to push itself upwards. Indeed, it flies like a common aeroplane. The difference lies on the rotating blades aerodynamically powered by the relative wind going through. The gyroplane can manage without fixed-wings and it is considered as a hybrid between an aeroplane and a helicopter: propelled horizontally by an engine, as the former, and vertically by a rotor, as the latter. Not connected to the engine in flight, the rotor is free to rotate driven by the aerodynamic forces that generate a lifting force. The helicopter, in contrast, makes use of the rotor to get both propulsion and lift.

Low flying speeds are feasible, but the gyrocopter cannot eventually stop its motion to stand still up in the air (hovering). It is a safe aircraft, having a critical moment: after landing, while the rotation has not ceased yet, strong wind gusts can lift it up again.

In the event of an engine failure, the autogiro glides and descends slowly (auto-rotation). The faster the free fall, the faster spinning of the rotor, storing more energy and providing higher lift. In a similar fashion, a helicopter is able to land in an emergency by means of auto-rotation, but the clutch mechanism must be first disengaged in order to completely release the engine from the rotor head and the blade pitch must be modified too. In contrast, the gyroplane always flies under the auto-rotation principle.

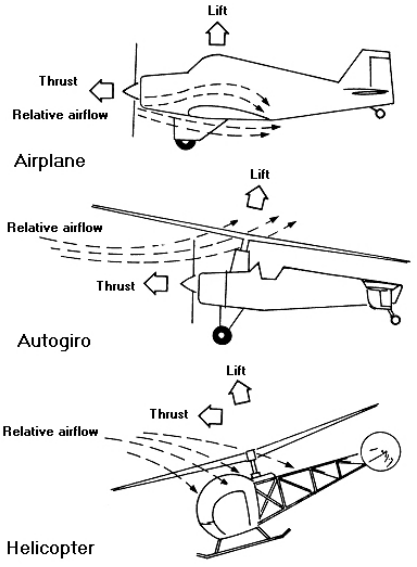

Figure 1.2: Comparison with aeroplane & helicopter [W14].

1.1.2 History Review

The author George Townson presents a history review in his book *Autogiro. The Story of the Windmill Plane* [21], elaborating on the mechanics involved. The next lines in the section allude to the historical framework based on this work.

Invented by the Spanish engineer Juan de la Cierva, the first attempts to lift the autogiro took place in 1920. But it was in 1923 when the invention could fly up to 200 metres. Later, in 1924, the first flight between two aerodromes (Getafe and Cuatro Vientos, Madrid) took place.

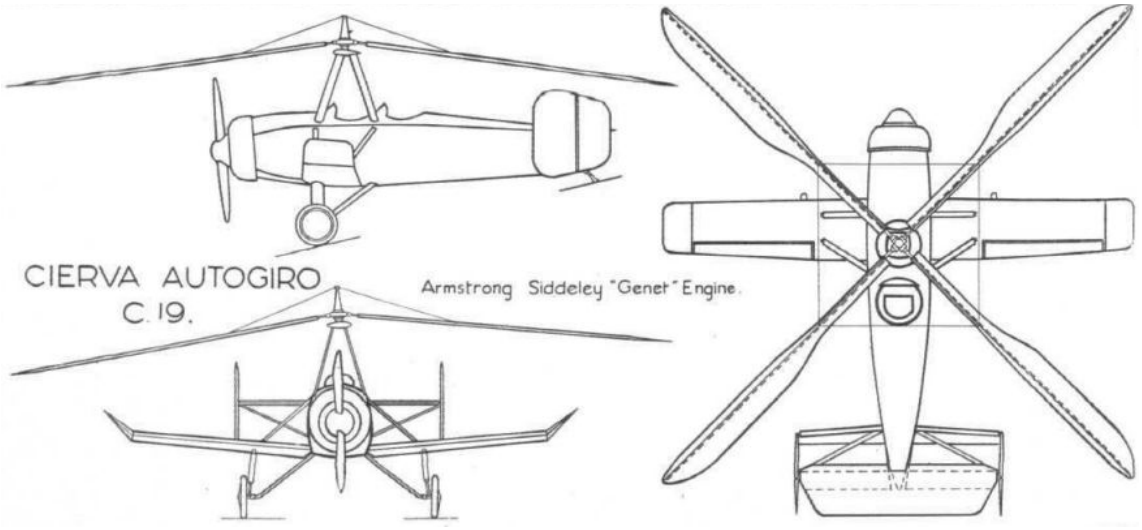

Figure 1.3: Juan de la Cierva's Autogiro C.19 [W2].

The first models included small wings that helped controlling the rolling moment. As the advances progressed, the Spanish engineer developed the articulated rotor head, which gave the blades two extra degrees of freedom (DoFs). They would present now two oscillatory motions: lagging and flapping. It meant a revolutionary concept at that time that solved the problem of asymmetry in the lift distribution of the rotor disc, preventing the aircraft from rolling over and crashing. A friction damper installed also helped stabilise the oscillations through the lagging motion. Together with the direct control on the attitude, these improvements would take the invention a step further and the original small wings were eventually removed.

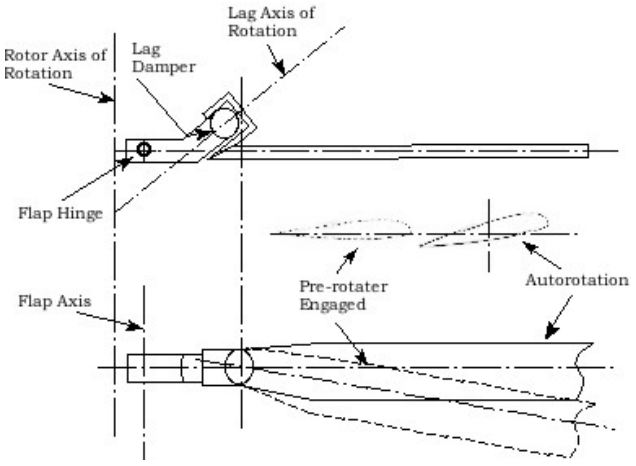

Figure 1.4: Improvement for the latest models take-off: inclination of lag axis [W8].

Other improvements involved pre-rotation through an ad hoc system, decreasing the take off run up to the 'jump take-off', which was practically vertical. More advanced models were equipped with the 'auto-dynamic' rotor head, introducing an angle to the lag axis with respect to the vertical (depicted in fig. 1.4) that would ensure 'fine pitch' until reaching the right speed and disengaging the clutch system from the engine. At this moment, the blades would move in lagging motion increasing the angle of attack (AoA) and generating the lift needed for the jump take-off.

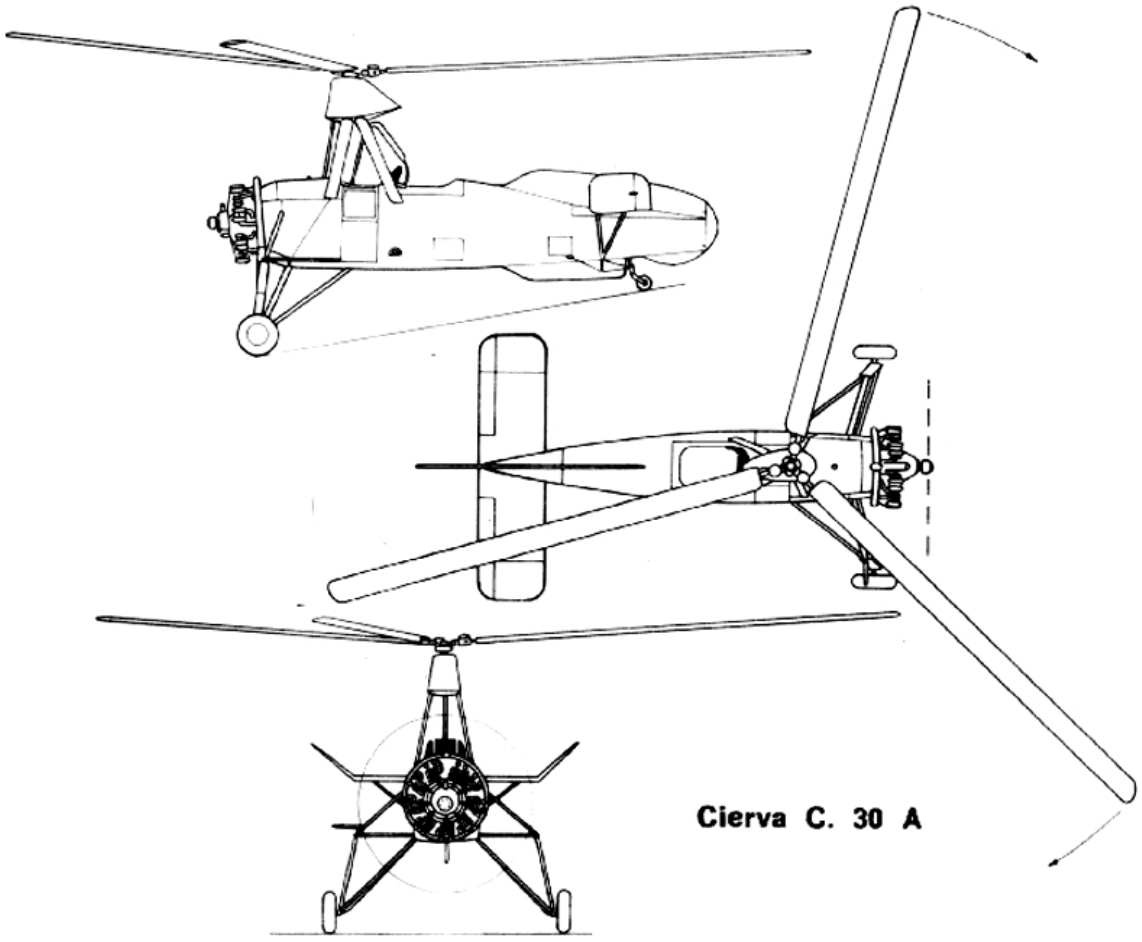

Figure 1.5: Juan de la Cierva's Autogiro C.30 [W3].

As a curious fact, Juan de la Cierva was not especially interested in helicopters; he considered them "quite complex to fly and prone to accidents". However, with the beginning of helicopters came the decline of gyrocopters, until near extinction. In the present, sport aviation has boosted the autogiro.

1.2 Goals & Objectives

The principal objective of the project will be the material selection for the friction damper disc of the C.30 autogiro. Through literature and documentation, different materials will be researched as a starting point and a specific procedure will be defined to evaluate them. Once chosen according to the project constrains, the blade dynamics in flight will be modelled with the purpose of checking the validity and studying the two motions involved —namely flapping and lagging—.

Two distinctions will be made according to the goals and the objectives in the next few lines. The objectives of the project are the target points, at a task level, that represent the endeavoured steps with the main guidelines of the document. They are listed as follows:

- Analysing the project constrains and/or needs to identify the relevant properties in the process of material selection for the friction damper disc of the C.30 autogiro.
- Providing a quantitative method that allows the material selection based on the parameters involved and the identified properties.
- Selecting the optimal material for the friction damper disc according to the criteria established.
- Creating a model for the simulation of the blade dynamics to study the motion in straight forward flight.
- Validating the performance of the the material selected after numerical computation and comparing with existing experimental results.

And the goals, at an academic level, describe the competences and skills expected to be learned by the end of the project. They are described as follows:

- Learning to collect, filter and process information to implement the correct methodology, to present and elaborate on results and to write a bachelor thesis.
- Researching through literature and official documents to obtain valuable information, data, constrains and parameters involved in the problem.
- Understanding the limitations due to technological means that fall behind in time and searching for new, more advanced, ways to approach the study.
- Cooperating with other professionals, like professors and members of the aforementioned association AJCC, discussing different points of view and defining objectives step by step during the project.

- Studying and understanding the mechanics of the articulated rotor.
- Working with numerical computation software, understanding its advantages and limitations.
- Evaluating and assessing the performance of simulation, identifying possible improvements that may be implemented and possible weaknesses that should be studied in depth.

1.3 Structure of the Document

The document is divided into six chapters detailed as follows, with a graphical representation of the most relevant sections in fig. 1.6.

Chapter 1 introduces the project subject in the first lines and includes three subsequent sections. The first one explains the concept of the autogiro and compares it to other types of aircraft. The second reviews briefly the history and the advances implemented to observe the first steps in the evolution of the invention. And the third, which correspond to the present section, describes the document structure with an explanation of each chapter.

Chapter 2 shows the literature review where the official documentation used in the study is presented. Relevant studies and existing knowledge in the matter are also referred to in the chapter as well as the socio-economic impact and governing regulations. Mainly three sections elaborate on research papers about documentation, literature review and regulatory and socio-economic frameworks.

Chapter 3 describes the selection process for the material of the friction damper disc. It is divided into five sections that consist on: explaining material properties concerned, presenting the candidate materials, defining the selection criteria, providing some calculations for the installation procedures and discussing de results.

Chapter 4 presents the process for the simulation of the blade motion. It contains six sections with content on: a summary of the assumptions, the reference frames involved, the model of dynamics proposed (split into four subjects), the equations of motion (EoMs), the software used and the discussion of the results.

Chapter 5 exposes the final conclusion of the project. Possible improvements are discussed too in the chapter for future lines of research that may arise within the present field of study.

Chapter 6 closes the document with two sections elaborating on the project planning and the budget estimation to develop the project.

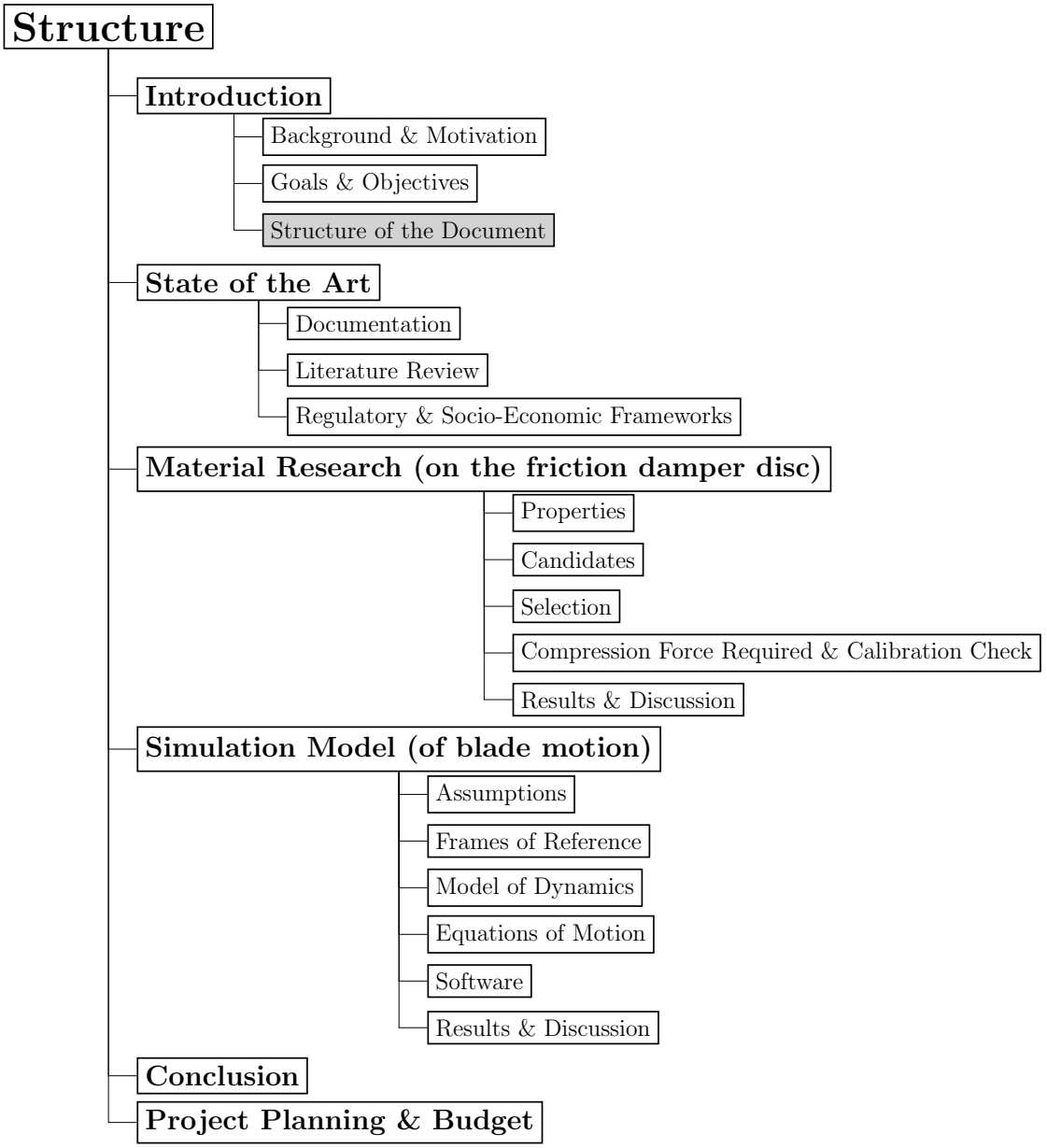

Figure 1.6: Main structure of the document.

2 State of the Art

Existing knowledge and work related to the project are grouped and referenced in the following lines, where two main categories can be distinguished. On one hand, the majority of the official documents date from the last century, one hundred years ago, and show the information and characteristics of the autogiro C.30 as well as studies made by Juan de la Cierva and other approved authors. On the other hand, as a literature review, more recent advanced studies provide different techniques to approach every part of the study.

2.1 Documentation

The research process begins with primary source documents about the autogiro C.30 MZA —approved for official use only— currently found as museum copies and supplied by AJCC. Namely guides on the use, maintenance and repair [4, 17] together with investigation papers on performance both at ground [20] and flight [3, 12], including general blade motion and experimental results. The fundamental characteristics are also found in these (mass, geometry, subsystems...) offering a broad understanding of the invention and providing reference data.

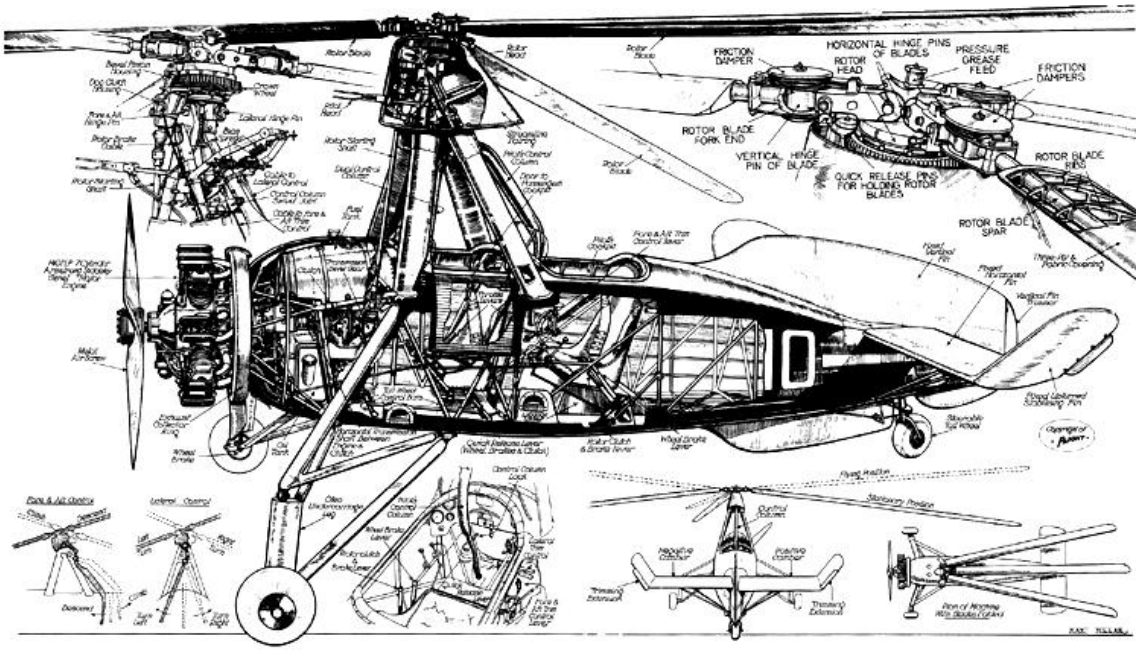

Figure 2.1: Sketch of Juan de la Cierva's autogiro C.30 and some systems [W16].

A particular procedure for the friction damper calibration deserves especial attention (cross-section illustrated in fig. 3.1 in chapter 3). As an imperative requirement, it describes the steps and defines the value of the force that must be read on the spring balance used. Quoting the instructions from the original paper [3]:

> Checking friction damper:
>
> After the three blades have been assembled the "pull off" of the friction dampers on each should be checked as follows:
>
> Put on rotor brake and lock the control column. Set the rotor to be checked in line with the fuselage, in such a position that the total movement of the blade is equally divided on each side of the centre line of the gyroplane. Next place a piece of tape round the rotor blade across the centre of the oblong recess where the balance weights are fixed, i.e. about 12 inches from the tip. The tape should be tied so that the hooked end of the spring balance supplied with the tool kit can be attached. Now move the blade over to the left to the extent of its free movement and attach the tape from the trailing edge to the spring balance which is tied or secured in any convenient manner. It will facilitate the operation now if another person will steady the rotor by taking hold of one of the other two blades. The blade being checked is gently pulled to the right and the reading of the spring balance noted. With the blade extended to the right until up against the stop, the operation should be reversed with the tape pulling off the leading edge. It will usually be found that the two readings vary slightly and the friction damper should be adjusted until the mean of the two readings is consistent at approximately 12lb. and then locked.
>
> Adjusting friction damper:
>
> Loosen the lock nut on the top of the damper and adjust by turning the bottom nut to the right to increase the pressure and to the left to decrease it. When the correct pressure has been obtained, secure the adjustment by means of the lock nut above the adjusting nut.

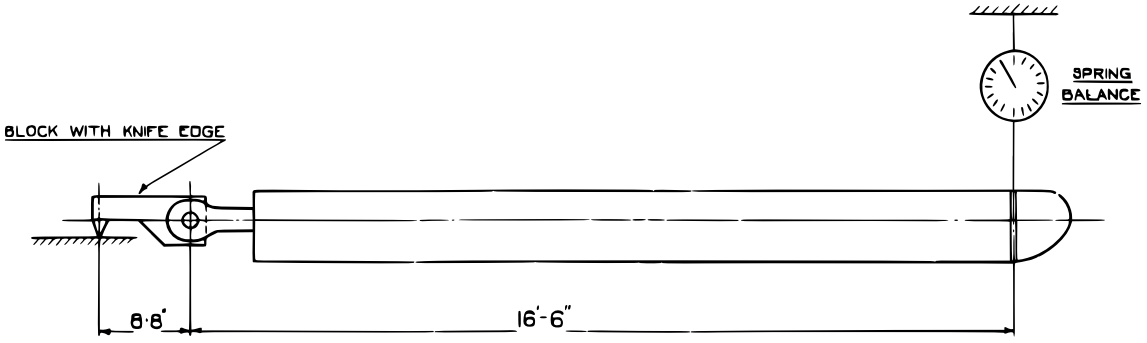

Figure 2.2: Spring balance attachment on blade tip for calibration [3].

2.2 Literature Review

2.2.1 Material Research

Different sources of information on existing materials and procedures of selection are presented in this section. The aim is collecting the relevant studies on the matter that may be used to make a decision on what material should be used to manufacture the friction damper disc.

2.2.1.1 Metallurgy of Brake Discs

Brake discs like the ones installed on a vehicle wheels work essentially under the same principles as the ones in the gyroplane blade damper: energy dissipation by friction. Concerning the metallurgy, engineers from São Paulo University have gone through the history of materials used in brake discs within the automotive, railway and aviation industries. Their paper *Development of Materials for Automotive Disc Brakes* [11] presents a theoretical background on physical and mechanical properties and the factors affecting each in the manufacturing process.

If iron (Fe) is combined in the right proportion with alloy elements, with control on the cooling speed, the micro-structure changes affecting the properties. Carbon (C) is the element that can modify the properties of Fe most significantly. Other elements may be added to improve the desired properties. For instance, molibdenum (Mo) increases mechanical strength to heat and chromium (Cr) improves corrosion and abrasion strength.

Brake discs, as the Brazilian scientists explain, work under thermo-mechanical loading, withstanding temperatures ranges from ambient temperature up to 700°C due to friction. Among a range of possible materials that comply with the demanding performance, usually carbon ceramics and (grey or ductile) cast iron (shaded region in fig. 2.3) are employed against others due to favourable balance between cost, manufacturing, metallurgical stability, vibration damping and galling[1]. However, the authors conclude that, despite being theoretical results, experimental work is needed to confirm the validity. For more reliability in the present study, as a consequence, real properties of this alloy (cast iron) should be first obtained from a materials database and compared among different additional elements and concentrations.

[1] [W10] Galling is a kind of wear that happens when two bodies under compression are set to relative motion. The heat caused by friction welds and bonds both together, removing material from one and giving it to the other. The surroundings, where the heat from friction was insufficient, may suffer abrasive wear.

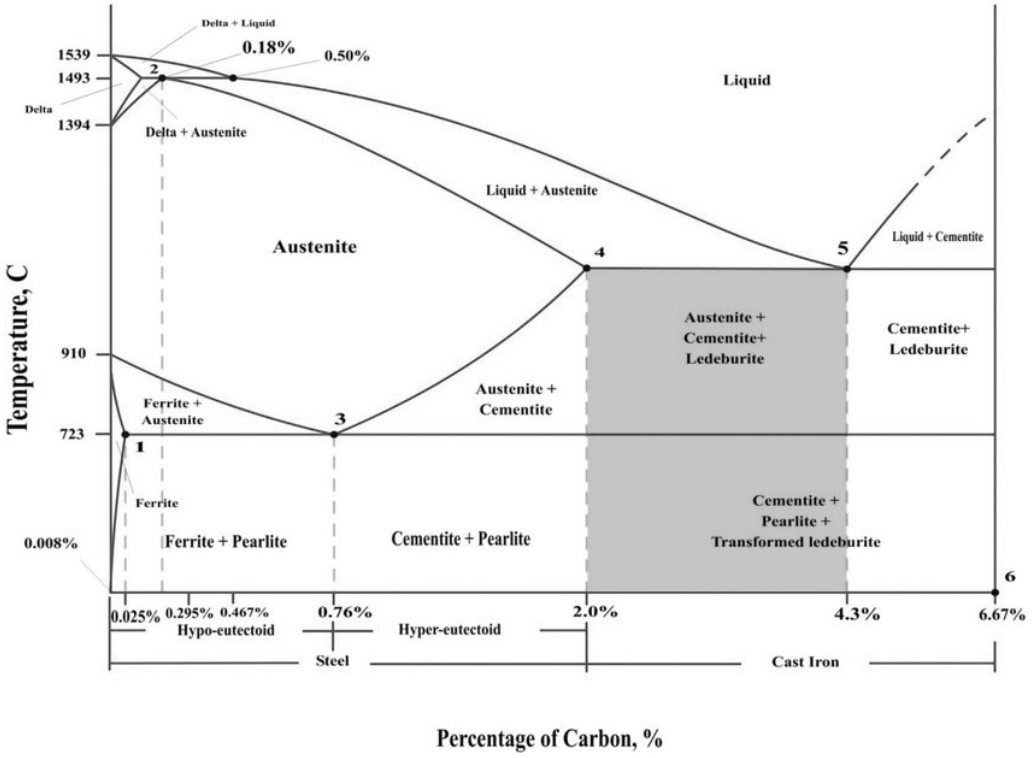

Figure 2.3: Fe-C phase diagram [W6]. Grey & ductile cast irons in shade-area.

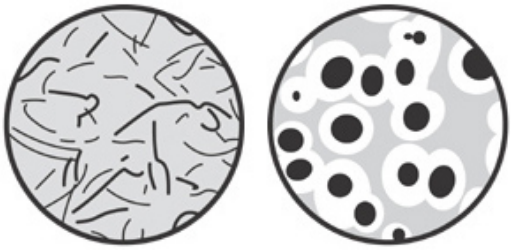

Figure 2.4: Graphite micro-structures [W25]: i) grey cast iron ii) ductile cast iron.

Aluminium (Al) alloys will be considered too as the global balance of the desired properties might eventually be favourable. They are particularly suitable for low weight and high strength applications. According to Joseph Davis in his book *Alloying: Understanding the Basics* [5], within the wrought alloys, the $8xxx$ series has improved elevated performance and they are often used in the aerospace industry, especially in helicopters. Other series like $5xxx$ and $7xxx$ might also prove a reliable performance for the desired conditions. As the author explains, the cast Al alloys have the same strengthening mechanisms and are based on the same systems: these will be more useful for the small custom production considered in this project.

2.2.1.2 Selection Criteria

A well known method to select a material in all design processes is the weighted properties method (WPM) [13]. Based on simple mathematics, it consists on defining the properties and factors (goals) affecting the performance of the piece in question and assigning a scaled value to weight the importance of each.

That way the goals involved are ranked, but the subjectivity of assigning every relative weight still remains. The digital logic (DL) method approaches the problem by reducing the subjective nature, making the selection criteria more objective or quantitative. It compares all the goals by pairs, giving a logical value depending on the importance: 1 to the most and 0 to the least. In the paper *A novel method for materials selection in mechanical design: Combination of non-linear normalization and a modified digital logic method* [7], engineers claim that the DL method can be improved for accuracy. Because the least important goal is expelled from the decision process, they offer the modified digital logic (MDL) technique that plays with three values according to the importance: 3 to the most, 1 to the least and 2 in case of similarity. A scale factor is finally applied, as the relative weights are usually scaled in the basis of unity.

Goals	**Possible Decisions** $[N = \frac{\sum n_i(\sum n_i - 1)}{2} = 10]$										**Positive Decisions**	**Relative Weight**
$[n_i]$	1	2	3	4	5	6	7	8	9	10	$[N_i^+]$	$[\alpha_i = \frac{N_i^+}{N}]$
A	1 (3)	1 (3)	1 (3)	0 (2)							3 (11)	**0.3 (0.275)**
B	0 (1)				0 (1)	0 (1)	0 (1)				0 (4)	**0.0 (0.100)**
C		0 (1)			1 (3)			1 (2)	0 (1)		2 (7)	**0.2 (0.175)**
D			0 (1)			1 (3)		0 (2)		0 (1)	1 (7)	**0.1 (0.175)**
E				1 (2)			1 (3)		1 (3)	1 (3)	4 (11)	**0.4 (0.275)**
$\sum n_i = 5$											$\sum N_i^+ = 10$ (40)	$\sum \alpha_i = 1$ (1)

Table 2.1: Comparison between DL & (MDL) methods [7].

This model will be used later on in the selection process of the material for the friction damper disc. The authors also regard the non-linearisation of the problem, but that would be reasonable for design projects where the decision process is of paramount importance and the (many) goals need a more accurate weighting model.

An existing example of the selection process is found in the publication *Material Selection Method in Design of Automotive Brake Disc* [19]. The document can be used as a guideline to evaluate the properties, although it lacks of a high number of choices so more materials would need to be studied. Furthermore, the implemented method is the DL, whose accuracy can be improved by the MDL proposed in the above paragraphs. So taking into consideration these potential improvements, the technique will be used as reference later on with regard to an index of performance (IoP) and its increment among materials for comparison to build the tables.

2.2.2 Simulation Model

In this section existing research on the dynamics of the blade in flight is retrieved. The purpose is to collect relevant information in order to create a model that simulates the motion of the blade in the autogiro forward flight. There are two main subsections here: the first one elaborates on both the rotor head an the friction damper and the second one contains research on the blade motion.

2.2.2.1 Rotor Head & Friction Damper

There exist different rotor heads depending on the conditions at the blade joint, as the professor Pablo Ringegni from La Plata National University explains [W22].

In particular, the autogiro C.30 has a fully articulated rotor head, which relieves the loads on the blades and the rotor head, as opposed to the rigid one. Two articulations allow free motion of the blades providing one DoF each: one parallel and another perpendicular to the plane of rotation. Each blade, thus, can individually flap (moving perpendicularly up and down to the rotation plane) and lead/lag (moving fore and aft in the rotation plane with respect to the rotor shaft angular velocity).

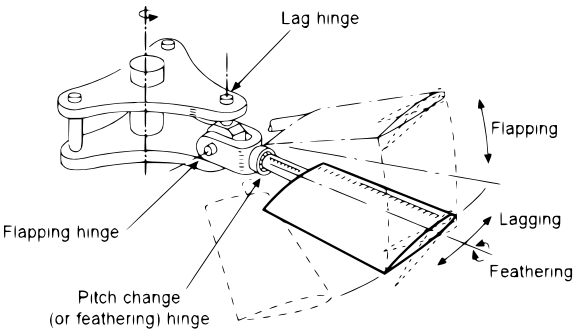

Figure 2.5: Hinges & motions on fully articulated rotor [25].

The position of the hinges is selected in accordance to the correction of vibrations transmitted to the fuselage. A damper is also installed for the same reason.

But the most important advantage of this system is the lift redistribution on the rotor disc that controls stability and relieves bending. Gordon Leishman approaches the fundamentals from the very first steps of rotorcraft history in his book *Principles of helicopter aerodynamics* [15]. As the gyroplane is in steady straight forward flight, with a relative headwind component, the blades can be advancing or retreating with a velocity component favourable or opposed to the flight direction respectively. On the advancing side, the blade finds higher aerodynamic velocity, with subsequent increment in lift. In contrast, on the retreating side, the blade has lower aerodynamic velocity and lift decreases. Figure 2.6 shows a comparison of the lift distribution with and without flapping.

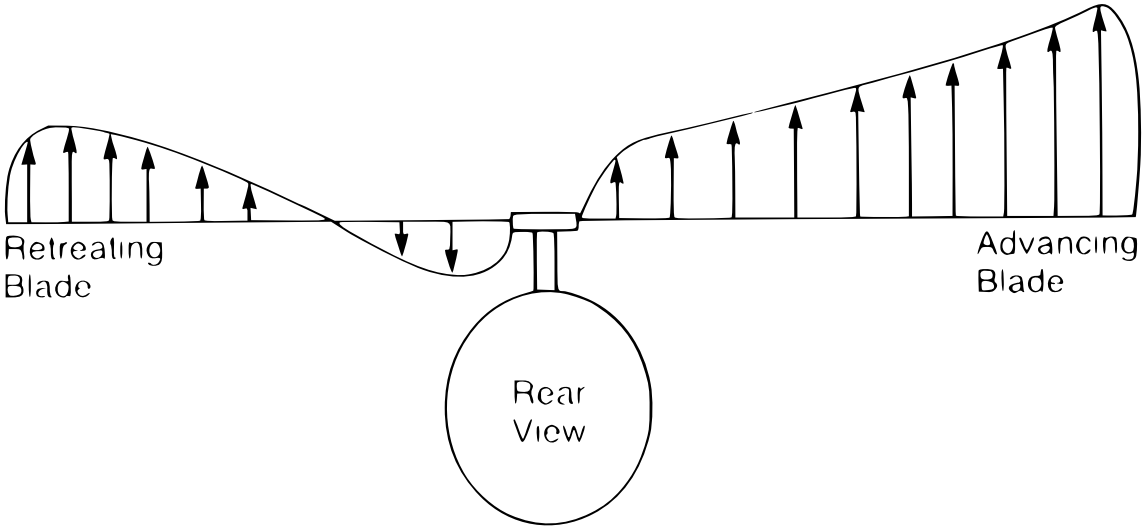

(a) Lift distribution without flapping.

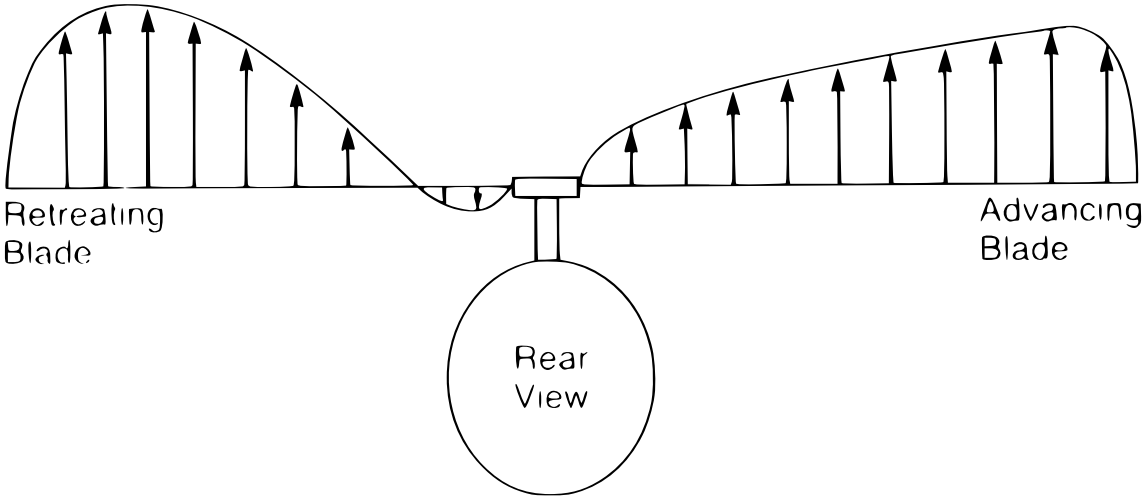

(b) Lift distribution with flapping.

Figure 2.6: Effect of blade flapping on lateral lift distribution [W4].

The revolutionary concept was the key point that made it possible for Juan de la Cierva to fly the gyroplane without rolling over and crashing. The resulting flapping motion is represented in fig. 2.7 where the blade shows an angular displacement that balances the lift force.

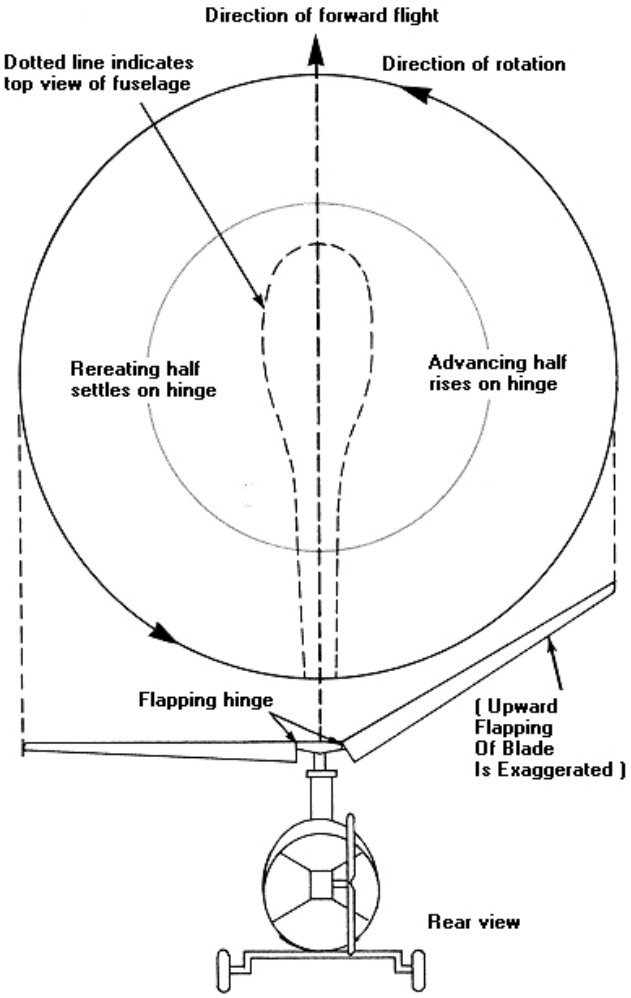

Figure 2.7: Blade flapping in forward flight [W14].

2.2.2.2 Blade Motion

Literature in this part is divided into three categories that elaborate on the equations of motion for rotating rigid bodies, a suitable friction model for brake discs and the fundamentals to build the aerodynamics model.

2.2.2.2.1 Equations of Motion

Different approaches are useful to study the dynamics of the rotor blades. *Bramwell's Helicopter Dynamics* [6] proposes the (extended) Euler's equations: formulated for spinning rigid bodies, they are convenient to model the flapping and lagging motions.

For a rigid body in rotation about a point O, with inertia tensor $\boldsymbol{I}$ about the principal axes, angular velocity $\boldsymbol{\omega}$, moment $\boldsymbol{M}_0$ on the origin (actually the blade hinge) and other external moments $\boldsymbol{M}$, the Euler's extended equation in vector form is expressed as:

$$\boldsymbol{I} \cdot \dot{\boldsymbol{\omega}} + \boldsymbol{\omega} \cdot (\boldsymbol{I} \cdot \boldsymbol{\omega}) = \boldsymbol{M_o} + \boldsymbol{M} \tag{2.1}$$

From this expression, one can select the axes of interest, namely flapping and lagging axes, to study the oscillatory equations that govern these motions separately.

As a remark from the fundamental procedure in classical mechanics, several frames of reference are defined first with the aim of having a set of non-inertial reference systems related to the inertial one. Each frame involves a rotation from another, so that it is possible to have the blade principal directions linked to the rotor head principal axes through direct orthogonal transformations. In addition, the relative wind frames with respect to both the rotor head and the blade must be considered. In the end, the algebraic computations will be simplified as the variables are defined in the most convenient frame with their simplest expressions.

2.2.2.2.2 Friction

There exist many theories modelling friction phenomena. The kynetic friction model (KFM) [1] is widely used as a consistent approach in engineering when dealing with the interaction of two body surfaces in contact.

Aerospace engineers from Georgia Institute of Technology compare in their publication *Semiactive Coulomb Friction Lead–Lag Dampers* [10] two different lead/lag dampers performance in a helicopter: a Coulomb damper and a hydraulic damper.

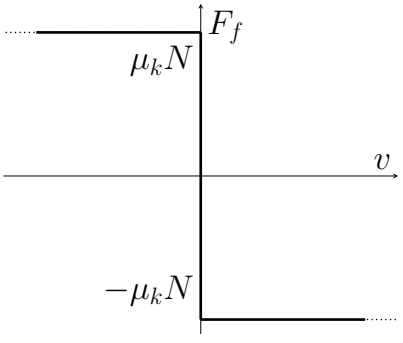

Figure 2.8: Coulomb's friction law with constant N.

According to Coulomb's law for a sliding point particle, kinetic friction $\boldsymbol{F}_f$ always opposes to velocity $\boldsymbol{v}$ direction and is proportional to the normal force N and a constant coefficient μ_k, which depends intrinsically on the surface characteristics. A problem emerges in the unidirectional case with the discrete behaviour that exists in the change of direction sign, as observed in fig. 2.8. This adds difficulties to numerical computation.

$$\boldsymbol{F}_f = -\frac{\boldsymbol{v}}{|\boldsymbol{v}|}\ \mu_k N \tag{2.2}$$

In real life, an additional adversity appears when static, Stribeck and viscous frictions come into play. Known as the modified Stribeck model, this generally used friction law depicts a more accurate behaviour under the whole scenario (fig. 2.9). The gentle inclination close to zero-velocity eliminates the discrete inconvenience. Firstly a 'brake-away' force must be exceeded in order to transit from the static to the kinetic region. Then over the kinetic domain the Coulomb point is found, which corresponds to the local minima (in absolute value). Finally the linear viscous term provides the asymptotic behaviour.

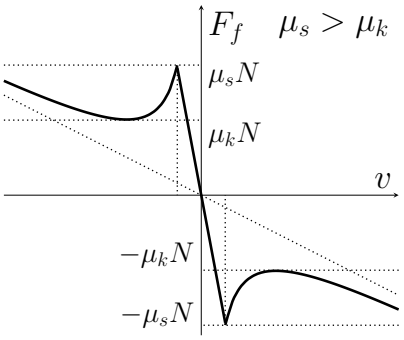

Figure 2.9: Modified Stribeck friction model.

Even though the KFM regards all these contributions, for many applications the problem can be faced simply by means of one of them: a modified Coulomb's friction law. In their project, the American researchers work with an amendment to Coulomb's law that models a continuous friction law in the unidirectional transition from one direction to the opposite. Namely:

$$\boldsymbol{F}_f = -\frac{\boldsymbol{v}}{|\boldsymbol{v}|}\ \mu N\ \tanh\left(\frac{v}{v_0}\right) \tag{2.3}$$

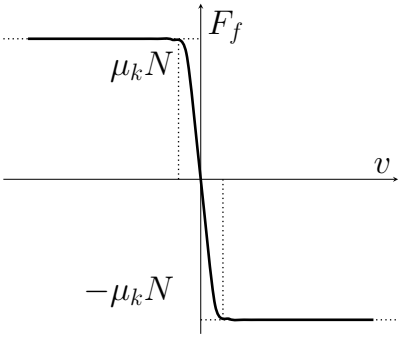

Figure 2.10: Modified Coulomb's friction law.

The hyperbolic tangent is the correction factor that smooths out the discontinuity, where a characteristic velocity v_0 is arbitrarily defined very small compared to the instantaneous speed v. As the authors state: "sticking is replaced by 'creeping' between contacting bodies with a small relative velocity". Compared to a more accurate friction model (LuGre's law) similar to the modified Stribeck law seen above, the modified Coulomb's law proves effectiveness, as they claim, due to the similarity of results at lower computational costs.

Therefore the present study will consider the modified Coulomb's friction law to determine the friction by the damper acting on the blade lagging motion.

2.2.2.2.3 Aerodynamics

Depending on the type of aerodynamics study, some theories are more adequate than others. Regarding the analysis of a blade motion in flight, the thin aerofoil theory (TAT) and the blade element theory (BET) become useful to obtain the overall moment by the aerodynamic forces that needs to be replaced in the aforementioned Euler's equations.

The TAT [9] facilitates the linear relation of the lift with the AoA to build a simple two dimensional model that computes the local force at each section of the blade (aerofoil). The theory is formulated under the main assumptions of incompressible, inviscid flow, small AoA and a thin aerofoil, whose thickness is much smaller compared to the chord. Even though this theory cannot predict the stall, it can suffice the needs in the analysis of a simplified rotor blade dynamics model.

Additionally, the BET [W11] works in two dimensions considering every section in the blade by means of the TAT. All aerodynamics computations are locally expressed in terms of the blade length as a variable. The elements of interest are the lift and drag to obtain the local resultant force. Then the total force acting on the blade is obtained by integrating along the span.

The mathematical analysis of these theories is developed in detail later on in the simulation methodology part of the document, chapter 4.

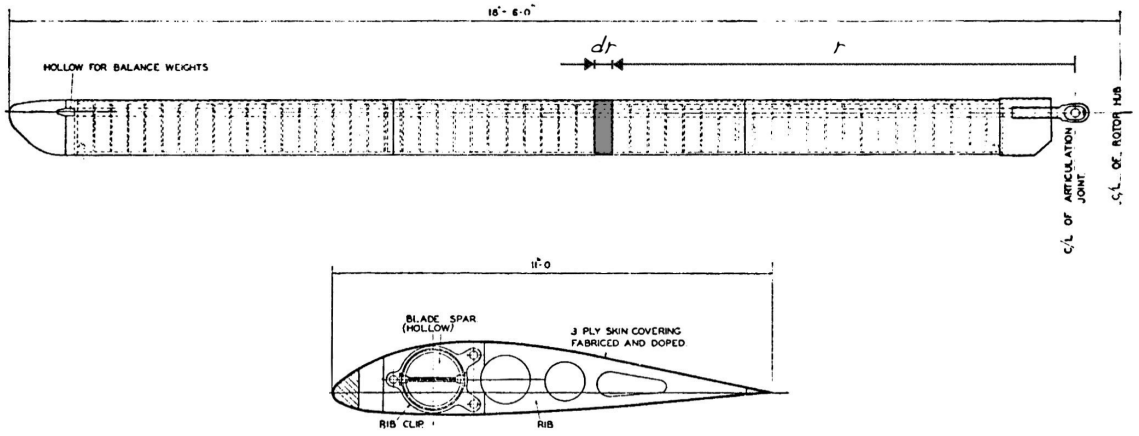

Figure 2.11: View of blade (top) & section (bottom) as a differential of span [2].

Furthermore, the student Sadaf Mackertich develops a thorough research on wind harvesting in his master thesis *Dynamic Modeling of Autorotation for Simultaneous Lift and Wind Energy Extraction* [16]. He uses a kite model based on the autogiro to generate lift and extract wind from it when the adequate wind conditions are present. In the research process the author explains how the air velocity distri-

bution on the blade span-wise affects the torque under auto-rotation conditions. An auto-rotating blade is illustrated in fig. 2.12 at an instant. The inner sections find higher AoAs where the driving force is higher than the drag parallel component. Within this section the net torque is positive. Oppositely, sections lying in the outer region find lower AoAs that result in lower driving forces and higher drag. Within this section the net torque is negative. Between both regions there exists a specific point where the net torque equals zero: ideal auto-rotating conditions hold. Higher rotor speeds would move the point inwards and lower rotor speeds would have the opposite effect. This holds under the assumption of momentum conservation, which is made possible with the provision of a fully articulated rotor.

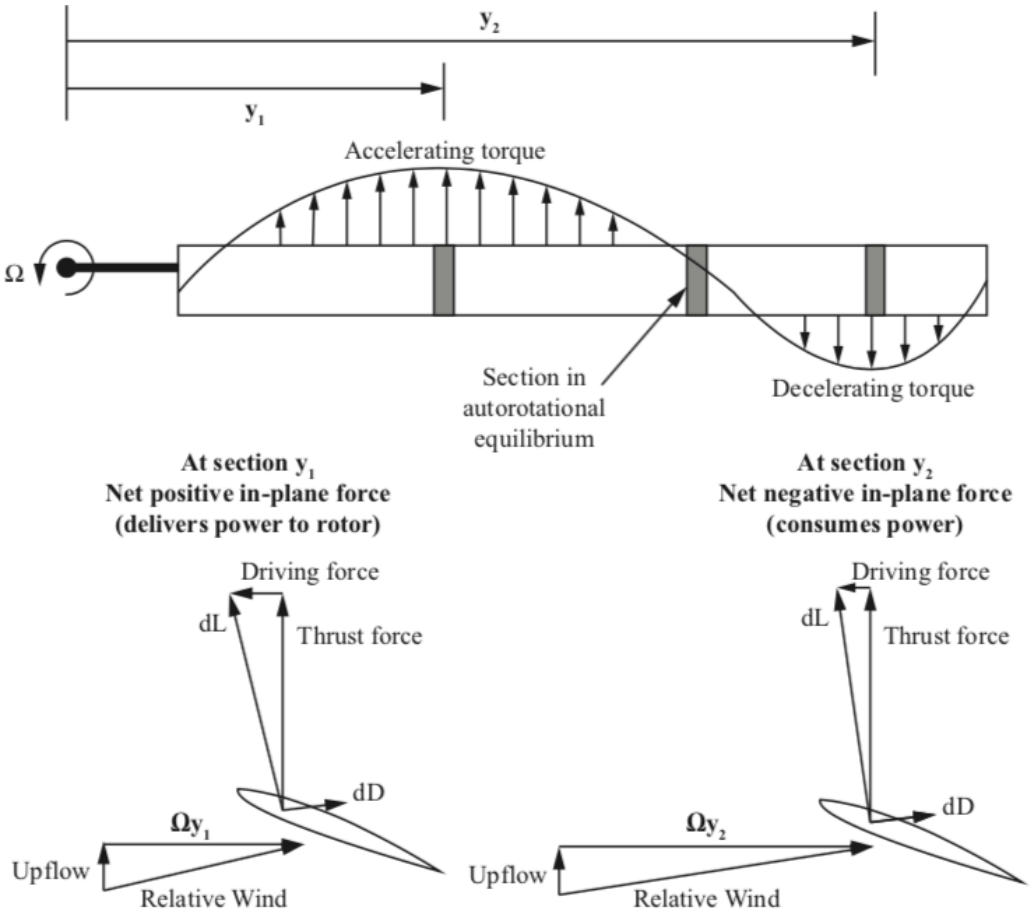

Figure 2.12: Torque distribution along the blade [16]. Angles exaggerated.

Because the integration must give zero total torque for auto-rotation conditions, the present study will assume constant rotor speed for simplicity and consider the aerodynamic torque with the aim of providing a force contributing to the blade motion relative to the hinge, but not to the rotor change in speed.

2.3 Regulatory & Socio-Economic Frameworks

2.3.1 Socio-Economic Impact

In the article *The evolution of the British rotorcraft industry 1842-2012* [14] relevant steps in the evolution of the autogiro are highlighted and it will be used as reference along the section. According to his extensive biography [22], Juan de la Cierva was managing in the early 1920s to solve the stability problem that his first versions of the gyroplane were facing. As of the quasi-successful C.4 model the projects that had been self-financed were now subsidised by the Spanish Military Aviation. The C.6 successfully flew between two aerodromes, which attracted Scottish investors who supported economically the development of the invention. The Cierva Autogiro Company Ltd. was founded and the first models were sold in the UK.

Important air-shows in the USA opened a new window for further investors in the late 1920s. The Pitcairn-Cierva Company was founded by such a well-known American businessman and the British The Cierva Autogiro Company. France purchased a number of units and Germany built the headquarters of La Cierva Autogiro GMBH in Berlin for their authorised production.

By the 1930s the autogiro was already known all over the globe. In fact, the Fédération Aéronautique Internationale (FAI) awarded Juan de la Cierva in 1932 with its most prestigious distinction: the FAI Gold Air Medal. The gyroplane was still in process of enhancement, notwithstanding different European military forces and other top economic powers in the world gained interest and acquired several units, especially after exhibiting the gyrocopter crossing the English Channel. The eminent manoeuvrability and the wide range of flight speeds were definitely an indicator of great performance capabilities that the armed forces would require for the upcoming WWII. This had a global impact and the patents would soon travel to other countries worldwide —ten significant units are illustrated in fig. A.1 in appendix A—. The announcement of the C.30 in 1934 supposed a revolution with the direct control on the attitude through a column, removing the small wings. Later models like the C.40 reached the zenith of the gyroplane era with the jump take-off.

At that time the helicopter (yet as a concept) was deeply desired. Despite being something feasible, Juan de la Cierva claimed that it was fairly complex to develop [W18]. A decade later in the 1940s, inspired by the gyrocopter, the Ukrainian Sikorski would come up with the solution for the helicopter, which would quickly replace the gyroplane. The WWII would also play an important role in its extinction: they were demobilised in 1945, only surviving twelve units. In the present, the autogiro has not prevailed upon the helicopter except for sport aviation purposes.

To sum up, the eminently large social and economic impact of the autogiro in the mid-20^{th} century covered military and general (commercial and private) aviation. But the emergence of the helicopter ceased the operation, reducing it to sport aviation. Nowadays some manufacturers have their own gyroplane models, but the Cierva autogiro is not manufactured any longer for obvious reasons. The construction of a replica would allow the exhibition in national air-shows of the yet old aircraft.

In conclusion, the economic impact of this study as a part of a global commemorative project (Juanito C.30) would not have presumably any transcendent repercussion. However, the social impact would be vastly affected in that the operational replica of the C.30 could bring the society back in time. It would definitely foment the national culture within aeronautics with such a historical piece of aviation.

2.3.2 Legal Framework

Airworthiness (AW) measures the capability of an aircraft to operate under safe conditions. The certificate of AW is issued by the national aviation authority of the state where the aircraft is registered. Correct maintenance and tests must be followed as established to preserve its validity.

The national agency in charge of the civil aviation (CA) security in the Spanish territory is Agencia Estatal de Seguridad Aérea (AESA). This organism complies with the European regulations and has the competence to extend them as long as the bases are always respected.

2.3.2.1 European Level

The regulation of the European Parliament and of the Council of 20 February 2008[2] establishes the common rules in the field of CA. More specifically, article 4(1) of chapter II sets the "basic principles and applicability to aircraft, including any installed product, part and appliance". However, according to article 4(4) such principles do not apply to aircraft falling in one or more of the categories set out in annex II. Among these categories, the C.30 autogiro complies with four —(a), (b), (f) and (h)—, being the third a potential one. They read as follows:

[2][L2] REGULATION (EC) No 216/2008 OF THE EUROPEAN PARLIAMENT AND OF THE COUNCIL of 20 February 2008 on common rules in the field of civil aviation and establishing a European Aviation Safety Agency, and repealing Council Directive 91/670/EEC, Regulation (EC) No 1592/2002 and Directive 2004/36/EC.

(a) historic aircraft meeting the criteria below:

(i) non-complex aircraft whose:

— initial design was established before 1 January 1955, and

— production has been stopped before 1 January 1975;

or

(ii) aircraft having a clear historical relevance, related to:

— a participation in a noteworthy historical event, or

— a major step in the development of aviation, or

— a major role played into the armed forces of a Member State;

(b) aircraft of which at least 51% is built by an amateur, or a non-profit making association of amateurs, for their own purposes and without any commercial objective;

(f) single and two-seater gyroplanes with a maximum take off mass not exceeding 560 kg;

(h) replicas of aircraft meeting the criteria of (a) or (d) above, for which the structural design is similar to the original aircraft;

2.3.2.2 International Standardisation

A detailed set of common and wide requirements for the CA management is written by the Joint Aviation Authorities (JAA), according to the regulations established by the International Civil Aviation Organization (ICAO). Among these, the Joint Aviation Requirements (JAR) correspond to the proceedings for the certification of civil aircraft, products and pieces related to such (called JAR-21). They are founded on the the annex 8 of article 37 of the Convention on International Civil Aviation (Chicago 1944), which establishes superior standards of safety.

Aiming for national presence within the international framework in relation to the civil aircraft certification proceedings, products and pieces related to such and, particularly, to obtaining the type certificate (TC) and aircraft AW, the approval of entities that design and manufacture aerospace products, and the approval of pieces and instruments for such products, the regulations JAR-21 became applicable through a Royal Decree[3] as of 11^{th} July of 2001 officially published by the Spanish government.

[3] [L1] Real Decreto 660/2001, de 22 de junio, por el que se regula la certificación de las aeronaves civiles y de los productos y piezas relacionados con ellas.

For the present study, the pertinent guideline in that document to be followed in the design process of the material is found at point 4.1.2 of chapter 4, part II. It reads as follows:

> 4.1.2. Materials
>
> All materials used in parts of the aeroplane essential for its safe operation shall conform to approved specifications. The approved specifications shall be such that materials accepted as complying with the specifications will have the essential properties assumed in the design.

2.3.2.3 Summary

With respect to annex II upon article 4 of the European regulation No 216/2008:

- The initial design of the C.30 was patented in 1934, the production ceased in 1945 and its historical relevance lies potentially on a major step in the development of aviation. Consequently point (a) is met.
- AJCC takes the sole and ultimate responsibility of the design and construction of the aircraft as an association founded by amateur members, complying with point (b).
- According to the autogiro documentation [17], the maximum take-off mass (MTOM) is 854 kg. However, if the eventual new design of the replica reduced the weight allowing 560 kg MTOM or below, article (f) would be satisfied. It is not relevant, though, because at least other points are met.
- The design is a replica of the original C.30 autogiro and the previous point (a) was met, therefore in agreement with article (h).

Summing up, since the replica of the C.30 gyroplane lies within the historical category and it is built by a non-profit amateur association, the **European regulations for standard civil aircraft are exceptionally not applied**. As an extraordinary case, the application form[4] *Certificado de Aeronavegabilidad no EASA - Anexo II* (non-EASA certificate of airworthiness) must be downloaded, filled by AJCC and sent back to AESA.

Besides, the material selection process in the present project will need to define a set of criteria within the scope of the JAR-21 standards in order to finally get the approval after aircraft tests by AESA.

[4] Application forms for airworthiness certificates are available online at AESA's website.

3 Material Research

This chapter section of the methodology contains information about the process of material research for the friction damper disc and it is divided into five sections. The first one justifies the material properties that are needed for a friction disc and gives a relative weight to each. The second section proposes a number of candidate materials and lists their properties. The third one scales those properties. The fourth section derives the expression for the compression force needed to screw the damper and the resulting stress. The fifth and last one shows the results obtained and the discussion of them.

Some information that the official documents provide about the damper and the blade is recorded in table 3.1. It will be useful for calculations in upcoming sections. Other relevant pieces of data will be detailed in tables later on when necessary.

System	Notation	Value	Units (SI)	Description
Damper	e_h	0.224	m	Eccentricity of hinge
	R_i	0.057	m	Inner radius of damper washer (ferodo)
	R_o	0.070	m	Outer radius of damper washer (ferodo)
	F_{spring}	51.155	N	Force on spring balance at blade tip (calibration)
Blade	m	22.2	kg	Mass of blade
	R	5.639	m	Radius of rotor disc (from rotation axis to blade tip)
	b	5.415	m	Span of blade
	c	0.279	m	Chord of blade
	x_{cm}	2.275	m	Distance from hinge to center of mass

Table 3.1: Reference data of damper & blade [12, 3, 20].

The damper is installed between the rotor head and the blade root. Its components consist on a friction disc and two washers exerting pressure against each side of the disc. There is a total number of two discs and four washers in a damper. Figure 3.1 illustrates the cross-section where components are shown in detail.

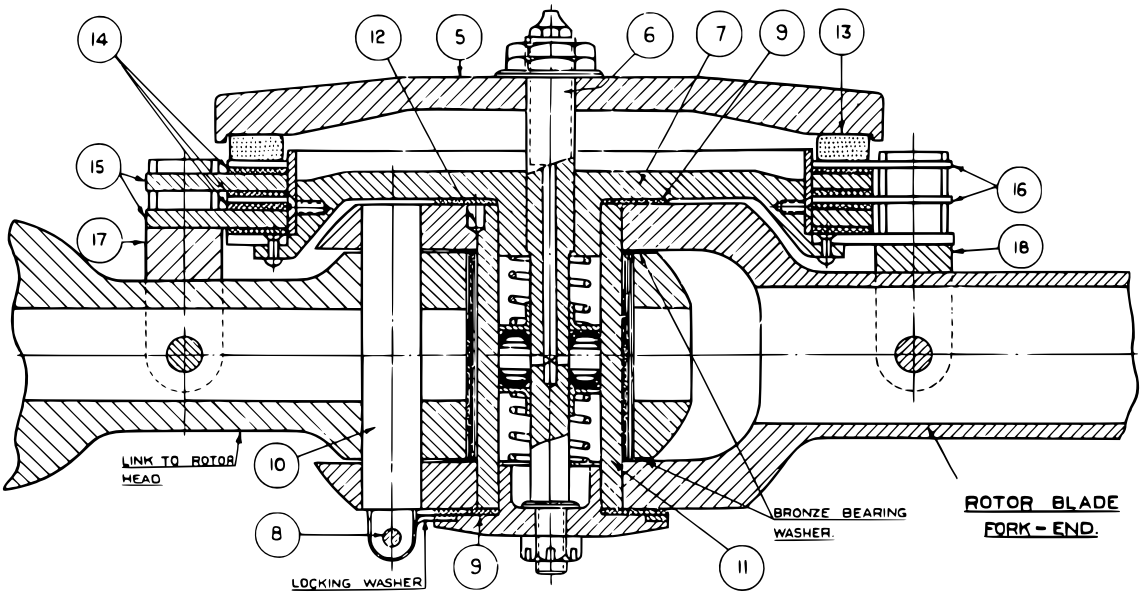

Figure 3.1: Friction damper cross-section [3].

3.1 Properties

An insight into the most significant properties as a first step will allow to filter materials. So the next few lines aim to state the thermo-mechanical properties needed as well as to give a priority to each by quantifying their relative weight.

The material weight, measured by its density, is often presented as an obstacle for aerospace engineers. Mass is a key-point whose minimisation becomes a priority.

As a friction damping system, the friction coefficient deserves attention. However it is not the only factor in the friction law: the normal (compressive) force term can be adjusted up to the point of suitable friction. Hence there is some freedom to play with this property; higher friction coefficients will reduce the compressive force required alleviating the stress and vice-versa.

Mechanical performance is a concern to guarantee the structural integrity. It will be measured with the compressive strength of the material and the tensile strength, that will be essential due to the huge variations in thermal stress.

Other two properties of paramount importance in the selection procedure are the specific heat and thermal conductivity. Withstanding a high heat flux is necessary while operating in flight, despite existing advantageous cooling rates in flight by convection from the strong relative airflow. From the thermal stability point of

view, metals and ceramic compounds offer excellent performance as explained in the literature reviewed. It is worth mentioning that thermal properties are considered since they play a role in performance, but the thermal analysis is out of the scope of this project. A more in-depth study would be necessary to check the validity of the proposed materials in terms of their thermal characteristics.

Summarising, the properties that will take part in the selection process are:

- Density
- Friction Coefficient
- Compressive strength
- Tensile strength
- Specific heat
- Thermal Conductivity

And the weighting of each property n_i is done by means of the MDL method. Table 3.3 shows the application of the method and the relative weights that make the material properties quantifiable, whose process is described in the following lines.

Every pair of properties involves one decision, so the possible decisions N are simply the total number of pairs that can be grouped. It can be obtained using the expression:

$$N = \frac{\sum n_i(\sum n_i - 1)}{2} \tag{3.1}$$

Therefore with 6 properties the possible decisions is 15. An alternative easy way to compute the total possible decisions is constructing a table where each pair of properties is crossed once, as in table 3.2, and noting down the number of crosses.

n_i	A	B	C	D	E	F
A		✗	✗	✗	✗	✗
B			✗	✗	✗	✗
C				✗	✗	✗
D					✗	✗
E						✗
F						

Table 3.2: Graphical method to obtain possible decisions for properties A to F.

After evaluating the priority of each property in all possible decisions with 1, 2 or 3 (as explained in section 2.2.1.2) the valuations are summed up and noted down as positive decisions (N^+).

The relative weight α is finally obtained dividing the positive decisions of each property over the total number of positive decisions.

$$\alpha_i = \frac{N_i^+}{\sum N_i^+} \tag{3.2}$$

Property	**Possible Decisions [$N = 15$]**															**Positive Decisions**	**Relative Weight**
[n_i]	1	2	3	4	5	6	7	8	9	10	11	12	13	14	15	[N_i^+]	[α_i]
Density	3	3	3	1	1											11	**$11/60 = 0.183$**
Friction Coefficient	1					1	1	1	1							5	**$1/12 = 0.083$**
Compressive Strength		1				3				2	1	1				8	**$2/15 = 0.133$**
Tensile Strength			1				3			2			1	1		8	**$2/15 = 0.133$**
Specific Heat				3				3			3		3		3	15	**$1/4 = 0.250$**
Thermal Conductivity					3				3			3		3	1	13	**$13/60 = 0.217$**
$\sum n_i = 6$																$\sum N_i^+ = 60$	$\sum \alpha_i = 1$

Table 3.3: Relative weights of properties according to MDL method.

Because weldability, wear resistance and corrosion resistance are complex to quantify, they will be put apart and considered only in the discussion of results to make a final decision.

Finally, it is worth mentioning that a reduced budget is available according to AJCC. It will be a factor with great significance constituting the criteria: looking for low costs.

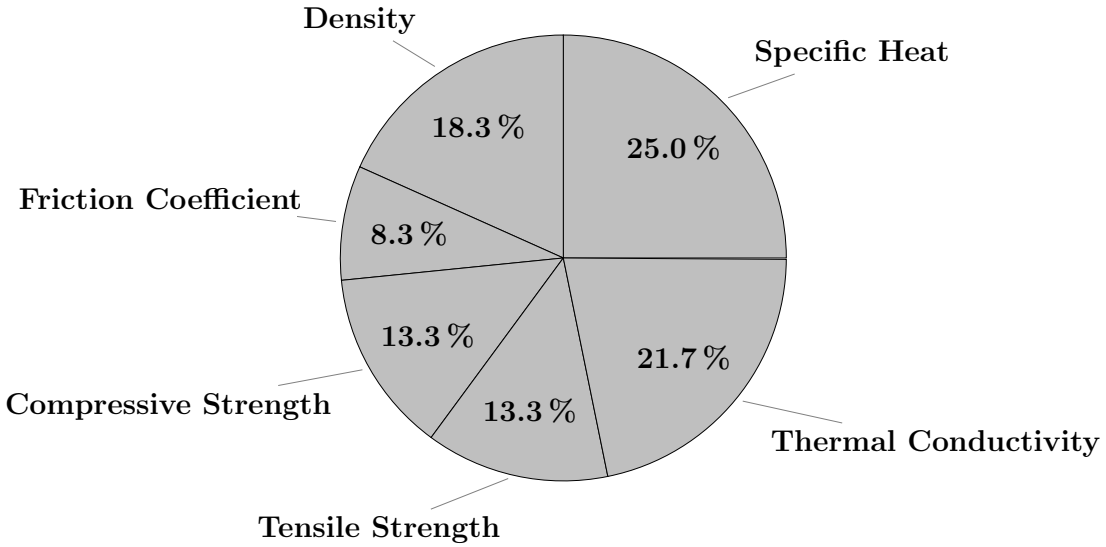

Figure 3.2: Relative weights of properties.

3.2 Candidates

Owing to demanding thermo-structural stability conditions that the element must comply with, metallic materials —particularly alloys— offer the most suitable choice when balancing out all the properties. Retrieved from a materials database, in table B.1 (in appendix B) different metals are detailed to be compared according to their properties. There are mainly five different types of materials to be evaluated:

- Aluminium
- Steel
- Cast iron
- Titanium
- Ceramic Composites

The most significant specimens for aerospace application and the described working conditions are chosen as candidates. Because the global balance of the properties might favour the Al alloys, as previously seen, they will be considered together with the grey cast iron alloys as potential candidates. In addition, steels, carbon ceramic compounds and titanium alloys are included to widen the range of choice possibilities.

3.3 Selection

In order to scale the properties of each material according to the relative weights in table 3.3, there are two types of relations to consider: directly and inversely proportional. Some properties have a directly related scale (the higher, the better) and some others have an inversely proportional one (the lower, the better). Both formulae expressing the scales in the basis of unity are respectively:

$$\beta_{i,j} \equiv \text{Scaled Property (i) of Material (j)} = \frac{\text{Actual Value of j}}{\text{Max. Value Among All}} \tag{3.3}$$

$$\beta_{i,j} \equiv \text{Scaled Property (i) of Material (j)} = \frac{\text{Min. Value Among All}}{\text{Actual Value of j}} \tag{3.4}$$

Figure B.1 in appendix B plots the average scaled properties of each type of material. An IoP is obtained from the sum of the product of the relative weights and their scaled properties.

$$\delta_j \equiv \mathrm{IoP}_j = \sum_i \alpha_i \cdot \beta_{i,j} \tag{3.5}$$

Finally a figure of merit (FoM) takes into account a factor that modifies the IoP in favour of the (volumetric) material cost. The IoP is divided by the cost per unit mass C and the density ρ of the material. It can be eventually rescaled to the most convenient multiple of 10 just for the sake of reading; it will determine the ranking of the materials.

$$\gamma_j \equiv \mathrm{FoM}_j = \frac{\delta_j}{C_j \cdot \rho_j} \tag{3.6}$$

The complete process is collected in table B.2, which is found in appendix B.

Results will be sorted including only the ranked materials with increments of IoP and cost respect to the first one, which represents the optimum option.

$$\Delta\gamma_j = \frac{\gamma_j - \gamma_1}{\gamma_1} = \frac{\gamma_j}{\gamma_1} - 1 \tag{3.7}$$

$$\Delta C_j = \frac{C_j - C_1}{C_1} = \frac{C_j}{C_1} - 1 \tag{3.8}$$

3.4 Compression Force & Calibration Check

Since the axial force F_{comp} on the damper that compresses the friction elements is controlled by a screw and a nut, it can take any constant value depending on the material that is finally used. Derived from the torque M_f exerted by the washers on the disc sides, F_{comp} can be expressed as a function of the friction coefficient of the material μ and the radii of the washer (inner R_i and outer R_o) that determine the friction area A_c and the pressure S. Each damper includes two discs with two washers one washer on each side, which makes a total four contact surfaces where friction is acting.

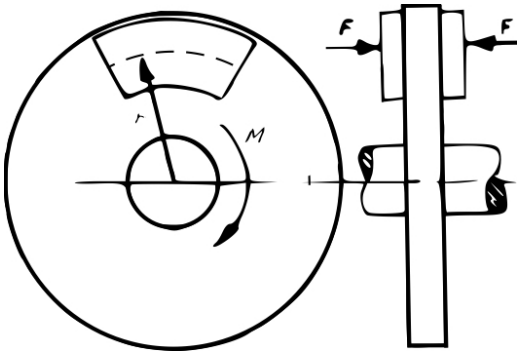

Figure 3.3: Pads compressed against disc brake [W13].

$$F_{comp} = \frac{3}{8}\frac{R_o^2 - R_i^2}{R_o^3 - R_i^3}\frac{M_f}{\mu} \tag{3.9}$$

The derivation of eq. (3.9) is detailed step by step with eq. (B.1) in appendix B with washers being equivalent to annular pads (bodies of revolution).

Because the instructions manual for the C.30 imposes a constant value for the torque, the calibration procedure will remain unchanged (read section 2.1).

The compression strength S_m intrinsic to each type of material must be finally checked upon acceptance by calculating and comparing the stress S produced by the compressing force on the contact area:

$$S = \frac{F_{comp}}{A_c} = \frac{F_{comp}}{\pi\,(R_o^2 - R_i^2)} \leq S_m \tag{3.10}$$

3.5 Results & Discussion

Table B.2 in appendix B collects all candidate materials and ranks them according to the optimum balance among properties, with material cost being a significant concern as explained.

For convenience, the results are arranged in the ranking of table 3.4. The order is given by the FoM and the variations in the IoP ($\Delta\gamma$) and the cost per unit weight (ΔC) are calculated with respect to the first element. These increments are useful to evaluate each option. For instance, in the eventual case that AJCC, who has the ultimate decision, considered that they need a more economical material, they would know how much performance needs to be sacrificed. In a similar fashion, if they needed a material with better performance —not happening in this case— they would know the increment in price.

#	Material	Type/Grade/Class		$\Delta\gamma$ [%]	ΔC [%]
1	Aluminium	Alloy (cast)	356.0	0.0	0.0
2	Aluminium	Alloy (cast)	852.0	−2.3	+87.0
3	Aluminium	Alloy (cast)	333.0	−13.4	−8.7
4	Aluminium	Alloy (cast)	514.0	−8.7	+8.7
5	Aluminium	Alloy (cast)	518.0	−12.7	+13.0
6	Steel	Alloy	SAE 4027	−47.8	−69.6
7	Aluminium	Alloy (cast)	705.0	−13.9	+52.2
8	Aluminium	Alloy (cast)	713.0	−10.0	+65.2
9	Steel	Carbon	SAE 1547	−44.4	−60.9
10	Steel	Alloy	SAE 5140	−45.3	−60.9
11	Steel	Stainless	AISI 201	−42.9	−52.2
12	Steel	Alloy	SAE 9255	−46.2	−52.2
13	Cast Iron	Grey	ASTM A48 CLASS 40	−37.8	−39.1
14	Cast Iron	Ductile	ASTM A536	−43.9	−34.8
15	Steel	Carbon	SAE 1045	−46.2	−43.5
16	Steel	Carbon	SAE 1006	−49.2	−43.5
17	Steel	Stainless	AISI 410	−45.5	+4.3
18	Steel	Stainless	AISI 2205	−45.3	+30.4
19	Titanium	Alloy	Ti-6Al-4V	−21.1	+2726.1
20	Composite	Al-Matrix	SiC-Fibres	−38.6	+69465.2
21	Composite	C-Matrix	C-Fibres	−14.0	+173813.0
22	Composite	SiC-Matrix	SiC-Fibres	−31.7	+156421.7

Table 3.4: Ranking of materials & increments in IoP and cost with respect to #1.

The overall balance of the properties studied indicates that the most suitable material is the cast Al alloy 356.0, whose chemical composition is shown in fig. 3.4. It is important to remember that the results are valid only under the assumptions made, which involves the material properties concerned and the criteria defined by the MDL method to assign their relative weights. Notwithstanding, the choice made is supported by [17], where the Al is originally the material intended for the manufacturing of the friction disc.

From a general point of view, the series $3xxx$ of Al alloy is the most convenient for the task as shown in table 3.4. According to the literature reviewed [5] this series offers about extra 20% strength compared to the $1xxx$ series. As expected, the $8xxx$ series is also a potential candidate that can compete with the series $3xxx$. It is followed by the series $5xxx$, which makes sense as moderate-to-high-strength work-hardenable alloy. They have acceptable welding characteristics and corrosion resistance, especially in marine atmospheres, although they are diminished at high

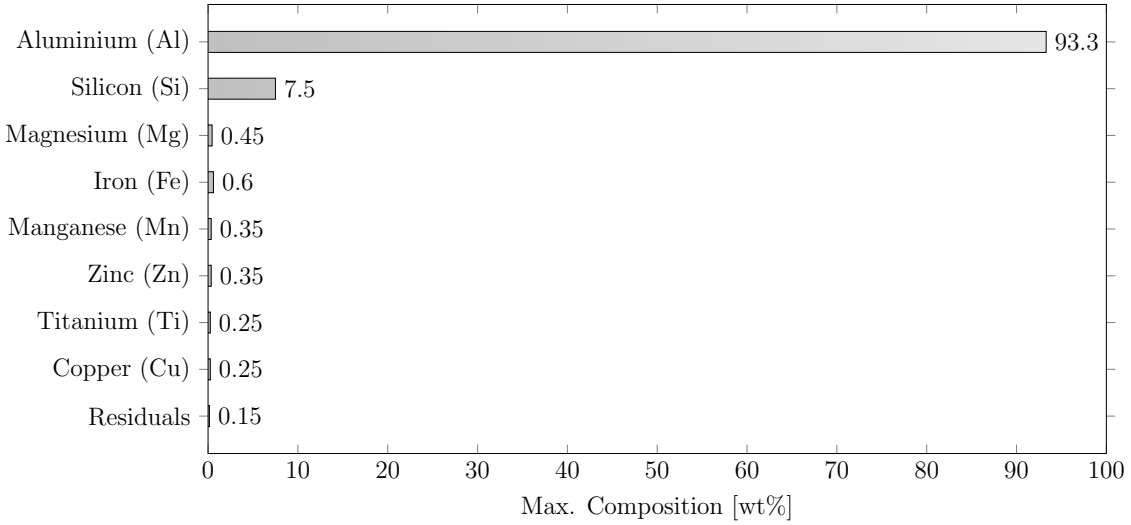

Figure 3.4: Chemical composition of cast aluminium alloy 356.0 [5][W17].

operating temperatures. The $7xxx$ is found a couple positions below, providing moderate-to-high strengths too and offering excellent behaviour under high stress conditions. However, extreme precaution must be taken as they are more vulnerable to stress corrosion cracking and overaged-temper techniques are needed as a means of prevention.

In spite of a bigger trade-off between performance and cost, steels are sequent in the ranking, offering an alternative to Al alloys. Extensive information is found in the book *Alloy Steel – Properties and Use* [5]. They are used when demanding mechanical properties are needed. With components added, specially Cr, they become quite resistant upon corrosion in different chemical environments.

Cast irons are significantly penalised owing to density and thermal behaviour against other materials (see fig. B.1 in appendix B). Even though they offer magnificent performance in the automotive industry, they fall behind Al and other materials in this specific application: they prove better effectiveness in braking, which is not the actual purpose in rigorous terms when it comes to damping —only moderate energy dissipations are searched instead—. In contrast, titanium (Ti) alloys and other composites descend to the bottom positions due to their expensive prices in the market.

It is good praxis in engineering checking limits of a material performance, even if they seem obvious in many cases. As a means of checking the compliance of the materials in terms of their compressive strength, the friction coefficients from table B.1 are substituted in eqs. (3.9) and (3.10). Table 3.5 shows the final stress

that must be applied to the disc and washers to get the desired friction torque. It must always be lower than the corresponding compressive strength, otherwise the material is rejected.

#	Material	Type/Grade/Class		μ_{min} [-]	S_m [MPa]	F_{comp} [kN]	S [kPa]	$S < S_m$
1	Aluminium	Alloy (cast)	356.0	0.47	170	2.3	446	✓
2	Aluminium	Alloy (cast)	852.0	0.47	185	2.3	446	✓
3	Aluminium	Alloy (cast)	333.0	0.47	150	2.3	446	✓
4	Aluminium	Alloy (cast)	514.0	0.47	85	2.3	446	✓
5	Aluminium	Alloy (cast)	518.0	0.47	140	2.3	446	✓
6	Steel	Alloy	SAE 4027	0.10	140	10.9	2095	✓
7	Aluminium	Alloy (cast)	705.0	0.47	125	2.3	446	✓
8	Aluminium	Alloy (cast)	713.0	0.47	175	2.3	446	✓
9	Steel	Carbon	SAE 1547	0.10	210	10.9	2095	✓
10	Steel	Alloy	SAE 5140	0.10	150	10.9	2095	✓
11	Steel	Stainless	AISI 201	0.10	365	10.9	2095	✓
12	Steel	Alloy	SAE 9255	0.10	150	10.9	2095	✓
13	Cast Iron	Grey	ASTM A48 CLASS 40	0.25	827	4.3	838	✓
14	Cast Iron	Ductile	ASTM A536	0.25	520	4.3	838	✓
15	Steel	Carbon	SAE 1045	0.10	190	10.9	2095	✓
16	Steel	Carbon	SAE 1006	0.10	180	10.9	2095	✓
17	Steel	Stainless	AISI 410	0.10	415	10.9	2095	✓
18	Steel	Stainless	AISI 2205	0.10	420	10.9	2095	✓
19	Titanium	Alloy	Ti-6Al-4V	0.38	960	2.9	551	✓
20	Composite	Al-Matrix	SiC-Fibres	0.40	270	2.7	524	✓
21	Composite	C-Matrix	C-Fibres	0.40	100	2.7	524	✓
22	Composite	SiC-Matrix	SiC-Fibres	0.40	450	2.7	524	✓

Table 3.5: Acceptance check of compressive strength.

As expected, metals in general do not present problems with compressive strength for the intended application. The compression force required for the correct damping is far from the limit that these materials can support, as previously mentioned when defining the criteria. Despite having left this property as a last priority, it was considered indeed since it is often reduced at high temperatures, diminishing the performance of the friction damping.

To conclude, based on the results **the material suggested in this project for the disc of the C.30 Autogiro friction damper is the cast Al alloy 356.0**, which shows optimal performance for the intended application at an affordable final cost[1]. The results are supported by [17] where Al is presumably presented as a potential option to manufacture the friction discs. Notwithstanding, the following section is devoted to the simulation of the blade dynamics in flight in order to make a final decision on the mechanical performance of the proposed material.

[1]Corresponding material and manufacturing costs are estimated at the end of the document in chapter 6.

4 Simulation Model

As a way to check the validity during flight operation and understand the dynamics of the blades when the gyroplane flies, this part of the project focusses on the simulation of the blade motion. In the next sections, the procedure is expanded step by step by means of the algebra and the assumptions made when appropriate.

4.1 Assumptions

All the assumptions made in the methodology for the simulation of the blade dynamics are listed in table 4.1 below for convenient reference. Nevertheless, they will all be developed along the next sections.

Classification	**Assumption**
Atmosphere	International standard atmosphere (ISA) conditions at sea level (SL)
Gyroplane	Steady forward flight with no wind (inertial rotor frame)
	Constant rotor shaft revolutions over time
Hinge	Hinge with 2 DoF (flapping and lagging)
Blade	Uniform mass distribution
	Center of mass (CoM) aligned with longitudinal axis
	Infinite stiffness: no deflection
Inertia	Long rectangular flat plate
	Similar moment of inertia (MoI) about lagging and flapping axes
Earth	Flat
Friction	Modified Coulomb's law
Aerodynamics	Approximation of NACA 3316 profile to Göttingen 606 aerofoil
	No geometric nor aerodynamic twist
	No airflow in the blade spanwise direction
	TAT for lift relation with blade AoA
	BET for total aerodynamic force on blade (with no eccentricity of hinge)
Linearisation	Small angle approximation in blade motions and AoA

Table 4.1: Assumptions made for the simulation of the blade motion.

4.2 Frames of Reference

The first step now is setting the reference frames that allow the formulation of the equations. A proper definition from the beginning will translate into simplified algebra later on, so a number of frames are needed as well as the transformations from one to another.

4.2.1 Definition

Two different approaches can be followed: either placing every frame with their origin at the desired position or placing them all together with a common origin. In the second case, they would only indicate the directions: relative positions must be taken into account when doing the algebra. This latter approach will be the one used in the following calculations with all frames meeting the right-hand rule.

- $Ox_Ey_Ez_E$: Flat Earth (inertial). Arbitrary initial point O coinciding with the rotor head centre. Orthogonal axes: Ox_E and Oy_E in the horizontal plane and Oz_E vertical completing the right-hand set.
- $Ox_By_Bz_B$: Body frame (non-inertial). Ox_B longitudinally aligned with the nose. Oy_B perpendicular pointing to the left-hand side of the aircraft. Oz_B points downwards. Useful for expressing the motion of the aircraft within the flat Earth if needed. Rotation about Ox_B, Oy_B and Oz_B axes are given by the positive angles Φ (roll), Θ (pitch), Ψ (yaw) respectively.
- $Ox_Ay_Az_A$: Air velocity frame. First rotation about Oz_B with positive angle β_s and a second rotation about Oy_A with negative angle α. Useful for defining the relative wind direction in flight.
- $Ox_Ry_Rz_R$: Rotor frame (non-inertial). Ox_R coincides with Ox_B and is rotated 180º: Oy_R and Oz_R opposite to Oy_B and Oz_B respectively. This frame and the all the ones above will be assumed later as inertial frames however, with fixed orientation in the steady flight.
- $Ox_1y_1z_1$: Hinge frame (non-inertial). Rotation of a positive azimuthal angle ψ about Oz_R with angular velocity Ω. Ox_1 passes through the hinge radially. Useful for determining the hinge motion within the rotor. Conventionally ψ is often offset at 180º, opposite to the forward flight.
- $Ox_2y_2z_2$: Lagging frame (non-inertial). Rotation of a negative small angle ξ about Oz_1 (backwards). Useful for describing the lagging motion with respect to the hinge.

- $Ox_3y_3z_3$: Flapping frame (non-inertial). Rotation of a negative small angle β about Oy_2 (upwards). Useful for describing the flapping motion with respect to the hinge.
- $Ox_4y_4z_4$: Feathering & blade frame (non-inertial). Rotation of a positive small angle θ about Ox_3. Useful for describing the feathering motion with respect to the hinge, which in this study will only be reduced to the constant blade inclination. This is also the blade frame indicating its principal directions, which helps to define the inertia tensor.
- $Ox_5y_5z_5$: Local aerodynamic frame. Rotation of a negative small angle α_b about Ox_4. Useful for describing the aerodynamic forces acting locally on a blade section.

Figure 4.1 offers a visual understanding. To avoid an excess of axes lines that mess the representation, only the most relevant coordinate frames are shown, recognising the azimuth angle (ψ) in the rotor frame and the lagging (ξ) and flapping (β) angles of the blade with respect to the hinge.

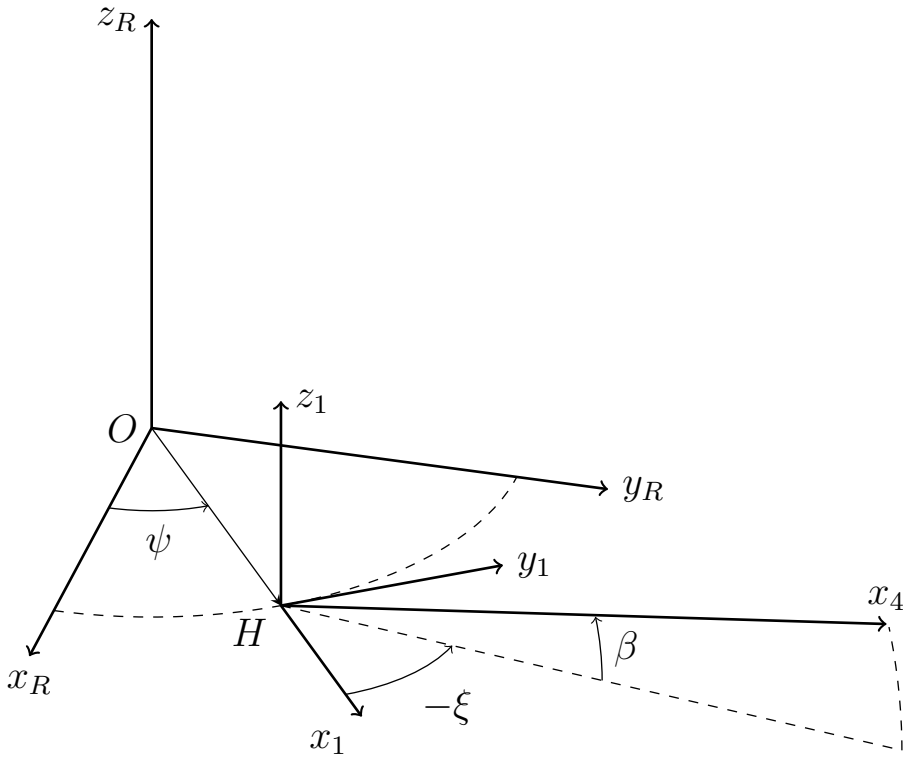

Figure 4.1: Rotor frame ($Ox_Ry_Rz_r$), hinge frame ($Hx_1y_1z_1$) & blade longitudinal axis (Hx_4). Azimuth angle (ψ), lagging angle (ξ) & flapping angle (β).

4.2.2 Transformations

The reference systems defined are mathematically related. The procedure to rotate from one frame to another consists on multiplying by a transformation matrix that relates both of them [W20].

Let vector $\bar{v}$ belong to some linear space and let two different bases A and B in the same vector space. The operation that changes the coordinates of vector $\bar{v}$ from A to B is governed by the transformation matrix $\bar{\bar{T}}_{A\to B}$ such that:

$$\vec{v}_B = \bar{\bar{T}}_{A\to B} \cdot \vec{v}_A \tag{4.1}$$

As a nonsingular or invertible matrix the opposite change can be obtained with the inverse:

$$\vec{v}_A = \bar{\bar{T}}_{B\to A} \cdot \vec{v}_B \tag{4.2}$$

Therefore combining eqs. (4.1) and (4.2) into eq. (4.3) it holds that a matrix which transforms from one base to another is equivalent to the inverse of the matrix that returns the opposite transformation.

$$\bar{\bar{T}}_{A\to B} = \bar{\bar{T}}^{-1}_{B\to A} \tag{4.3}$$

Worth mentioning for simplicity in future computation is another property of orthogonal matrices, whose transpose multiplied by itself gives the identity matrix $\bar{\bar{I}}$. Thus for any orthogonal matrix $\bar{\bar{T}}$ the following statement is satisfied:

$$\bar{\bar{T}}^T \cdot \bar{\bar{T}} = \bar{\bar{I}} \to \bar{\bar{T}}^T = \bar{\bar{T}}^{-1} \tag{4.4}$$

In the present study, all the basic rotation matrices relating each frame from flat Earth to blade axes correspond to eqs. (C.1) to (C.8) in appendix C. Because rotation preserves orthogonality, the properties above from linear algebra apply to these matrices.

4.3 Model of Dynamics

The model of dynamics used to simulate the motion of the blade is classified into different categories: kinematics, inertia, Earth, friction and aerodynamics. These are described in the next sections.

4.3.1 Kinematics

Assuming cruise stage in straight forward flight and constant rotor shaft revolutions with time, the rotor (R) angular velocity is first defined.

$$\vec{\omega}_{R,1} = \begin{bmatrix} 0 \\ 0 \\ \Omega \end{bmatrix} \cdot \begin{Bmatrix} \vec{i}_1 \\ \vec{j}_1 \\ \vec{k}_1 \end{Bmatrix} \tag{4.5}$$

Regarding the hinge (H), its position is given radially by the eccentricity and its linear velocity and acceleration correspond to the time derivatives.

$$\vec{r}_{H,1} = \begin{bmatrix} e_h \\ 0 \\ 0 \end{bmatrix} \cdot \begin{Bmatrix} \vec{i}_1 \\ \vec{j}_1 \\ \vec{k}_1 \end{Bmatrix} \tag{4.6}$$

$$\vec{v}_{H,1} = \dot{\vec{r}}_{H,1} = \vec{\omega}_{R,1} \times \vec{r}_{H,1} = \begin{bmatrix} 0 \\ \Omega e_h \\ 0 \end{bmatrix} \cdot \begin{Bmatrix} \vec{i}_1 \\ \vec{j}_1 \\ \vec{k}_1 \end{Bmatrix} \tag{4.7}$$

$$\vec{a}_{H,1} = \dot{\vec{v}}_{H,1} = \vec{\alpha}_{R,1} \times \vec{r}_{H,1} + \vec{\omega}_{R,1} \times \vec{v}_{H,1} = \begin{bmatrix} -\Omega^2 e_h \\ 0 \\ 0 \end{bmatrix} \cdot \begin{Bmatrix} \vec{i}_1 \\ \vec{j}_1 \\ \vec{k}_1 \end{Bmatrix} \tag{4.8}$$

Respect to the blade (B), which is joined to the rotor head by the hinge, the angular velocity and acceleration are defined by the rotor shaft speed and the time derivatives of the lagging ξ, flapping β and feathering θ angles. In the case of the C.30 autogiro, there is no variable pitch (i.e. θ remains constant in time). As a reminder, β had been defined negative in the Hx_4 direction for convenience.

$$\vec{\omega}_{B,4} = \left[\bar{\bar{T}}_{1\to4} \cdot \vec{\omega}_{R,1} + \bar{\bar{T}}_{2\to4} \cdot \begin{bmatrix} 0 \\ 0 \\ \dot{\xi} \end{bmatrix} + \bar{\bar{T}}_{3\to4} \cdot \left(\begin{bmatrix} 0 \\ -\dot{\beta} \\ 0 \end{bmatrix} + \begin{bmatrix} \dot{\theta} \\ 0 \\ 0 \end{bmatrix} \right) \right] \cdot \begin{Bmatrix} \vec{i}_4 \\ \vec{j}_4 \\ \vec{k}_4 \end{Bmatrix} \tag{4.9}$$

$$\vec{\alpha}_{B,4} = \dot{\vec{\omega}}_{B,4} = \left[\bar{\bar{T}}_{1\to4} \cdot \vec{\alpha}_{R,1} + \bar{\bar{T}}_{2\to4} \cdot \begin{bmatrix} 0 \\ 0 \\ \ddot{\xi} \end{bmatrix} + \bar{\bar{T}}_{3\to4} \cdot \left(\begin{bmatrix} 0 \\ -\ddot{\beta} \\ 0 \end{bmatrix} + \begin{bmatrix} \ddot{\theta} \\ 0 \\ 0 \end{bmatrix} \right) \right] \cdot \begin{Bmatrix} \vec{i}_4 \\ \vec{j}_4 \\ \vec{k}_4 \end{Bmatrix} \tag{4.10}$$

As a rigid body, the CoM also needs to be characterised to describe the motion of the blade by means of a single point. Its position is assumed to lie on the longitudinal axis with negligible deviation in the blade cross-section plane.

$$\vec{r}_{cm,4} \approx \begin{bmatrix} x_{cm} \\ 0 \\ 0 \end{bmatrix} \cdot \begin{Bmatrix} \vec{i}_4 \\ \vec{j}_4 \\ \vec{k}_4 \end{Bmatrix} \tag{4.11}$$

$$\vec{v}_{cm,4} = \dot{\vec{r}}_{cm,4} = \vec{\omega}_{B,4} \times \vec{r}_{cm,4} \tag{4.12}$$

$$\vec{a}_{cm,4} = \dot{\vec{v}}_{cm,4} = \vec{\alpha}_{B,4} \times \vec{r}_{cm,4} + \vec{\omega}_{B,4} \times \vec{v}_{cm,4} \tag{4.13}$$

4.3.2 Inertia

Inertia describes the tendency to resist changes in the state of rest or motion and it plays a crucial role in the dynamics of rigid bodies. While in rotation, it depends on the spinning velocity, the relative position of the object (including time derivatives) and the characteristics of the object. The next two subsections detail how mass is distributed to give the blade inertia tensor and the forces and moments produced by inertial forces.

4.3.2.1 Tensor

The moment caused by inertial forces when rotating depends on how the mass of a body is distributed, which can be mathematically expressed by means of a summation. Let the masses m_j be located at $\vec{r}_j$ and a perpendicular distance $r_{j\perp i}$ to axis i. The moment of inertia I about i is:

$$I_i = \sum_j \left(m_i r_{j\perp i}^2 \right) \tag{4.14}$$

From continuum mechanics, integration over the surface can be used instead if the mass distribution is known. Furthermore, the mass can be rewritten in terms of the planar density σ and the orthogonal area A to the axis in question.

$$I_i = \int_S r_{j\perp i}^2 dm = \int_S r_{j\perp i}^2 \sigma dA \tag{4.15}$$

Let the blade span, the chord and the thickness be notated as b, c and t, respectively. Assuming uniform density of the blade and approximating the geometry to a long rectangular flat plate ($b \gg c \gg t$), the moments of inertia about the three principal axes with respect to the hinge (namely $I_{x,4}$, $I_{y,4}$ and $I_{z,4}$) are deduced. With the linear density λ_i defined as the blade mass over the corresponding length on axis i, then:

$$I_{x,4} = \iint_{y,z} \left(y_4^2 + z_4^2\right) \sigma dz dy \approx \int_{-\frac{c}{2}}^{\frac{c}{2}} y_4^2 \lambda_y dy = \frac{m}{c} \int_{-\frac{c}{2}}^{\frac{c}{2}} y_4^2 dy = \frac{1}{12} m c^2 \tag{4.16}$$

$$I_{y,4} = \iint_{x,z} \left(x_4^2 + z_4^2\right) \sigma dz dx \approx \int_0^b x_4^2 \lambda_x dx = \frac{m}{b} \int_0^b x_4^2 dx = \frac{1}{3} m b^2 \tag{4.17}$$

$$I_{z,4} = \iint_{x,y} \left(x_4^2 + y_4^2\right) \sigma dy dx \approx I_{y,4} + I_{z,4} \approx \frac{1}{3} m \left(b^2 + \frac{c^2}{4}\right) \tag{4.18}$$

As a consequence of the geometry assumption, one can observe that further simplification is still possible: $I_{x,4} \ll I_{y,4} \approx I_{z,4}$. From eq. (4.17) and table 3.1:

$$I_{y,4} \approx 217 \left[kg \cdot m^2\right]$$

So the numerical computations will neglect the moment of inertia about the blade longitudinal axis and equate the other two for simplicity. The inertia tensor $\bar{\bar{I}}_{H,4}$ of the blade is consequently obtained from all the assumptions made.

$$\bar{\bar{I}}_{H,4} = \begin{bmatrix} I_{x,4} \\ I_{y,4} \\ I_{z,4} \end{bmatrix} \cdot \begin{Bmatrix} \vec{i}_4 \\ \vec{j}_4 \\ \vec{k}_4 \end{Bmatrix} \approx I_{y,4} \begin{bmatrix} 0 \\ 1 \\ 1 \end{bmatrix} \cdot \begin{Bmatrix} \vec{i}_4 \\ \vec{j}_4 \\ \vec{k}_4 \end{Bmatrix} \tag{4.19}$$

4.3.2.2 Forces & Moments

In a non-inertial reference frame, Newton's second law from classical mechanics, stated in eq. (4.20), is not sufficient to describe the motion of a body by means of the external or real forces (F).

$$\sum \vec{F} = m\vec{a} \tag{4.20}$$

The reason is due to the acceleration of the non-inertial system —by mere definition— with respect to an inertial one. Introduced in eq. (4.21), additional forces (F_I) derived from that relative acceleration determine the motion: they are known as *inertial*, *fictitious*, *d'Alembert* or *pseudo forces*.

$$\sum \vec{F} + \sum \vec{F}_I = m\vec{a} \tag{4.21}$$

The same principle applies to moments, that are obtained multiplying by a length. The force and moment on the blade origin (the hinge) are then defined as:

$$\vec{F}_{H,4} = -m\ \bar{\bar{T}}_{1\to 4} \cdot \vec{a}_{H,1} \tag{4.22}$$

$$\vec{M}_{H,4} = \vec{r}_{cm,4} \times \vec{F}_{H,4} \tag{4.23}$$

The study case in question will be approached by means of Euler's equations, formulated for a rigid body under rotation. They already consider the non-inertial frame, hence the moments from inertial forces. However there is an exception: originally Euler's equations were set for a free rotating body and in this case it is constrained by the hinge. Consequently, the extended form of Euler's equations below introduces the moment on the hinge from eq. (4.23).

$$\bar{\bar{I}}_{H,4} \cdot \vec{\alpha}_{B,4} + \vec{\omega}_{B,4} \times \left(\bar{\bar{I}}_{H,4} \cdot \vec{\omega}_{B,4}\right) = \vec{M}_{H,4} \tag{4.24}$$

Equation (4.24) describes the rotation of the blade in the absence of any other external moments: it represents the inertia itself.

As any object undergoing rotation with external forces applied, it is not straightforward to visualise. For instance, when considering only the flapping motion in eq. (4.25), merging all external moments ($\bar{\bar{M}}_4$) just for a simple lookout and substituting $\varepsilon = \frac{me_h x_{cm}}{I_{y,4}}$, a torque on the lagging axis appears. It has a magnitude of $2I_{y,4}\Omega\dot{\beta}\beta$.

$$\begin{bmatrix} 0 \\ \ddot{\beta} + (1+\varepsilon)\,\Omega^2\beta \\ 2\Omega\dot{\beta}\beta \end{bmatrix} = -\frac{1}{I_{y,4}} \begin{bmatrix} M_{x,4} \\ M_{y,4} \\ M_{z,4} \end{bmatrix} \tag{4.25}$$

This is a consequence of Coriolis effects after introducing the flapping DoF. For the conservation of angular momentum, while the blade is flapping its radius of gyration must change. Therefore the blade is subjected to high stress levels at the root unless installing an additional hinge to allow this second DoF, lagging. Hence its main and justified purpose. In contrast, no effects are observed on other axes if looking only at the lagging motion in eq. (4.26).

$$\begin{bmatrix} 0 \\ 0 \\ \ddot{\xi} + \varepsilon\Omega^2\xi \end{bmatrix} = -\frac{1}{I_{y,4}} \begin{bmatrix} M_{x,4} \\ M_{y,4} \\ M_{z,4} \end{bmatrix} \tag{4.26}$$

4.3.3 Earth

The Earth is assumed flat for simplicity since relative short distances are presumably covered by the gyroplane. The conservative field is yet governed by the gravitational acceleration g, which is taken at SL ($g \approx 9.80665\ m/s^2$). Thus, the weight and the moment that it exerts on the blade centre of mass are, respectively:

$$\vec{W}_E = m\vec{g} = mg \begin{bmatrix} 0 \\ -1 \\ 0 \end{bmatrix} \cdot \begin{Bmatrix} \vec{i}_E \\ \vec{j}_E \\ \vec{k}_E \end{Bmatrix} \tag{4.27}$$

$$\vec{M}_{W,4} = \vec{r}_{cm,4} \times \bar{\bar{T}}_{E\to 4} \cdot \vec{W}_E \tag{4.28}$$

4.3.4 Friction

The modified Coulomb's law will be used to model friction in the problem. It was previously stated in eq. (2.3) as well as the torque caused by friction in eq. (3.9). The combination of both will help to implement the concepts in a single equation that describes the actual torque from friction between disc and washer while solving the discontinuity problem, which is brought by the original Coulomb's model. Therefore, using some information from table 3.1, the resulting moment in the lagging frame will be defined as:

$$\vec{M}_{f,2} = \frac{8}{3}\frac{R_o^3 - R_i^3}{R_o^2 - R_i^2}\mu F_{comp} \begin{bmatrix} 0 \\ 0 \\ -\tanh\left(\frac{\dot{\xi}}{\dot{\xi}_0}\right) \end{bmatrix} \cdot \begin{Bmatrix} \vec{i}_2 \\ \vec{j}_2 \\ \vec{k}_2 \end{Bmatrix} \tag{4.29}$$

This expression basically returns opposite sign vectors (of constant magnitude) depending on the velocity direction of lagging motion. In rigorous terms, the friction is decreased for values that tend to zero, but the reference velocity $\dot{\xi}_0$ can be set very low to make an abrupt transition, thus assuming only a virtual discontinuity. Later on the convenient blade reference system will be used in the EoMs.

$$\vec{M}_{f,4} = \bar{\bar{T}}_{2\to 4} \cdot \vec{M}_{f,2} \tag{4.30}$$

4.3.5 Aerodynamics

This subpart of the dynamics model is focussed on building a consistent aerodynamics model to express the contribution to the moment on the blade. It is divided into four subsections: the first one presents some data to be used in the computations, the second subsection deduces the velocity components on a blade section, the third one details the aerofoil used and the fourth derives the expressions of the forces and moments due to aerodynamics.

4.3.5.1 Data

Together with some reference data from table 3.1, the constants needed for the model of aerodynamics are listed in table 4.2 below.

Notation	Value	Units	Definition
ρ	1.225	kg/m^3	Density of air (at SL & ISA)
μ	$1.789 \cdot 10^{-5}$	$kg/m/s$	Dynamic viscosity of air (at SL & ISA)
ν	$1.460 \cdot 10^{-5}$	m^2/s	Kinematic viscosity of air (at SL & ISA)
U_∞	$[10.7, 43.4]$	m/s	Airspeed range of aircraft (forward flight)

Table 4.2: Constants for the aerodynamics model [3].

4.3.5.2 Velocity Components

The relative air velocity on the blade is expressed in terms of the local aerodynamic components that give the parallel (chord-wise) and perpendicular directions to the blade at each span section. There are two airflow components to consider in the problem: one comes from the forward flight, which is assumed constant, and another results from the blade rotation. Therefore the airspeed U_∞ is added to the linear velocity of the blade section.

$$\vec{u}_{aero,4} = \left[\bar{\bar{T}}_{A\to 4} \cdot \begin{bmatrix} U_\infty \\ 0 \\ 0 \end{bmatrix} + \bar{\omega}_{b,4} \times \begin{bmatrix} e_h + x_4 \\ 0 \\ 0 \end{bmatrix} \right] \cdot \begin{Bmatrix} \vec{i}_4 \\ \vec{j}_4 \\ \vec{k}_4 \end{Bmatrix} \tag{4.31}$$

For the sake of simplicity in the computation, the radial component is completely ignored: the blade is radially constrained. Once obtained, these velocity components will be useful to define the effective angle of attack α_b, where small angle approximation is assumed.

$$\alpha_b = -\operatorname{atan}\left(\frac{\vec{u}_{aero,4} \cdot \vec{j}_4}{\vec{u}_{aero,4} \cdot \vec{i}_4} \right) \approx -\frac{\vec{u}_{aero,4} \cdot \vec{j}_4}{\vec{u}_{aero,4} \cdot \vec{i}_4} \tag{4.32}$$

Note that no geometric or aircraft AoAs are included in eq. (4.32), since they are implicit in the coordinate frame transformation, and that the sign had been defined negative in the Hx_4 direction. With this effective AoA the velocity components can now be transformed to the aerodynamic frame multiplying by $\bar{\bar{T}}_{4\to 5}$.

4.3.5.3 Aerofoil

According to the official documentation the aerodynamic profile used for the blades of the autogiro C.30 is the Göttingen (Gö) 606 [17]. But there is scant evidence about such an old fashion aerofoil; it must be studied in order to obtain its lift slope needed to implement the TAT.

The first step is to retrieve the visual information available presented as a sketch of the profile [17]. In a similar fashion, the sketch of a four-digit NACA is superposed to the Gö and compared upon similarity. By means of visual inspection, the profile parameters (camber and thickness) are modified until obtaining a geometry as similar as possible. The plot is created with an aerofoils database: *Airfoil Tools* [W1]. The profile to be used in the computations is the NACA 3316, which best adjusts to the Gö 606 geometry, as observed in fig. 4.2.

Figure 4.2: Superposed profiles: Gö 606 (thick black) & NACA 3316 (thin red).

With the computation software XFLR5 one can obtain the polars of an aerofoil governed by the TAT [23]. To comply with this theory, the whole study is based on the assumptions of a thin aerofoil and small blade angles of attack. So for a two-dimensional aerofoil the lift coefficient is calculated straightforward as in eq. (4.33) and the drag coefficient will be assumed as in eq. (4.34).

$$C_l = \frac{\partial C_l}{\partial \alpha_b} \left(\alpha_b - \alpha_{b,l=0}\right) \tag{4.33}$$

$$C_d = C_{d,0} + k \left(C_l - C_{l,ideal}\right)^2 \tag{4.34}$$

The constants involved in the lift coefficient are the lift slope, $\partial C_l / \partial \alpha_b$, and the zero-lift AoA, $\alpha_{b,l=0}$. With regard to the drag coefficient, the first element, $C_{d,0}$, corresponds to the parasite drag, which coincides with the minimum drag, and the second element is the drag-due-to-lift, which is affected by a viscous factor k and the ideal lift coefficient at minimum drag, $C_{l,ideal}$. Note that a wing (3D) would include an additional term called induced drag, generated by the downwash from the wing-tip vortices. However, that will not be considered in this model and the assumption of a 2D-flow will prevail.

After dimensioning the NACA 3316, the numerical analysis is run for a defined sequence of blade angles of attack α_b and the desired increment. The Reynolds numbers used in the aerofoil analysis were calculated for the blade maximum airspeed[1] at four equally spaced sections (r) along the blade span.

$$Re = \frac{\rho V c}{\mu} = \frac{V c}{\nu} \tag{4.35}$$

$$V(r) \approx U_\infty + \Omega \cdot r \tag{4.36}$$

And the numerical computation finally returns the polars where the constants are obtained from. They are listed in table 4.3 and plotted in fig. C.1, appendix B.

[1]Reynolds numbers were computed for the maximum possible speeds in forward flight: at maximum flight airspeed when the blade is advancing with the chord parallel to the airflow.

Term	Value	Units	Definition
$\frac{\partial C_l}{\partial \alpha_b}$	1.8π	deg^{-1}	Lift slope
$\alpha_{b,l=0}$	-2.7	deg	AoA at zero-lift
$C_{d,0}$	0.007	–	Parasite drag
$C_{l,ideal}$	0.385	–	Ideal lift coefficient (at minimum drag)
k	0.00678	–	Viscous factor

Table 4.3: Aerodynamic constants of lift & drag polars.

4.3.5.4 Local Force & Moment about Hinge

The lift L' and drag D' forces can be locally calculated at each element (along the blade relative wind axes z_{aero} and y_{aero} respectively) if a differential of length dx_4 is taken along the blade span x_4. The centre of pressure is assumed to coincide with the longitudinal axis where the CoM lies too. As a reminder, the chord y_b in this case remains constant. The goal is to obtain the actual force F_{aero} from lift and drag components as a function of the longitudinal position. The velocity components from eq. (4.31) are used to compute the forces.

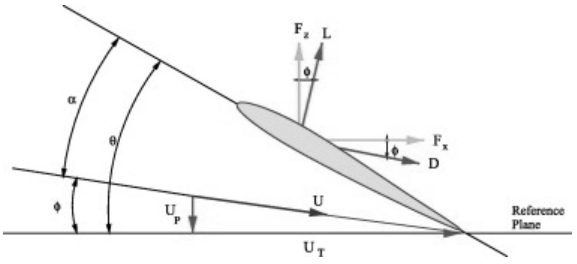

Figure 4.3: Blade element velocities & forces [18].

$$d\vec{F}_{aero,5} = d\vec{L}' + d\vec{D}' = \frac{1}{2}\rho|\vec{u}_{aero,5}|^2 y_b dx_4 \begin{bmatrix} 0 \\ -C_d \\ C_l \end{bmatrix} \cdot \begin{Bmatrix} \vec{i}_5 \\ \vec{j}_5 \\ \vec{k}_5 \end{Bmatrix} \tag{4.37}$$

The differential of moment dM_{aero} about the hinge is simply obtained after multiplying by the position x_4. For convenience, the force will be expressed in the blade frame, that way the moment is directly decomposed in the main directions (lagging, flapping and feathering).

$$d\vec{M}_{aero,4} = \vec{x}_4 \times \bar{\bar{T}}_{5\to4} \cdot d\vec{F}_{aero,5} \tag{4.38}$$

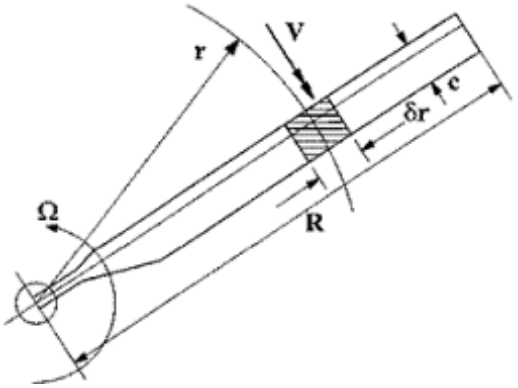

Figure 4.4: Conceptual illustration of BET: blade & span differential [W15].

Finally, in accordance to the BET the moment caused by the aerodynamic forces results from the integration along the span. The hinge is assumed to have no eccentricity since it is much smaller compared to the radius of the rotor disc ($e_h \ll R$), which significantly simplifies the computation costs and the error can be neglected.

$$\vec{M}_{aero,4} = \int_0^R d\vec{M}_{aero,4} \tag{4.39}$$

Unexpectedly, when operating with the Symbolic Math Toolbox™ in MATLAB the integration returned no output due to complexity of the frame transformations (lengthy algebra). As the issue persisted, an alternative way had to be found in the attempt of integrating along the span.

The proposed solution was the trapezoidal method [W9], which approximates the definite integral numerically by dividing the interval into a finite number of trapezoids, whose areas are summed. For a space of N divisions along a variable x the trapezoidal integration of a function $f(x)$ is expressed as:

$$\int_a^b f(x)dx \approx \frac{1}{2}\sum_{n=0}^{N-1}\left[(x_{n+1}-x_n)\left(f(x_n)+f(x_{n+1})\right)\right] \tag{4.40}$$

Note that as N tends to infinity, the classical definition of the integral is obtained. When the divisions are equally spaced, the formula can be further simplified:

$$\int_a^b f(x)dx \approx \frac{b-a}{2N}\sum_{n=0}^{N-1}\left[f(x_n)+f(x_{n+1})\right] \tag{4.41}$$

Hence eq. (4.39) in the methodology was eventually replaced by eq. (4.42) as an alternative procedure with a small space division of the blade span for the sake of accuracy ($N = 100$).

$$\vec{M}_{aero,4} = \int_0^R d\vec{M}_{aero,4} \approx \frac{R}{2N}\sum_{n=0}^{N-1}\left[\vec{M}_{aero,4}(x_n)+\vec{M}_{aero,4}(x_{n+1})\right] \tag{4.42}$$

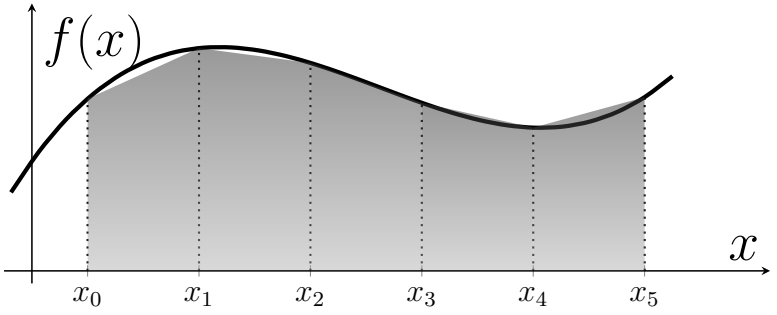

Figure 4.5: Graphical representation of trapezoidal method.

4.4 Equations of Motion

Finally, introducing the external moments from eqs. (4.28), (4.30) and (4.39) into the extended Euler's equations in eq. (4.24) results in:

$$\bar{\bar{I}}_{H,4} \cdot \vec{\alpha}_{B,4} + \vec{\omega}_{B,4} \times \left(\bar{\bar{I}}_{H,4} \cdot \vec{\omega}_{B,4} \right) = \vec{M}_{H,4} + \vec{M}_{W,4} + \vec{M}_{f,4} + \vec{M}_{aero,4} \tag{4.43}$$

Equation (4.43) contains the set of algebraic equations in the blade frame that close the problem. It will be used to study the oscillatory motions about the principal directions of the blade.

4.5 Software

The scope of the mathematical study is solving and plotting eq. (4.43), which is a set of differential algebraic equations (DAEs). For this task of numerical analysis the software used will be MATLAB.

However, most of the systems involving DAEs are not convenient for direct input to this mathematical coding language. Indeed, all the transformations used add complexity to the problem with lengthy algebra; the DAEs must be rewritten to an equivalent suitable expression through ordinary differential equations (ODEs). Notwithstanding, with the Symbolic Math Toolbox™ supplied it is possible to manipulate symbolic mathematical equations, which will result particularly useful when working with a set of DAEs. According to MathWorks, the developer: specific functions can "reduce the differential index of the DAEs (number of differentiations needed to reduce the system to ODEs) and convert the system to numeric function handles suitable for MATLAB solvers."

4.6 Results & Discussion

The flapping and lagging motions are described and discussed in this section. The results are presented as plots of the corresponding angles along a rotor revolution (steady auto-rotation) in terms of the tip speed ratio μ.

$$\mu = \frac{U_\infty \cos(\alpha)}{\Omega R} \tag{4.44}$$

Table 4.4 shows the tip speed ratios selected for the analysis. A constant incidence angle ($\alpha = 30^o$) was assumed.

Airspeed (U_∞)		**Rotor Speed (Ω)**		**Tip Speed Ratio (μ)**
[**mph**]	[**m/s**]	[**rpm**]	[**rad/s**]	[–]
24.6	11.0	170	17.8	0.055
34.9	15.6	180	18.8	0.073
45.2	20.2	190	19.9	0.090
55.5	24.8	200	20.9	0.105
65.8	29.4	210	22.0	0.119
76.1	34.0	210	22.0	0.137
86.4	38.6	210	22.0	0.156
96.6	43.2	210	22.0	0.174

Table 4.4: Tip speed ratios.

4.6.1 Flapping Motion

The flapping motion was studied after retrieving the flapping angle along time. Small angle approximations were considered and the effect of lagging on flapping was neglected in the approach according to the rationale in eqs. (4.25) and (4.26). Figures C.2 to C.9 in appendix C show the results obtained in MATLAB, expressed as revolutions for convenience since the rotor speed was assumed constant. At approximately 30 revolutions the convergence of the numerical computation is observed, where the blade flapping reaches the steady equilibrium state and time can be eliminated in the problem. The following discussion focusses on such domain.

A tip speed ratio is first selected: for instance the one in the set that happens at maximum airspeeds close to 100 mph, which can be compared to existing experimental studies. The corresponding flapping is represented in fig. 4.6.

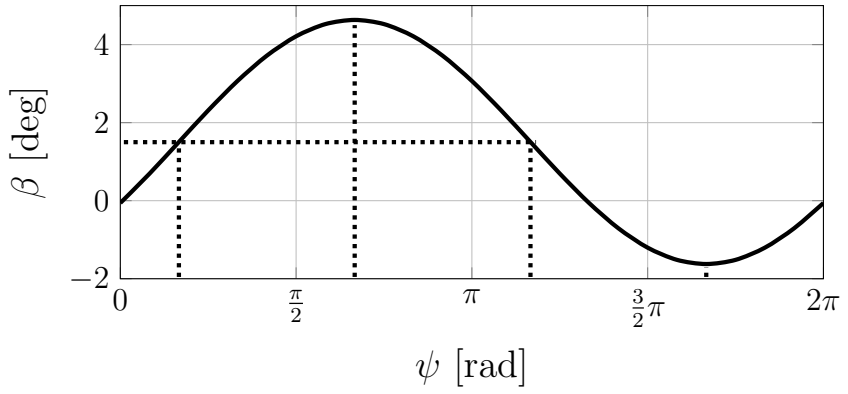

Figure 4.6: Blade flapping angle for a revolution under auto-rotation at $\mu = 0.174$.

From the plot, different points can be identified with a maximum amplitude of nearly 3º. The minimum angle falls roughly 2º below the horizontal plane, perpendicular to the rotor axis, whereas the maximum is lifted up to about 4.5º. Two inflexion points are found right in between, locating the offset at 1.5º, at the azimuthal angles 30º and 210º respectively. As a reminder, β had been defined negative in the Hy_2 direction (flapping axis), i.e. moving upwards.

In the first instance, comparison with experimental research from the official report [12] suggests acceptable points recorded in steady flight that may be fitted to the expansion. A 'ciné' camera was mounted on the rotor head and rotated with it (see fig. C.18 in appendix C). It was pitched up about 1.5º above the plane perpendicular to the rotation axis and it allowed to measure positions marked along the blade at the shots instants. But the main drawback was that no external reference in the pictures could be taken as datum for flapping and the azimuth angles.

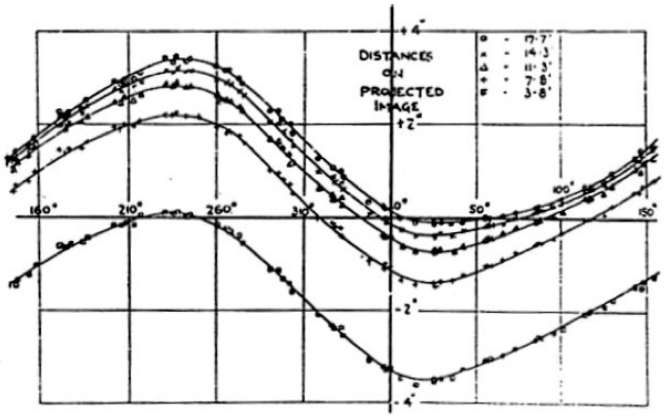

Figure 4.7: Experimental data [12]: flapping motion distance (in inches) of 5 spaced marks along the blade VS azimuth angle. Motion perpendicular to plane of rotation.

The evolution along a cycle from fig. 4.6 shows a sinusoidal behaviour, in a similar way to the experimental data from fig. 4.7. In fact, according to a wide variety of existing research, like Wheatley's report *An aerodynamic analysis of the autogyro rotor with a comparison between calculated and experimental results* [24], under auto-rotation conditions the flapping angle is a periodic function of the azimuth, naturally leading to a Fourier series:

$$\beta(\psi) \sim \frac{a_0}{2} + \sum_{n=1}^{\infty} [a_n \cos(n\psi) + b_n \sin(n\psi)] \tag{4.45}$$

The author claims that "all harmonics above the second are found experimentally to be negligible" and that statement is further proved numerically in [16]. If solving for the corresponding coefficients, a similar behaviour would be found, but that will not be the scope for now. Evidence is provided by fig. 4.8 instead.

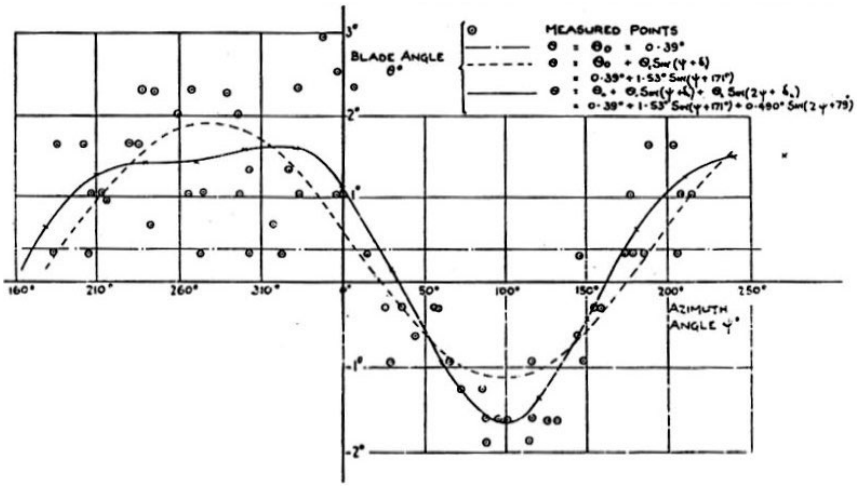

Figure 4.8: Comparison of experimentally measured blade angles (at 90mph) with Fourier series representing them [12].

Regarding a wide range of airspeeds in auto-rotative regime, the flapping angles obtained with MATLAB are superposed in a single plot, fig. 4.9, which helps observing the role of different tip speed ratios. One can presumably identify the first harmonic nature of the numerically obtained results: if reproduced by a Fourier series, then all elements for $n > 1$ would be presumably zero. On one hand, this supports the rationale of Fourier expansions in the steady state. On the other hand, it differs from experimental results found in [24] since the second harmonic is not present in fig. 4.9. The difference with the experimental results might be related to assumptions made in this model, like uncoupled motion, infinite blade span for the aerodynamics model and smooth undisturbed flow.

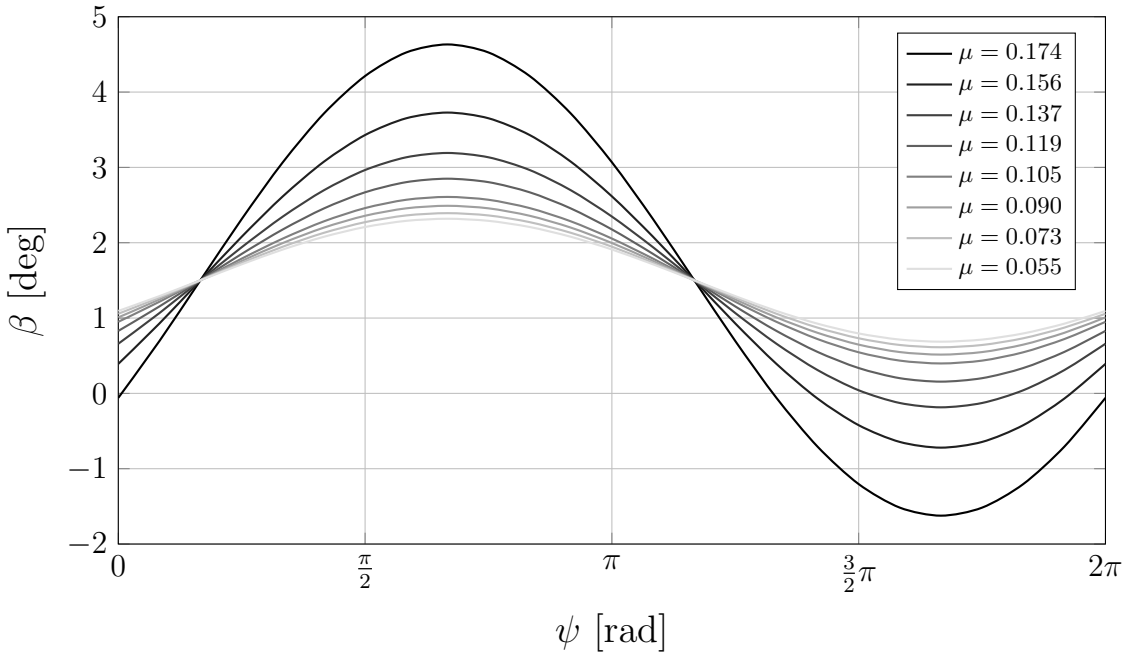

Figure 4.9: Blade flapping angle for a revolution under auto-rotation at different tip speed ratios.

Another remarkable aspect is the invariable frequency (only in the steady state) and offset at 1.5º from the rotation plane for all tip speed ratios. Only the amplitude seems to increase for higher ratios as the aerodynamics becomes dominant over the centrifugal force. Nonetheless, the blade does not exceed a maximum amplitude of nearly 3º approximately, which supports the small angle approximation made.

The torque evolution was omitted in the study, as explained in previous sections, due to the the constant rotor speed in steady motion. Indeed, it must be zero since the aerodynamic forces providing positive and negative torque contributions must balance out to achieve such conditions in flight [16]. So it is not meaningful in the steady auto-rotation, however detailed attention should be paid in a dynamic analysis out of the steady condition: among other reasons, it might cause undesired lateral forces compromising the stability of the gyroplane.

From a 3D view, for the sake of visual understanding, a model originally developed by MathWorks was further modified in virtue of the present study. It uses MATLAB to describe the harmonics of a rotor as a whole. So three blades were used in the model and their path was adapted to flapping motion like the one observed in fig. 4.6 for high airspeeds. The 3D representation (not scaled) is reproduced in fig. 4.10a.

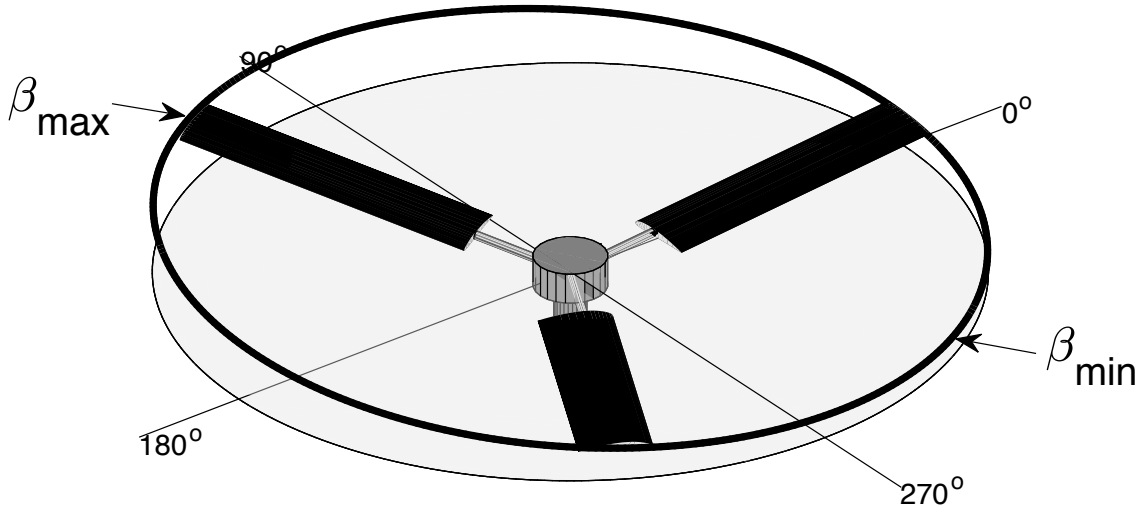

(a) Generic blade tip path described.

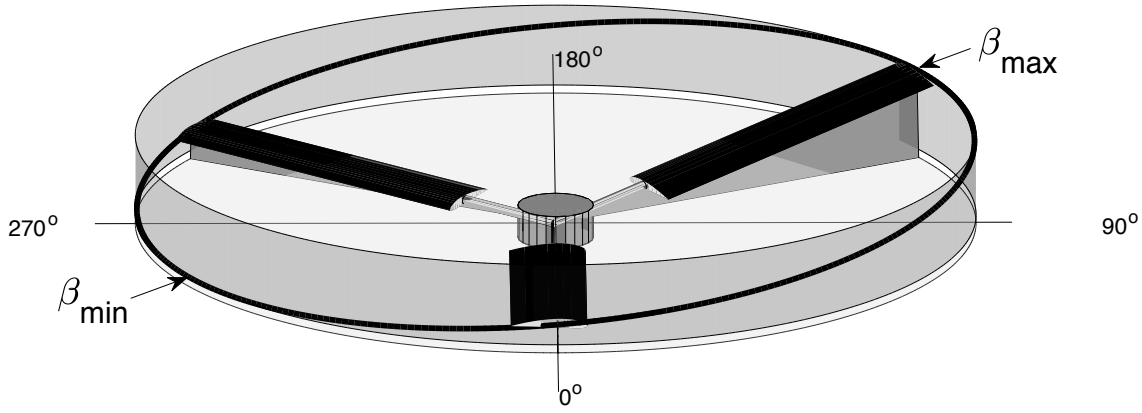

(b) Flapping angles at lower forward airspeeds.

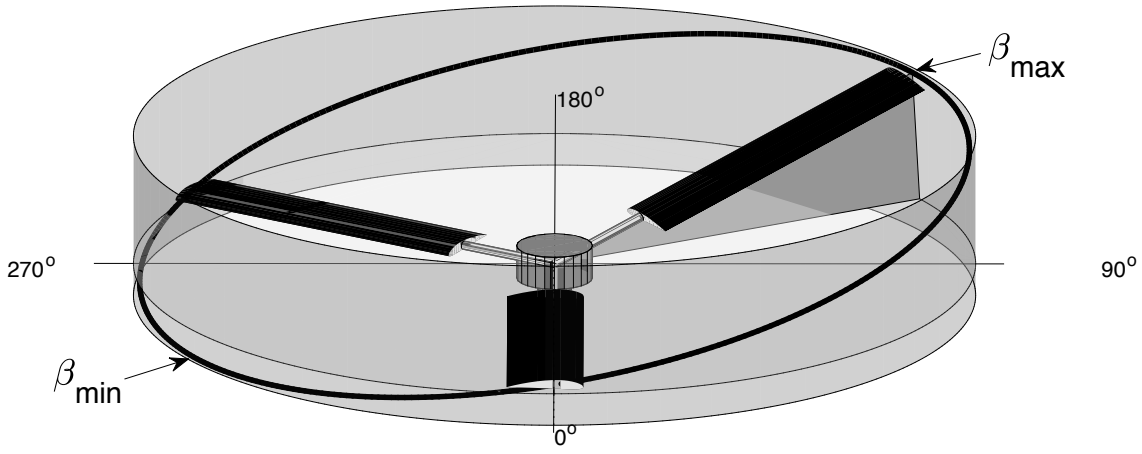

(c) Flapping angles at higher forward airspeeds.

Figure 4.10: 3D representation of rotor blades flapping in steady forward flight.

In forward flight heading to 180º, one can directly observe in fig. 4.10a the tip path plane, whose intersection with the rotor disc cylinder traces the same path for all the blade tips. This plane is also known as the 'axis-of-no-flapping' [6] and it is only valid for the first flapping harmonic —note from fig. 4.6 that such an ideal case does not occur in real life—. If the hinge is offset, then the axis-of-no-flapping does not exist any more. However for small offsets it can still be considered as an inclination approximately equal to the flapping angle, with a small error from the assumption. The azimuthal offset of the plane ($\pi/6$ rad) can also be distinguished by the maximum and minimum flapping angles projections on the plane perpendicular to the rotor axis. These are pointed out in fig. 4.10.

As already seen in the results from fig. 4.9, high airspeeds involve higher flapping angles, as depicted in fig. 4.10c. In contrast, lower airspeeds translate into governing centrifugal force over aerodynamic forces, with decreasing flapping angles as illustrated in fig. 4.10b.

Just as a final remark which is out of the scope of the analysis, supposing a vertical descent the lift distribution would become symmetric on the rotor disc. Then the tip path plane would be perpendicular to the rotor shaft and the cyclic flapping motion would disappear consequently as the angle would tend to a constant value. Figure 4.11 represents that behaviour.

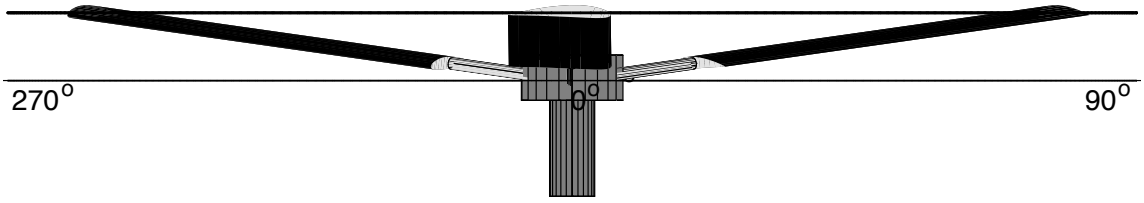

Figure 4.11: Blade tip path in vertical descent.

4.6.2 Lagging Motion due to Flapping

As a consequence of flapping, Coriolis forces act on the blade while moving up and down. Recalling eq. (4.25) that describes the isolated flapping motion, one can identify the term causing an acceleration on the lagging axis:

$$\begin{bmatrix} 0 \\ \ddot{\beta} + (1+\varepsilon)\,\Omega^2\beta \\ 2\Omega\dot{\beta}\beta \end{bmatrix} = -\frac{1}{I_{y,4}} \begin{bmatrix} M_{x,4} \\ M_{y,4} \\ M_{z,4} \end{bmatrix} \tag{4.25}$$

It depends directly on both the flapping angle and its first time derivative, which makes it rather not intuitive at a first glance.

In a similar fashion to the previous flapping analysis, the lagging motion was studied after retrieving the lagging angle along time. Again small angle approximations were considered. Figures C.10 to C.17 in appendix C show the results obtained in MATLAB, expressed as revolutions for convenience since the rotor speed was assumed constant. At approximately 30 revolutions the convergence of the numerical computation is observed, like in the flapping oscillation, where the blade flapping reaches the steady equilibrium state and time can be eliminated in the problem. Such domain will be the focus of discussion in the next lines.

The case for maximum airspeed (close to 100 mph) is selected once again. Represented in fig. 4.12, the second harmonic is present, showing positive increment from the azimuthal origin to past half a revolution, where it decreases up to practically the completion of the cycle. At the corresponding tip speed ratio, the maximum lagging angle is nearly 5°, the maximum amplitude is around 0.5° and the offset is found at 4.5° from the azimuth angular position. A remarkable aspect with respect to flapping in fig. 4.6 is that lagging is exactly phased by 90°. As a reminder, ξ had been defined negative in the Hz_1 direction (lagging axis), i.e. moving backwards, opposite to the rotor angular velocity.

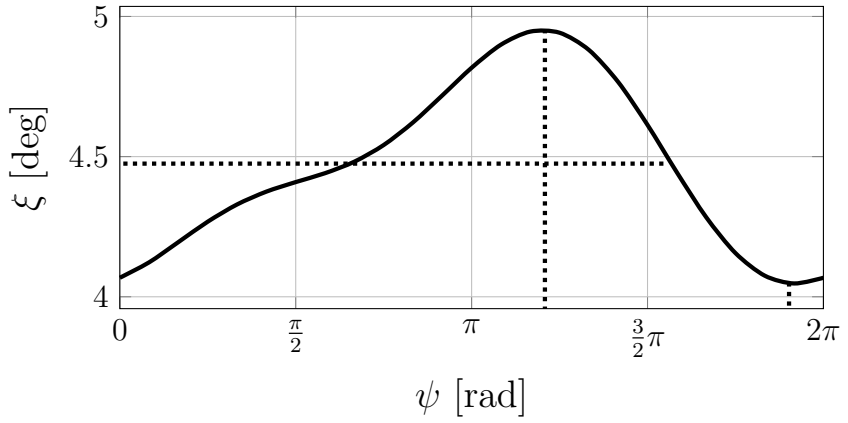

Figure 4.12: Blade lagging angle for a revolution under auto-rotation at $\mu = 0.174$.

Comparison upon experimental data from the technical report [12] shows the nature of the second harmonic, in agreement with the numerically results obtained for the respective airspeeds. There exists one difference with fig. 4.13 though: the plots are mirrored. This can be argued by the selection of a counter-clockwise rotor angular velocity (from a top view) in the present study —intentionally to comply with the right hand rule—. The original C.30 autogiro had a clockwise spinning rotor, but for the analysis in question that was not relevant due to symmetry.

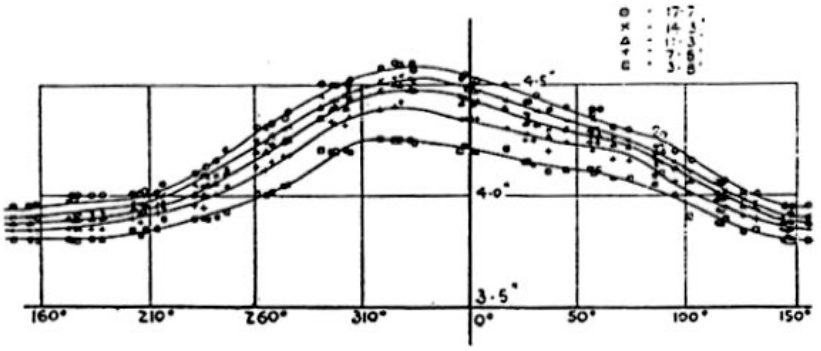

Figure 4.13: Experimental data [12]: lagging motion distance (in inches) of 5 spaced marks along the blade VS azimuth angle. Motion perpendicular to plane of rotation.

Now looking at a range of airspeeds under auto-rotation, the angles obtained with MATLAB are superposed in fig. 4.14 to analyse the effect of different tip speed ratios. Compatibility with the second harmonic according to Fourier expansions is present now, which agrees with Wheatley's study [24].

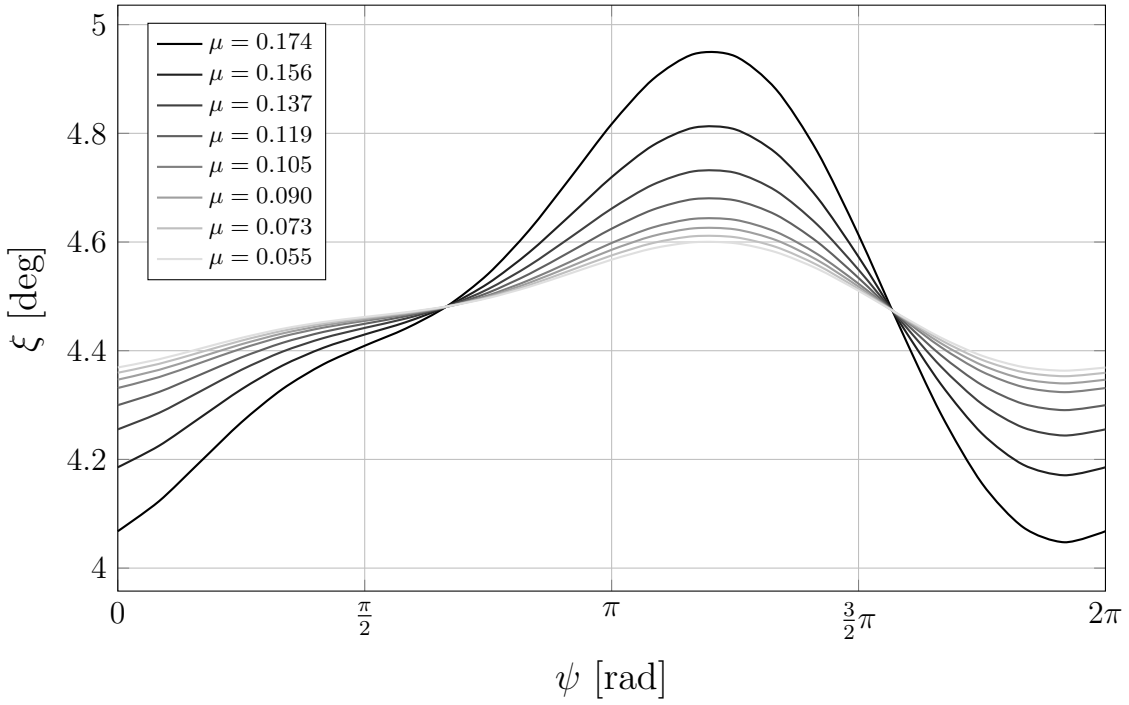

Figure 4.14: Blade flapping angle for a revolution under auto-rotation at different tip speed ratios.

From fig. 4.14 one can observe the constant oscillation frequency (only under steady auto-rotation) with an oscillation angle offset at approximately 4.5º (behind the hinge radial axis). The highest angle occurs at higher tip speed ratios and it is roughly 5º, which supports the small angle approximation made in the study. Likewise, the maximum increment found at higher speeds is about 1º, which gives credit to the assumption of no interference on the flapping motion; in real life that is not true, they are inherently coupled [6]. Lower tip speed ratios are dominated by the centrifugal force instead, decreasing the amplitude of the lagging angle in a similar way to the flapping motion: the amplitude decreases asymptotically to zero as the airspeeds also tend to zero.

4.6.3 Validity & Limitations

The validity of the results, based on the simulation model analytically defined and numerically computed, is supported by the experimental results from the (official) autogiro technical report [12] and further experimental research on it [24].

The limitations of this study, however, become significant in that the dependency on time was dispensable as it focussed on steady auto-rotation, under forward flight scenario. More advanced models could add more variables to the problem, like the rotor speed and the free air-stream incidence angle, in order to analyse their relation and find more accurate results. Different flight scenarios and physics perturbations ought to be considered in the endeavour of studying the system response, especially to find resonance frequencies —very important at design levels to ensure safety—.

Furthermore, as Wheatley states in [24]: "The aerodynamic analysis developed by Glauert and Lock is quantitatively usable except for the blade motion. The blade motion is critically dependent upon the distribution of the induced velocities over the rotor disc and cannot be calculated rigorously without the accurate determination of the induced flow." This suggests a noticeable discrepancy between the real aerodynamics and the aerodynamic model used in this study, which ignored the induced flow and assumed no interference between blades due to ideal fluid flow. Notwithstanding, the model was proven to converge at steady equilibrium state and it may be validated within the theoretical framework as long as no perturbations or other external forces come into play.

From the structural point of view, the elimination of stiffness also diminished complexity of the problem. In practice this is another significant source of vibrations that may lead to failure under specific circumstances, for which stability boundaries are confined [6].

5 Conclusion

Asociación Juan de la Cierva Codorníu (AJCC) is devoted to the reconstruction of a commemorative replica of the C.30 autogiro to be flown in national aeronautic exhibitions. In collaboration with the association, the project focussed on two related tasks: the research on a material for the disc of the friction damper and its validation through the design of a model that reproduced the motion of the blade in the steady forward flight.

With regard to the material of the friction disc, a research on the thermo-mechanical properties was made to identify the ones that play a decisive role: density, friction coefficient, compressive strength, tensile strength, specific heat and thermal conductivity. Then the modified digital logic (MDL) was proposed to weight those properties and minimise subjectivity from the problem. Afterwards, a number of candidate materials were listed and they were filtered according to the overall performance, considering the cost as an additional criteria. The materials list included aluminium (Al) alloys, steel alloys, titanium (Ti) alloys, cast iron and ceramic composites. The results showed the cast Al alloys to be a potential candidate material for the friction damper disc of the C.30 autogiro. Specifically, aluminium alloy 356.0 shows the optimum balance between performance and cost, with the ones from series $3xxx$, $5xxx$, $7xxx$ and $8xxx$ decreasing the performance in less than 15%. A full list was provided with the variations in performance and cost of each material with respect to the one proposed.

As for the simulation of the blade motion, the assumptions were listed in the first instance and the reference frames were defined with their corresponding transformation matrices. Then the kinematics were expressed and Euler's equations for the inertia written for a rigid body in rotation. The terms corresponding to the external or real forces involved were finally characterised with a flat Earth model, for gravity, a friction model based on Coulomb's friction law for the damper and an aerodynamics model that made use of the thin aerofoil theory (TAT) and the blade element theory (BET). The numerical results proved consistency with the analytical formulation, where the lagging motion was affected by flapping with a phase difference of 90º. Besides, both oscillations had the same frequency as the one of the rotor shaft, in agreement with theoretical background [12, 24] that proposes Fourier's expansions to approach the cycling as a sinusoidal function of the azimuthal angle. When comparing results at different airspeeds, higher amplitudes were found for higher tip speed ratios, which is explained by dominating aerodynamic effects over inertial effects. Further comparison with experimental results [12, 24] supports the consistency of the model when simulating the blade motion in steady forward flight.

In conclusion, **the material proposed is aluminium alloy 356.0, which proves to successfully meet the friction damping requirements for the steady auto-rotation of the Cierva C.30 autogiro with an optimal balance between performance and cost**.

Finally, with the main objectives accomplished, the study relies on a concise set of assumptions that opens a wide range of future lines of research:

Concerning the material proposed, essentially four main matters would consolidate the basis of the research. The first and most important one regards an in-depth thermal study to validate the material upon its thermal performance, since the validation of the present study was founded on the mechanics point of view. This would consolidate the basis of the project and prevent possible failure related to thermal deficiency. The other three matters are related to more detailed investigation on tribology properties, manufacturing techniques that may affect the material selection and direct enquiry to suppliers and/or manufacturers to have a closer estimation of the cost.

Respect to the blade motion, a more in-depth dynamic analysis would provide broader understanding about the motions distinguished. That would involve expanding the study beyond the assumption of steady auto-rotation. Further studies might also consider finite blade rigidity, for instance, a more realistic aerodynamics model (3D non-ideal flow, wake interference between rotor blades...) and the oscillations transmitted to the fuselage. Another remarkable aspect would be implementing the flight equations to model the flight dynamics of the gyrocopter. That would allow to simulate different scenarios (take-off, landing, manoeuvring, perturbations...) that may be crucial in terms of aircraft safety during operation.

6 Project Planning & Budget

6.1 Project Planning

The schedule followed in the project splits into seven stages along the semester. Figure D.1 in appendix D shows the distribution over the six months where the following tasks were developed. It does not necessarily coincide with the actual time spent in hours, which is shown next in table 6.1.

i. **Background and problem definition:** historical records of the invention were gathered in the first place to get familiar with the topic. Then the background and the context were set as a working scenario. At the same time, the project scope was defined together with the structure that would delineate the guidelines to be followed in the course of the study.

ii. **Documentation collection and research:** the old official documentation was collected; original documents supplied by AJCC. Likewise, regulations, existing knowledge and related research on similar projects were gathered and processed in order to summarise and contextualise the information in accordance to the established guidelines. This would facilitate decisions on later methodological procedure from a scientific approach.

iii. **Model characterisation:** the scientific methodology was determined to approach the main tasks of the project. Firstly, the model of the blade dynamics was built analytically. Secondly, a suitable material for the friction damping system was researched. The order of the tasks was not relevant yet at this phase.

iv. **Code preparation and post-processing:** at this stage the equations of the model were written in MATLAB. After optimising the maths and solving the issues, especially the ones related to the coding language and the Symbolic Math Toolbox™, the code was executed and the graphs were checked and standardised in terms of format.

v. **Results collection and processing:** yet as a draft, the raw results obtained were processed organising the files. At a second glance, they were evaluated and discussed, selecting the most suitable material for the friction disc and evaluating the performance according to the numerical simulation results. Further comparison with experimental results allowed the validation of the model and the material choice.

vi. **Document preparation:** first of all, a template was designed by formatting in LaTeX language. Afterwards, the draft notes previously written in a text file were transferred to the new formal template. The corresponding figures, tables and charts were included and the whole document was revised for corrections as a final duty.

vii. **Tutorial meetings and planning:** along the semester, the coordination with AJCC, who set the requirements, was established telematically. In parallel, the planning with the project supervisor was based on meetings at the department in the university and contact via email. The preparation of the agenda and documentation prior to the meetings are included in this point as well as the minutes to keep track of the full schedule. The total time spent on the project is recorded in table 6.1 below and its distribution along the semester is arranged in a Gantt chart in fig. D.1, appendix A.

Task	**Time [h]**
Background & problem definition	15
Documentation collection & research	25
Model characterisation	100
Code preparation & post-processing	135
Results collection & processing	20
Document preparation	140
Tutorial meetings & planning	15
Total	**450**

Table 6.1: Time invested in the project.

6.2 Budget

The budget of the project is calculated according to an estimation of all cost categories. That involves working time, software licenses, equipment and any assets used in the process. Additionally, the cost of the selected material and the manufacturing of such are also included.

6.2.1 Labour

An average salary of 15 €/h is estimated for both a Bacehlor's Degree student developing the project and a technician manufacturing the pieces. The latter is assumed to spend a working day (about 9 h) processing all the units (casting and turning operations mainly).

Personnel	**Cost [€/h]**	**Time [h]**	**Total Cost [€]**
Student	15	450	6750
Manufacturer	15	9	135
Total			**6825**

Table 6.2: Cost of labour.

6.2.2 Equipment

The main equipment needed to develop the project is a computer, where the research process, all analytic and numerical calculations and the document preparation have been developed. An useful life estimated as 10 years has been used to calculate a linear depreciation.

$$Depreciation = \frac{Investment}{Lifespan} \tag{6.1}$$

Likewise, the final cost takes into account the period of time that the project lasts for: half a year.

$$Cost = Depreciation \times Time\ Period \tag{6.2}$$

Item	**Investment [€]**	**Lifespan [years]**	**Depreciation [€/year]**	**Cost [€]**
Computer	1200	10	120	60
Total				**60**

Table 6.3: Cost of equipment.

6.2.3 Software

For the case of MATLAB, the student suite license (for use in Spain) is retrieved from MathWorks. In contrast, zero cost is assumed for XFLR5 since it is an open source (copyleft) programme and a GNU General Public License was used.

Software	**Cost [€]**
MATLAB (student suite)	69
XFLR5	0
Total	**69**

Table 6.4: Cost of software.

6.2.4 Product Material

Regardless of the manufacturing labour cost, assuming that the first material[1] in the ranking is finally selected and taking only the cylindrical volume of the friction disc as reference:

$$V_{ref} = \pi R_o^2 \cdot t = \frac{\pi}{4} D_o^2 \cdot t \tag{6.3}$$

So for a thickness of 5 mm, an outer diameter of 140 mm and applying an uncertainty factor of 50% to account for material loss in the manufacturing process, the reference volume of the friction disc is directly obtained.

$$V_{ref} = 1.15 \cdot 10^{-4}\ m^3$$

Remember that each damper has two friction discs and the gyroplane has three blades, which makes a total of six units. Together with the raw material[1] cost per unit mass and density ($1,96$€[2] and 2680 kg/m^3, respectively), the total cost is calculated.

$$Cost = C \cdot \rho \cdot 6V_{ref} \tag{6.4}$$

$$Cost = \$4,25 = 3,62€ \approx 4€$$

[1] Cast Aluminium Alloy 356.0 according to table 3.4.

[2] Price converted from US dollars at an exchange rate of $0,85$ €/\$. Original price: $\$2,30$.

Material	Cost [€]
Cast Aluminium Alloy 356.0	4
Total	**4**

Table 6.5: Cost of raw material.

As a relevant remark, no minimum orders are considered when buying the raw material. That totally depends on the provider chosen and the deal made with them. Notwithstanding, it is important to consider that large purchasing amounts (compared to the mass needed) usually of the order of metric tons, are often established by sellers as minimum, which may potentially increase the cost.

6.2.5 Total

Adding finally all the categories, the total cost is estimated at approximately 7000€ —rounding off to the nearest hundred—.

Category	Cost [€]
Labour	6885
Equipment	60
Software	69
Material	4
Total	**7018**

Table 6.6: Total cost.

Therefore the budget required should be at least this value, excluding any conditions imposed by sellers within the metallurgical sector like minimum purchase amounts of material.

Bibliography

[1] F. Altpeter. *Friction modeling, identification and compensation.* PhD thesis, École Polytechnique Fédérale de Lausanne, Lausanne, Switzerland, 1999.

[2] R. Brie. *The Autogiro and how to fly it.* Pitman, second edition, July 1934.

[3] C. L. Bullock. *Rota aeroplane*, volume I. Air Ministry, December 1934.

[4] C. L. Bullock. *Rota aeroplane*, volume II. Air Ministry, January 1936.

[5] J. R. Davis. *Alloying: understanding the basics.* ASM International, first edition, January 2001.

[6] A. R. S. Bramwell et al. *Bramwell's helicopter dynamics.* Elsevier, Oxford, United Kingdom, second edition, 2001.

[7] B. Dehghan-Manshadi et al. *A novel method for materials selection in mechanical design: combination of non-linear normalization and a modified digital logic method.* ScienceDirect, June 2005.

[8] D. R. Herling et al. *Low-cost Aluminum metal matrix composites.* Advanced Materials & Process, July 2001.

[9] E. L. Houghton et al. *Aerodynamics for engineering students.* Elsevier, Oxford, United Kingdom, sixth edition, 2013.

[10] O. A. Bauchau et al. *Semiactive Coulomb friction lead–lag dampers.* Technical Report No 012005, Daniel Guggenheim School of Aerospace Engineering, Georgia Institute of Technology, Atlanta, Georgia, USA, 2010.

[11] O. Maluf et al. *Development of materials for automotive disc brakes.* Technical Report pp.149(10):158, Minerva, University of São Paulo, São Carlos, São Paulo, Brazil, January 2004.

[12] P. A. Hufton et al. *General investigation into the characteristics of the C.30 Autogyro.* Reports and Memoranda 1859, March 1939.

[13] M. M. Farag. *Materials and process selection for engineering design.* CRC Press, third edition, March 2013.

[14] D. Gibbings. *The evolution of the British rotorcraft industry 1842-2012.* Journal of Aeronautical History, (No 2012/07), July 2012.

[15] J. Gordon Leishman. *Principles of helicopter aerodynamics.* Cambridge University Press, Cambridge, United Kingdom, 2000.

[16] S. Mackertich. *Dynamic modeling of autorotation for simultaneous lift and wind energy extraction.* Master's thesis, College of Engineering and Computer Science, University of Central Florida, Orlando, Florida, USA, Spring 2012.

[17] Maestranza Aérea de Albacete (MAESAL), Albacete, Castilla-La Mancha, Spain. *Autogiro C30 MZA. Manual de uso y mantenimiento*, December 1998.

[18] J. R. Majhi and R. Ganguli. *Modeling helicopter rotor blade flapping motion considering nonlinear aerodynamics.* Technical Report No 1, Computer Modeling in Engineering and Sciences (CMES), 2008.

[19] M. A. Maleque. *Material selection method in design of automotive brake disc.* World Congress on Engineering (WCE), III, July 2010.

[20] J. L. López Ruiz. *Autogiro C.30 MZA. Resonancia en tierra.* Reports and memoranda, Madrid, August 2000.

[21] G. Townson. *Autogiro. The story of the windmill plane.* Aviation Heritage, second edition, 1985.

[22] A. Roldán Villén. *Juan de la Cierva y Codorníu. Conde de la Cierva.* Real Academia de la Historia. Biography.

[23] Dr. M. Vural. *Estimating R/C model aerodynamics and performance.* Summer 2009. Illinois Institute of Technology, Illinois, USA.

[24] J. B. Wheatley. *An aerodynamic analysis of the autogiro rotor with a comparison between calculated and experimental results.* Technical Report 487, National Advisory Committee for Aeronautics, Langley Memorial Aeronautical Laboratory, Fairfax, Virginia, January 1934.

[25] Sevinç Çalişkan. *Development of forward flight trim and longitudinal dynamic stability codes and their application to a UH-60 helicopter.* Master's thesis, Middle East Technical University, Ankara, Turkey, February 2009.

Legislation References

[L1] Gobierno de España. *Real Decreto 660/2001, de 22 de Junio, por el que se regula la certificación de las aeronaves civiles y de los productos y piezas relacionados con ellas.* No 165, pp.25148(55):25202. BOE-A-2001-13367. July 2001.

[L2] European Parliament and Council. *Regulation (EC) No 216/2008 of 20 February 2008 on common rules in the field of civil aviation and establishing a European Aviation Safety Agency, and repealing Council Directive 91/670/EEC, Regulation (EC) No 1592/2002 and Directive 2004/36/EC.* Official Journal of the European Union, March 2008.

Web Sources

[W1] Airfoil Tools. Airfoils database and plotter online. `http://airfoiltools.com`. Accessed: 15-05-2018.

[W2] Avia Deja Vu. `http://aviadejavu.ru/Site/Crafts/Craft21898.htm`. Picture. Accessed: 03-04-2018.

[W3] Cierva C.30 Autogyro - Avro 671 Rota. `https://www.the-blueprints.com/blueprints/helicopters/helicopters-c-g/53893/view/cierva_c_30_autogyro__avro_671_rota/`. Picture. Accessed: 02-04-2018.

[W4] Stackexchange. `https://i.stack.imgur.com/32039.jpg`. Picture. Accessed: 11-04-2018.

[W5] Substances & Technologies. Material properties database. `http://www.substech.com/dokuwiki/doku.php?id=materials_data`. Accessed: 10-07-2018.

[W6] Shamail Ahmad. *Presence of golden ratio relationships in Fe–Fe3C, Cu–Zn and Cu–Sn alloy systems.* Philipps University of Marburg. `https://www.researchgate.net/profile/Shamail_Ahmad/publication/281806061/figure/fig1/AS:522846623498240@1501667757641/Iron-iron-carbide-phase-diagram-6-7.jpg`. Picture. Accessed: 19-07-2018.

[W7] AZoM. Material properties database. online publication for the materials Science community. https://www.azom.com. Accessed: 10-07-2018.

[W8] D. Cameron and Douglas Thomson. Scottish contributions to rotary wing flight. American Helicopter Society (AHS), March 2009. http://eprints.gla.ac.uk/4973/1/4973.pdf. Accessed: 03-04-2018.

[W9] MATLAB. Computation software. Trapezoidal numerical integration. https://uk.mathworks.com/help/matlab/ref/trapz.html, 2018. Accessed: 15-06-2018.

[W10] Corrosionpedia. Educational content on corrosion. https://www.corrosionpedia.com/definition/563/galling. Accessed: 12-04-2018.

[W11] Filipe Szolnoky Cunha. Helicopters. Instituto Superior Técnico, Lisbon. https://fenix.tecnico.ulisboa.pt/downloadFile/282093452028195/7-Blade%20element%20theory.pdf. Lecture slides. Accessed: 08-04-2018.

[W12] Ecardmodels. 1/48 cierva c.30/avro rota autogyro multi-kit models. https://www.ecardmodels.com/index.php/1-48-cierva-c-30-avro-rota-autogyro-multi-kit-paper-model.html. Picture. Accessed: 02-04-2018.

[W13] Engineers Edge. Disk brake design equations. https://www.engineersedge.com/mechanics_machines/disk-brake-calculations.htm. Picture. Accessed: 06-07-2018.

[W14] C. Gablehouse. Helicopters and autogiros. http://www.aviastar.org/theory/rotor.html, 1969. Accessed: 11-04-2018.

[W15] Helicopters and Aircraft. Axial flight: blade element theory. http://heli-air.net/2016/02/27/axial-flight-blade-element-theory, February 2016. Picture. Accessed: 21-05-2018.

[W16] J. Lewis. Autogyro history and theory. http://www.jefflewis.net/autogyros.html. Accessed: 02-04-2018.

[W17] MakeItFrom. Material properties database. https://www.makeitfrom.com/. Accessed: 10-07-2018.

[W18] Alejandro Polanco Masa. *El autogiro de Juan de la Cierva. Tecnología Obsoleta*, July 2014. https://alpoma.net/tecob/?p=9161. Accessed: 02-04-2018.

[W19] Metline Industries. Distributor of aluminium and steel. https://www.steelplates.in/. Online catalogue. Accessed: 11-07-2018.

[W20] D. E. Lerner. University of Kansas. Lecture Notes on Linear Algebra. http://www.math.ku.edu/~lerner/LAnotes/LAnotes.pdf, 2007. Lecture notes. Accessed: 01-05-2018.

[W21] Massachusetts Institute of Technology (MIT). Modules in mechanics of materials. http://web.mit.edu/course/3/3.11/www/modules/props.pdf, 1996. Accessed: 05-07-2018.

[W22] Jorge D. Ortalli. *Mecánica III: rotores*. Departamento de Aeronáutica, Facultad de Ingeniería, Universidad Nacional de La Plata, La Plata, Buenos Aires, Argentina, August 2002. Lecture Notes. http://www.aero.ing.unlp.edu.ar/catedras/archivos/APUNTE%20TIPO%20DE%20ROTORES.pdf. Accessed: 13-04-2018.

[W23] Pegasus Spiele. https://www.pegasus.de/fileadmin/Downloads/Spiele/Buecher/Cthulhu/BdW-Fahrzeug-CiervaC30.jpg. Picture. Accessed: 02-04-2018.

[W24] Engineering ToolBox. Friction and Friction Coefficients. https://www.engineeringtoolbox.com/friction-coefficients-d_778.html, 2004. Accessed: 10-05-2018.

[W25] T.R.S. Ductile Cast Iron. http://www.leevalley.com/en/shopping/techinfo.aspx?c=&type=a&p=49540. Picture. Accessed: 21-07-2018.

Appendices

A Illustrations Appendix

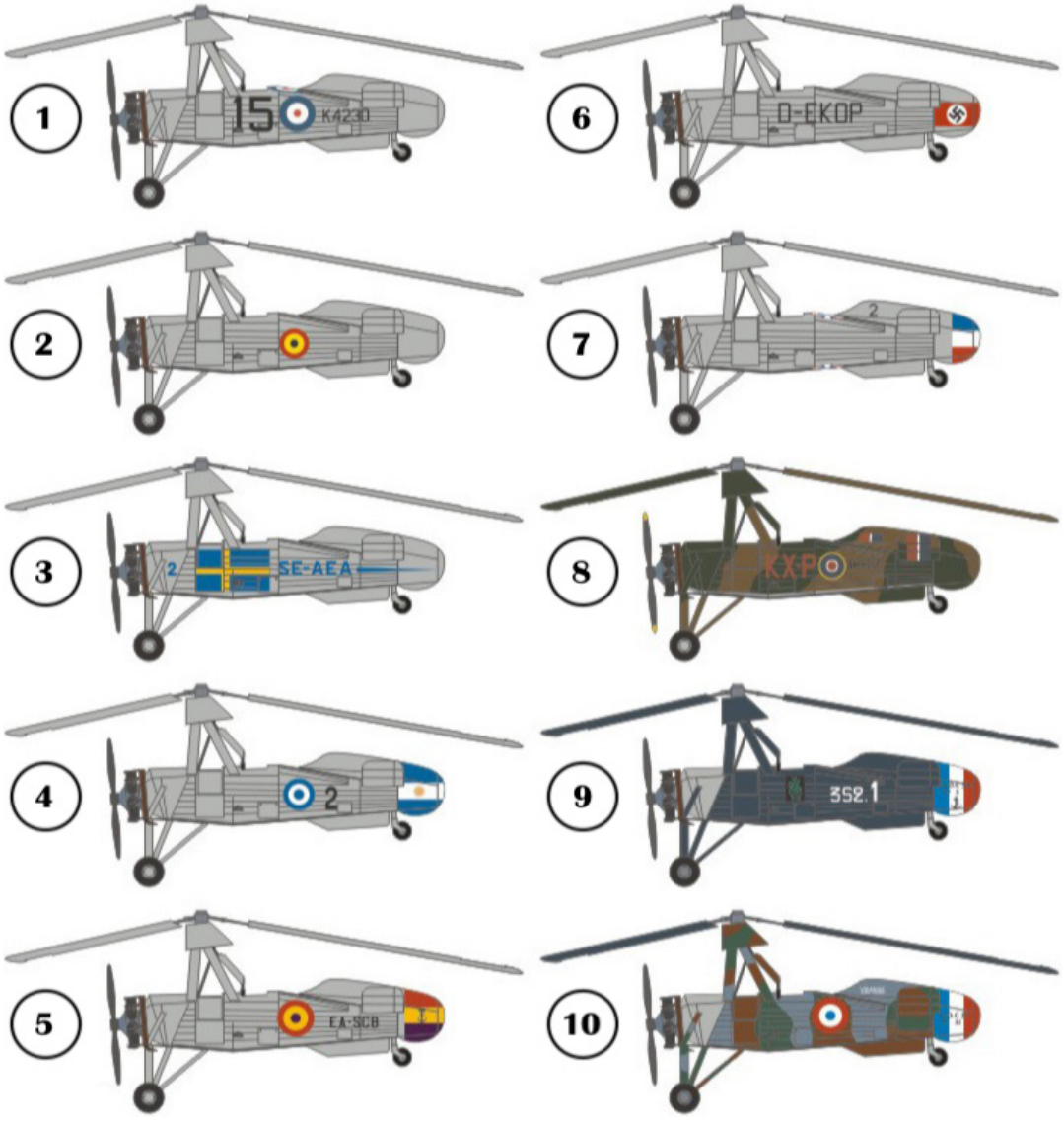

Figure A.1: Ten military units of the Avro Rota Cierva C.30 acquired by international military forces [W12].

1.UK Royal Air Force used to test landings on aircraft carriers. **2.**Belgian Air Force. **3.**Sweden, built by AB Autogiro, performed charter flights, rescue and ambulance and became popular in winter sport stations. **4.**Argentine Air Force. **5.**Spanish Naval Aviation (1934 to July 1936). **6.**German forces. **7.**Yugoslavian Air Force (1939). **8.**UK Royal Air Force used for radar calibration flights (1943). **9.**French Navy assigned to l'Escadrille 3S2 (1939). **10.**French Air Force assigned in Reims, Champagne (1940).

B Material Research Appendix

Material	**Type/Grade/Class**		**Properties**					
			Density $[\frac{kg}{m^3}]$	Specific Heat $[\frac{J}{kg \cdot K}]$	Thermal Conduct. $[\frac{W}{m \cdot K}]$	Compressive Strength $[MPa]$	Tensile Strength $[MPa]$	Friction Coeff. $[-]$
Ceramic Composite	C-Matrix	C-Fibres	1700	1338	11	210	20	0.40-0.52
	SiC-Matrix	SiC-Fibres	2100	630	15	200	34	0.40-0.52
	Al-Matrix	SiC-Fibres	2820	690	25	150	15	0.40-0.52
Titanium	Alloy	Ti-6Al-4V	4430	565	7	1085	40	0.38-0.41
Aluminium	Alloy	333.0	2770	963	105	240	119	0.47-0.61
		356.0	2680	963	167	240	91	0.47-0.61
		514.0	2650	963	138	170	140	0.47-0.61
		518.0	2570	963	96	310	205	0.47-0.61
		705.0	2760	963	105	240	127	0.47-0.61
		713.0	2810	963	121	235	180	0.47-0.61
		852.0	2880	963	172	185	115	0.47-0.61
Steel	Alloy	SAE 4027	7872	477	45	640	320	0.10-0.60
		SAE 5140	7872	452	45	795	490	0.10-0.60
		SAE 9255	7872	477	52	635	550	0.10-0.60
	Carbon	SAE 1006	7872	481	65	300	250	0.10-0.60
		SAE 1045	7872	486	51	590	480	0.10-0.60
		SAE 1547	7872	473	51	680	580	0.10-0.60
	Stainless	AISI 201	7800	500	16	910	520	0.10-0.60
		AISI 410	7700	460	25	680	420	0.10-0.60
		AISI 2205	7800	460	19	750	470	0.10-0.60
Cast Iron	Grey	ASTM A48 CLASS 40	7200	490	54	275	400	0.25-0.40
	Ductile	ASTM A536	6920	506	32	495	372	0.25-0.40

Table B.1: Candidate materials, properties [5][W5, W7, W24, W21].

Material	**Type/Grade/Class**		**Scaled Properties (β_i)**						**Cost**	**IoP**	**FoM**	**Ranking**
			Density	Specific Heat	Thermal Conduct.	Compress. Strength	Tensile Strength	Friction Coeff.	$[\frac{\$}{kg}]$	[%]		
Composite	C-Matrix	C-Fibres	1.000	1.000	0.066	0.104	0.194	0.852	4000,00	53.7	0.1	21
	SiC-Matrix	SiC-Fibres	0.810	0.471	0.090	0.469	0.184	0.852	3600,00	42.7	0.1	22
	Al-Matrix	SiC-Fibres	0.603	0.516	0.150	0.281	0.138	0.852	1600,00	54.6	0.1	20
Titanium	Alloy	Ti-6Al-4V	0.384	0.422	0.042	1.000	1.000	0.731	65,00	38.8	1.3	19
Aluminium	Alloy	333.0	0.614	0.720	0.629	0.156	0.221	1.000	2,10	56.0	96.3	3
		356.0	0.634	0.720	1.000	0.177	0.221	1.000	2,30	64.1	104.0	1
		514.0	0.642	0.720	0.826	0.089	0.157	1.000	2,50	60.4	91.2	4
		518.0	0.661	0.720	0.575	0.146	0.286	1.000	2,60	57.6	86.2	5
		705.0	0.616	0.720	0.629	0.130	0.221	1.000	3,50	55.9	57.9	7
		713.0	0.605	0.720	0.725	0.182	0.217	1.000	3,80	59.7	55.9	8
		852.0	0.590	0.720	1.000	0.193	0.106	1.000	4,30	62.8	50.7	2
Steel	Alloy	SAE 4027	0.216	0.357	0.269	0.146	0.590	0.648	0,70	33.4	60.6	6
		SAE 5140	0.216	0.338	0.269	0.156	0.733	0.648	0,90	37.0	52.2	10
		SAE 9255	0.216	0.357	0.311	0.156	0.585	0.648	1,10	39.7	45.9	12
	Carbon	SAE 1006	0.216	0.359	0.389	0.188	0.276	0.648	1,30	35.0	34.2	16
		SAE 1045	0.216	0.363	0.305	0.198	0.544	0.648	1,30	38.7	37.8	15
		SAE 1547	0.216	0.354	0.305	0.219	0.627	0.648	0,90	41.1	58.0	9
	Stainless	AISI 201	0.218	0.374	0.096	0.380	0.839	0.648	1,10	37.8	44.1	11
		AISI 410	0.221	0.344	0.150	0.432	0.627	0.648	2,40	36.7	19.9	17
		AISI 2205	0.218	0.344	0.114	0.438	0.691	0.648	3,00	37.1	15.9	18
Cast Iron	Grey	ASTM A48 CLASS 40	0.236	0.366	0.323	0.861	0.253	0.602	1,40	46.2	45.8	13
	Ductile	ASTM A536	0.246	0.378	0.192	0.542	0.456	0.602	1,50	38.9	37.5	14

Table B.2: Scaled properties of candidate materials & ranking [8][W21, W19].

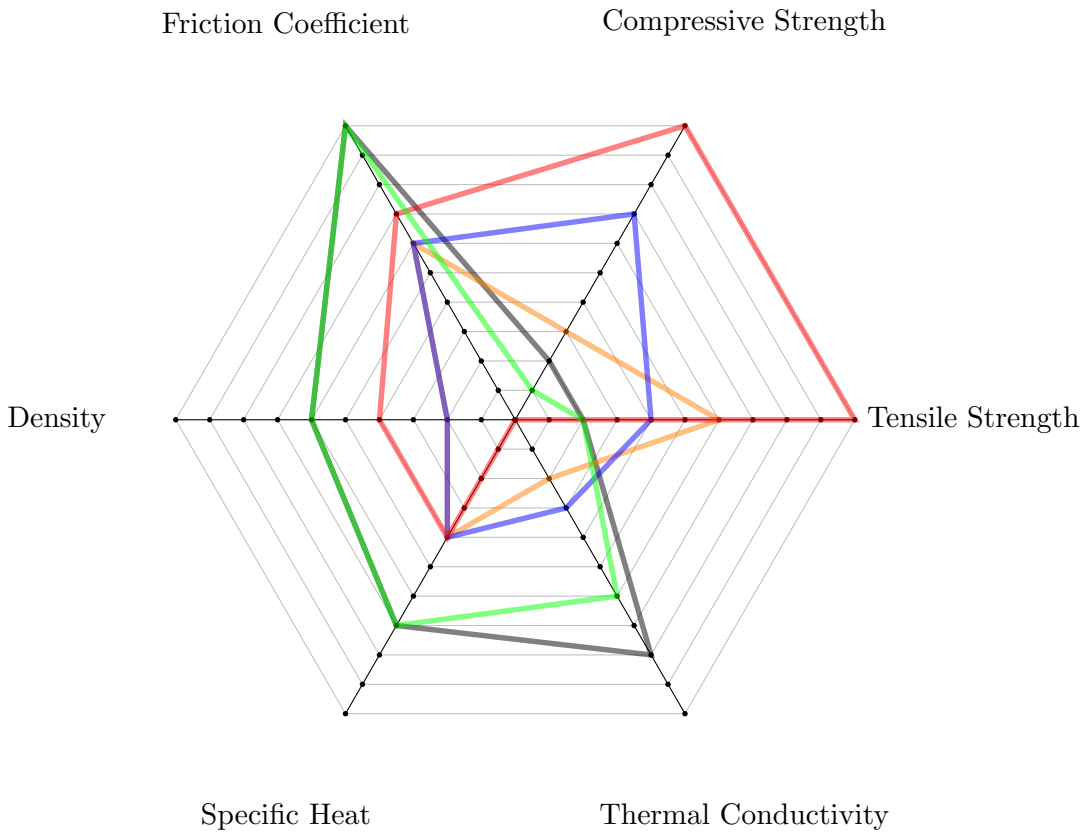

Figure B.1: Average scaled properties (β) of aluminium (black), steel (orange), cast iron (blue), titanium (red) & ceramic composite (green).

B.1 Disc brake torque derivation

$$M_f = 4\int_A dM = 4\int_A \mu P r dA = 4\mu \int_A \frac{F_{comp}}{A_c} r dA = 4\mu F_{comp} \iint_{R_i,\theta_1}^{R_o,\theta_2} \frac{r\,(r dr d\theta)}{\iint_{R_i,\theta_1=0}^{R_o,\theta_2=2\pi} d\theta r dr} =$$
$$= 4\frac{\mu F_{comp}}{\pi\left(R_o^2 - R_i^2\right)} \iint_{R_i,\theta_1}^{R_o,\theta_2} r^2 dr d\theta = 4\frac{\mu F_{comp}}{\pi\left(R_o^2 - R_i^2\right)} 2\pi \int_{R_i}^{R_o} r^2 dr = 8\frac{\mu F_{comp}}{R_o^2 - R_i^2} \int_{R_i}^{R_o} r^2 dr =$$
$$= 8\frac{\mu F_{comp}}{R_o^2 - R_i^2} \frac{R_o^3 - R_i^3}{3} = \frac{8}{3}\frac{R_o^3 - R_i^3}{R_o^2 - R_i^2} \mu F_{comp} \tag{B.1}$$

C Simulation Model Appendix

C.1 Transformation matrices

$$\bar{\bar{T}}_{E\to B} = \begin{bmatrix} \cos(\Psi)\cos(\Theta) & \cos(\Psi)\sin(\Phi)\sin(\Theta) - \cos(\Phi)\sin(\Psi) & -\sin(\Phi)\sin(\Psi) - \cos(\Phi)\cos(\Psi)\sin(\Theta) \\ -\cos(\Theta)\sin(\Psi) & -\cos(\Phi)\cos(\Psi) - \sin(\Phi)\sin(\Psi)\sin(\Theta) & \cos(\Phi)\sin(\Psi)\sin(\Theta) - \cos(\Psi)\sin(\Phi) \\ -\sin(\Theta) & \cos(\Theta)\sin(\Phi) & -\cos(\Phi)\cos(\Theta) \end{bmatrix} \tag{C.1}$$

$$\bar{\bar{T}}_{A\to B} = \begin{bmatrix} -\cos(\alpha)\cos(\beta_s) & \sin(\beta_s) & -\cos(\beta_s)\sin(\alpha) \\ \cos(\alpha)\sin(\beta_s) & \cos(\beta_s) & \sin(\alpha)\sin(\beta_s) \\ -\sin(\alpha) & 0 & \cos(\alpha) \end{bmatrix} \tag{C.2}$$

$$\bar{\bar{T}}_{B\to R} = \begin{bmatrix} 1 & 0 & 0 \\ 0 & -1 & 0 \\ 0 & 0 & -1 \end{bmatrix} \tag{C.3}$$

$$\bar{\bar{T}}_{R\to 1} = \begin{bmatrix} \cos(\Omega t) & \sin(\Omega t) & 0 \\ -\sin(\Omega t) & \cos(\Omega t) & 0 \\ 0 & 0 & 1 \end{bmatrix} \tag{C.4}$$

$$\bar{\bar{T}}_{1\to 2} = \begin{bmatrix} \cos(\xi) & \sin(\xi) & 0 \\ -\sin(\xi) & \cos(\xi) & 0 \\ 0 & 0 & 1 \end{bmatrix} \tag{C.5}$$

$$\bar{\bar{T}}_{2\to 3} = \begin{bmatrix} \cos(\beta) & 0 & \sin(\beta) \\ 0 & 1 & 0 \\ -\sin(\beta) & 0 & \cos(\beta) \end{bmatrix} \tag{C.6}$$

$$\bar{\bar{T}}_{3\to 4} = \begin{bmatrix} 1 & 0 & 0 \\ 0 & \cos(\theta) & \sin(\theta) \\ 0 & -\sin(\theta) & \cos(\theta) \end{bmatrix} \tag{C.7}$$

$$\bar{\bar{T}}_{4\to 5} = \begin{bmatrix} 1 & 0 & 0 \\ 0 & \cos(\alpha_b) & \sin(\alpha_b) \\ 0 & -\sin(\alpha_b) & \cos(\alpha_b) \end{bmatrix} \tag{C.8}$$

C.2 Model of aerodynamics

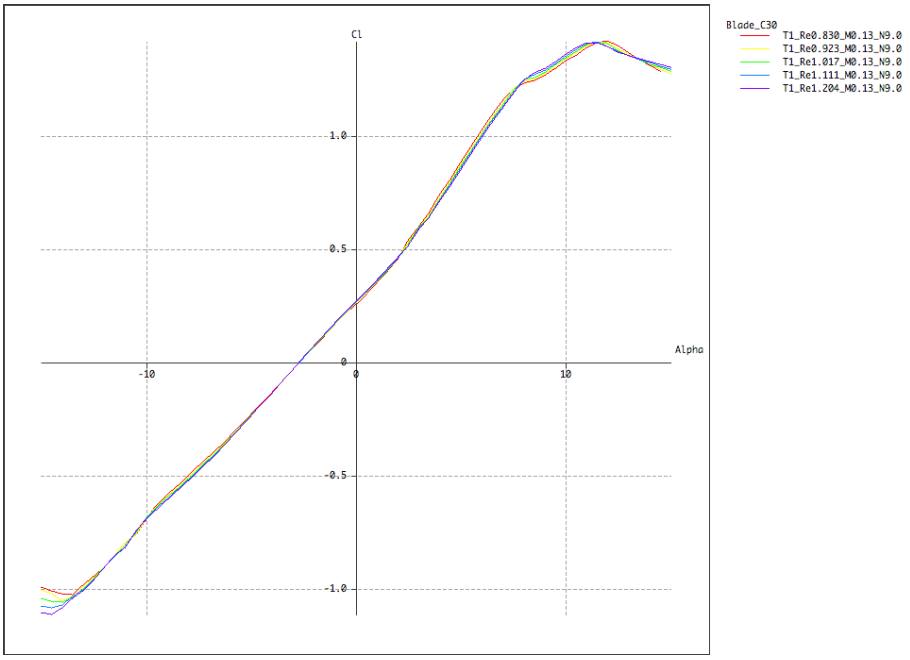

(a) Lift coefficient VS angle of attack.

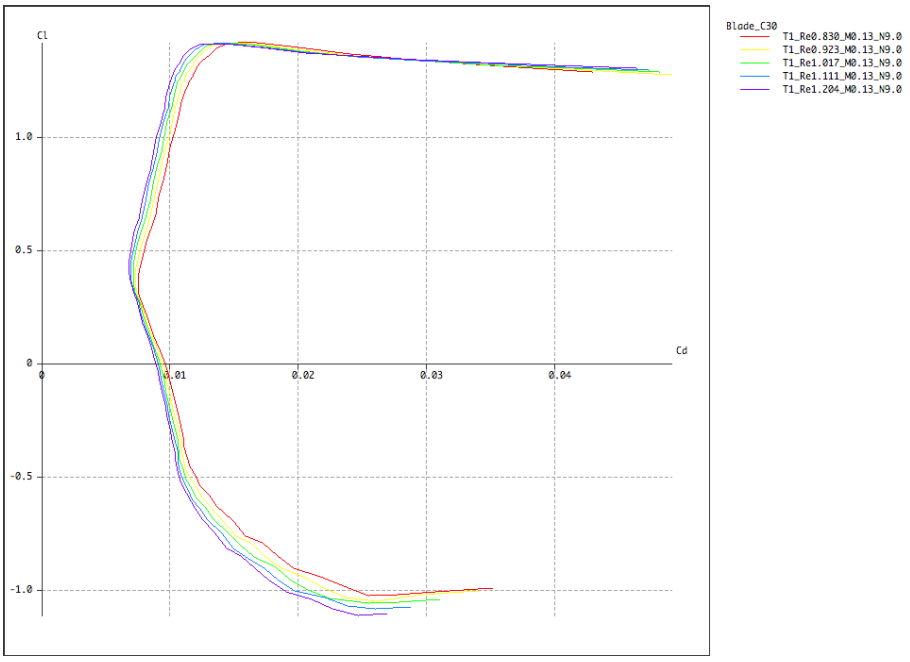

(b) Lift coefficient VS drag coefficient.

Figure C.1: NACA 3316 polars at 5 equally spaced blade sections from root to tip.

C.3 Blade motions

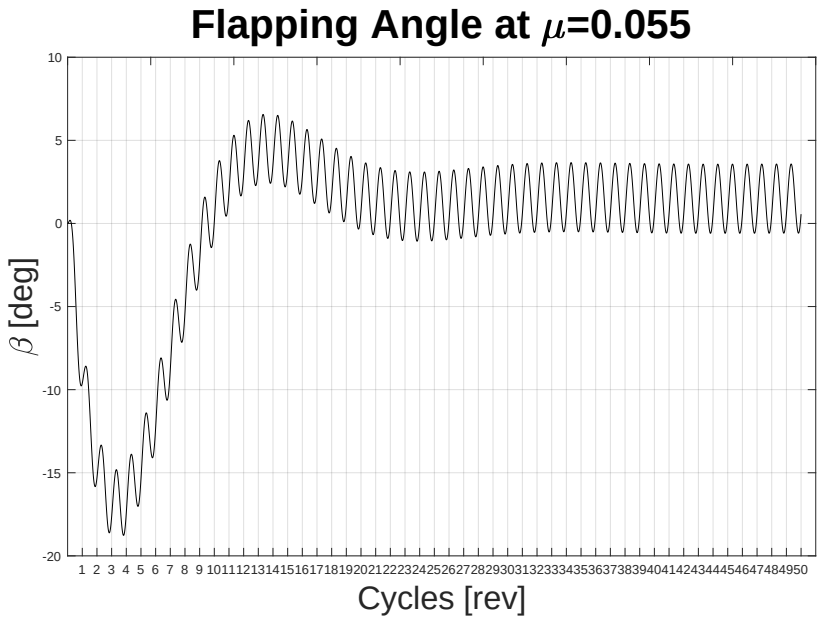

Figure C.2: Flapping angle at $\mu = 0.055$.

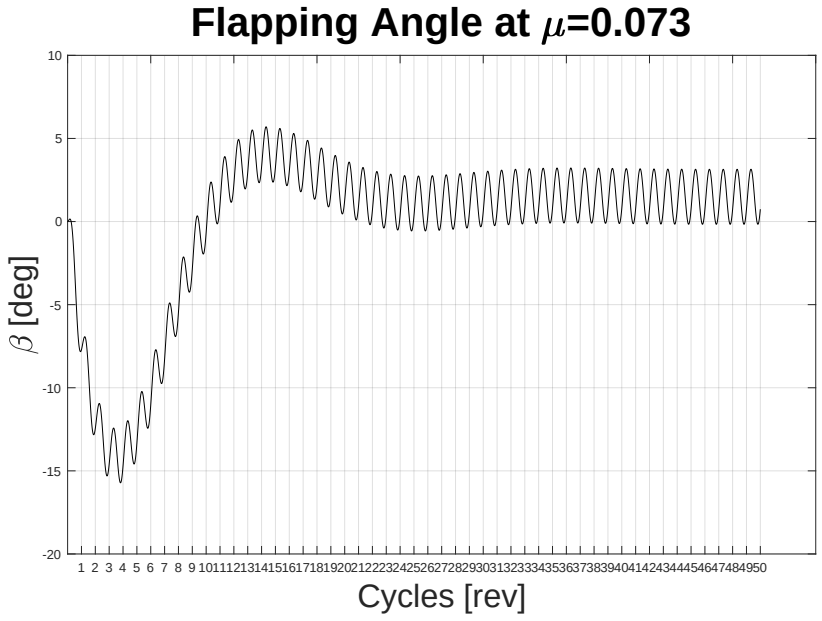

Figure C.3: Flapping angle at $\mu = 0.073$.

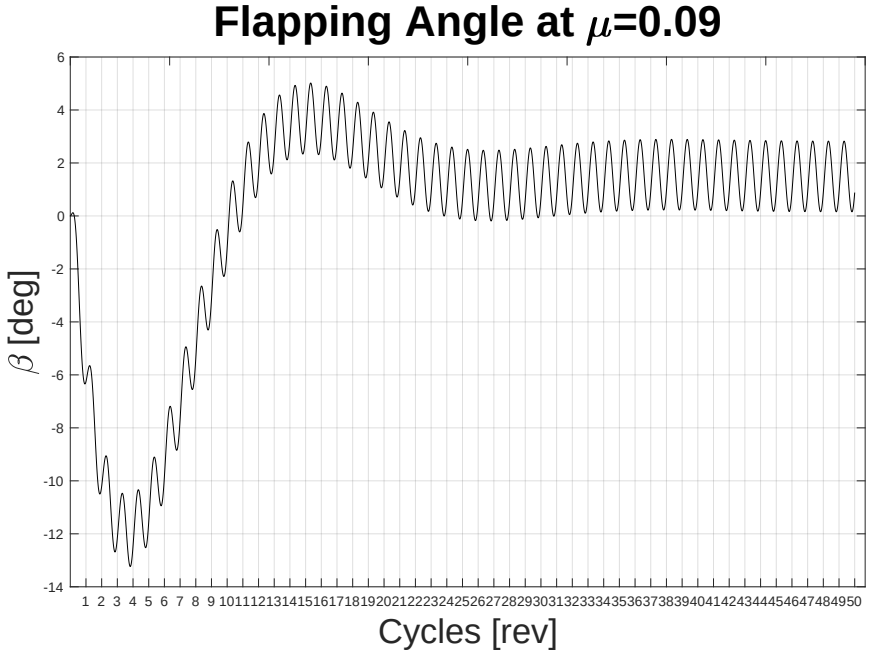

Figure C.4: Flapping angle at $\mu = 0.090$.

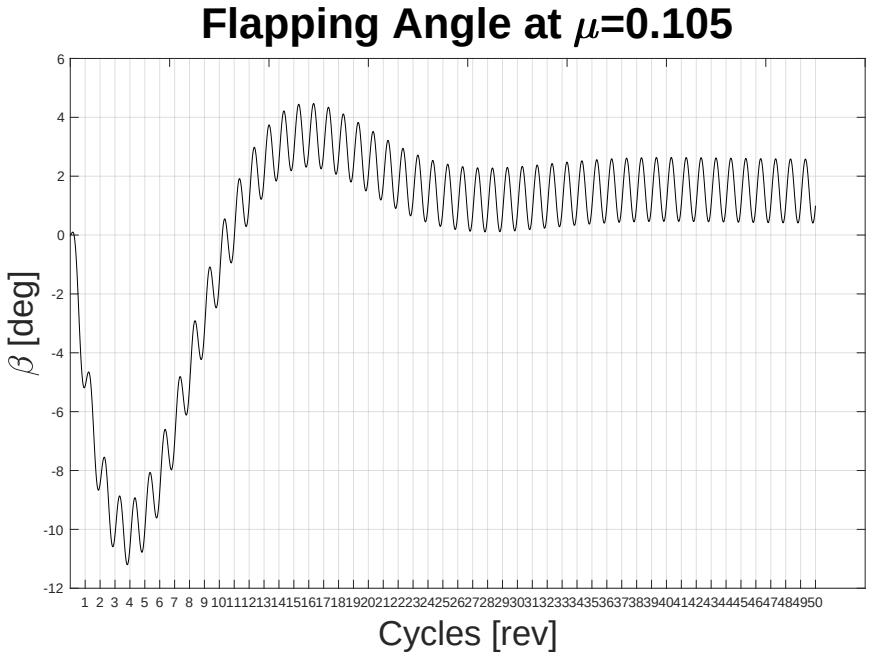

Figure C.5: Flapping angle at $\mu = 0.105$.

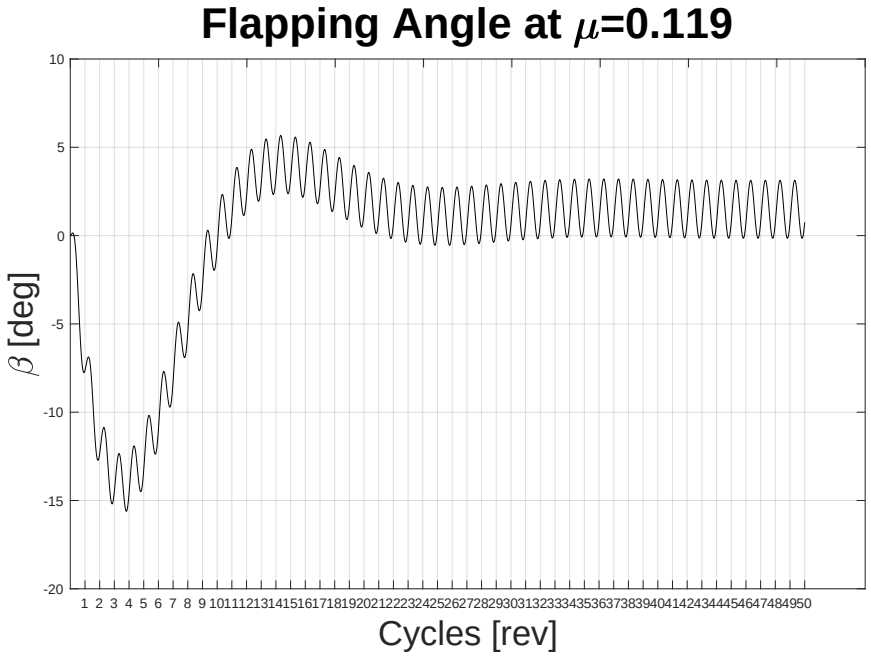

Figure C.6: Flapping angle at $\mu = 0.119$.

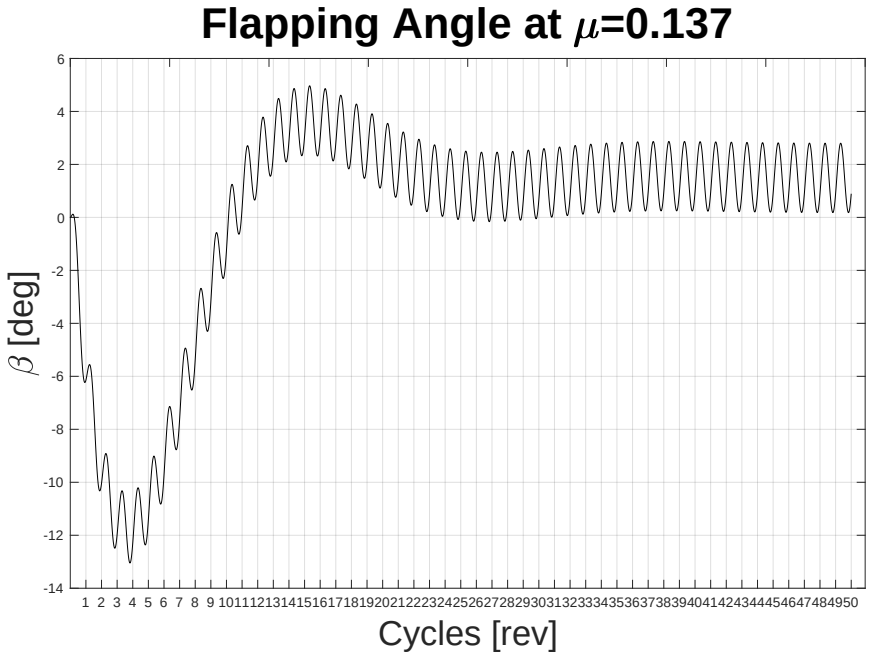

Figure C.7: Flapping angle at $\mu = 0.137$.

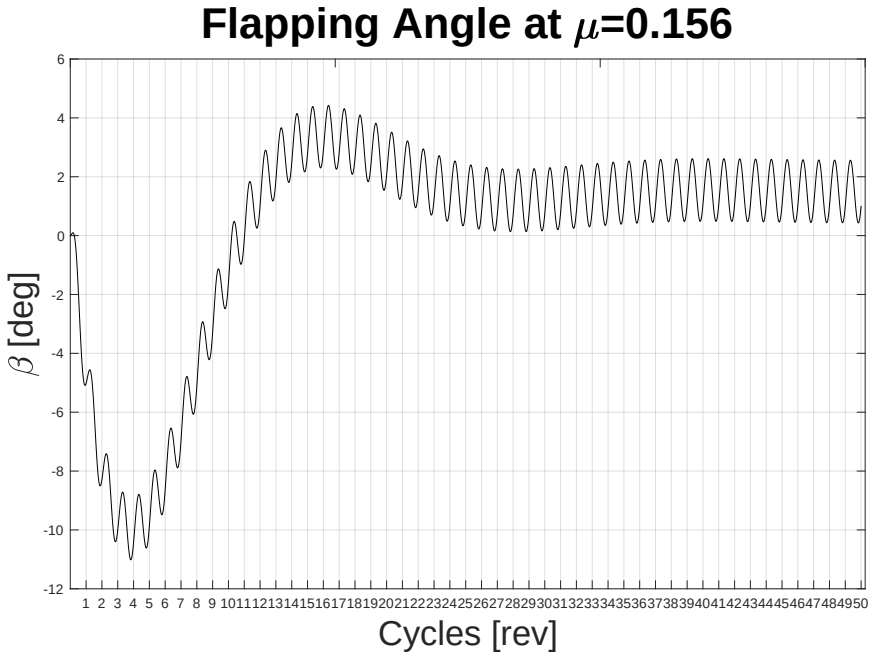

Figure C.8: Flapping angle at $\mu = 0.156$.

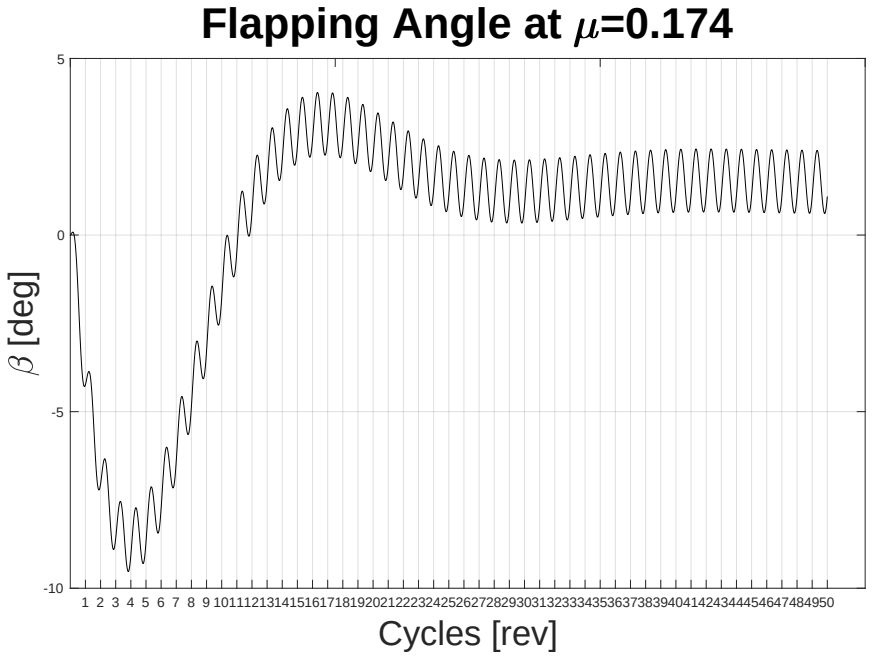

Figure C.9: Flapping angle at $\mu = 0.174$.

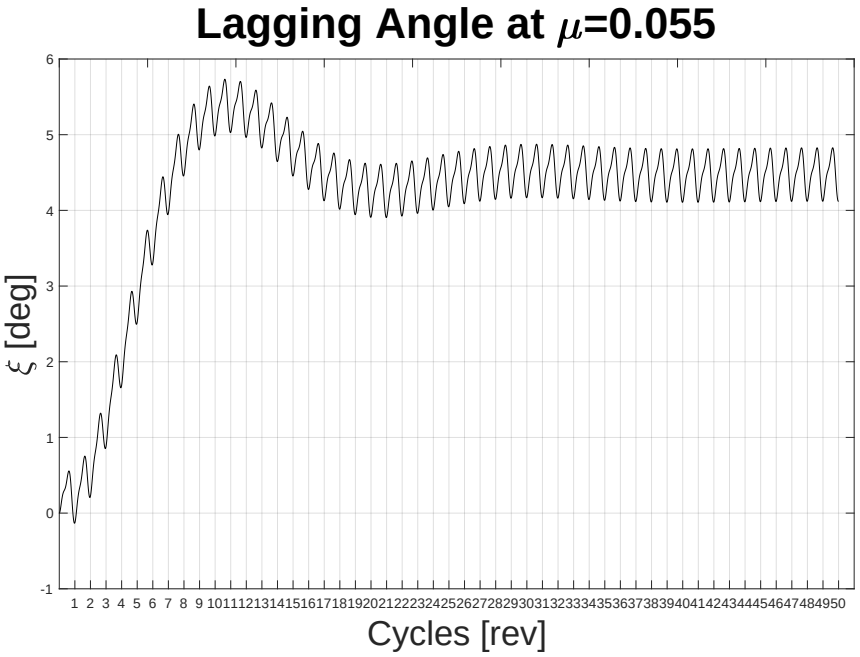

Figure C.10: Lagging angle at $\mu = 0.055$.

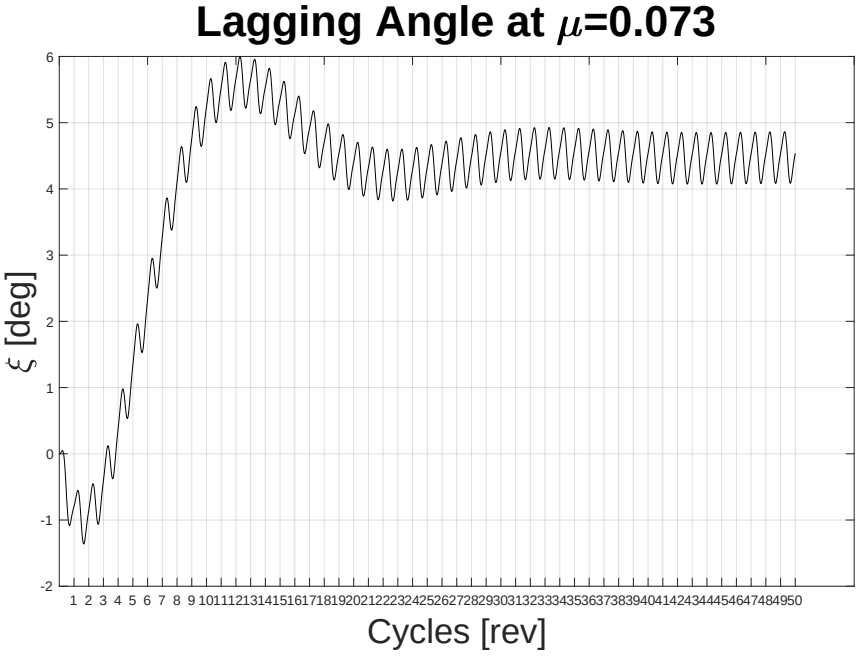

Figure C.11: Lagging angle at $\mu = 0.073$.

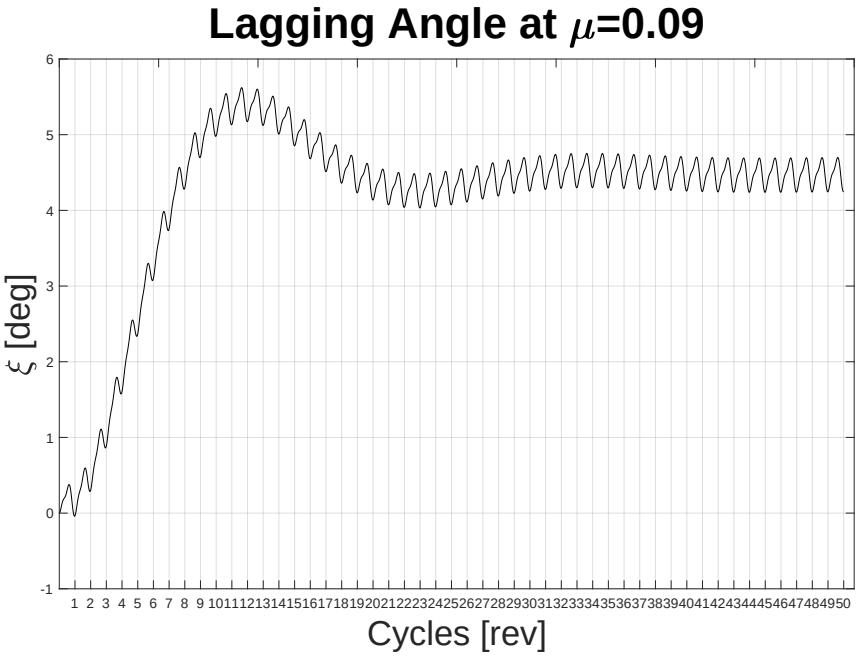

Figure C.12: Lagging angle at $\mu = 0.090$.

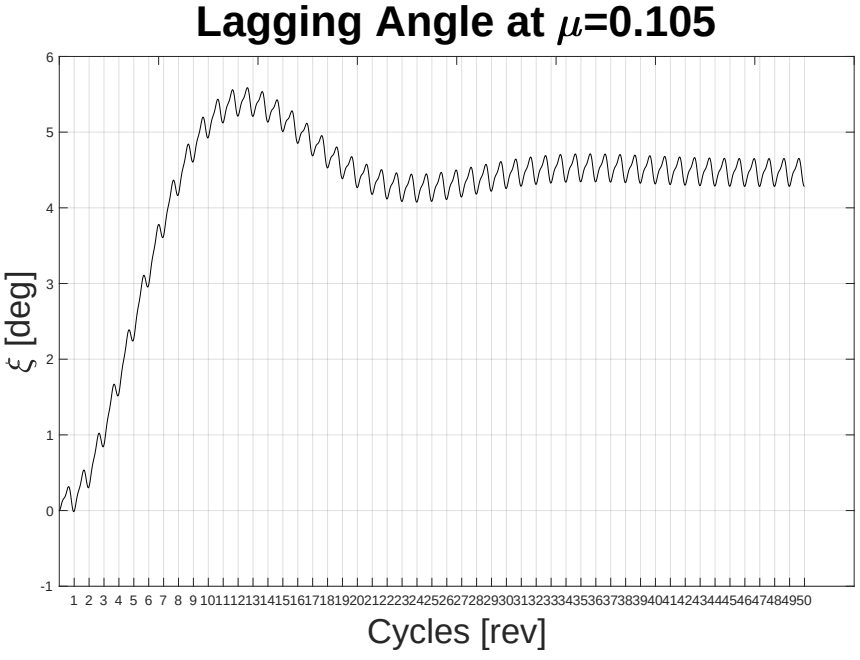

Figure C.13: Lagging angle at $\mu = 0.105$.

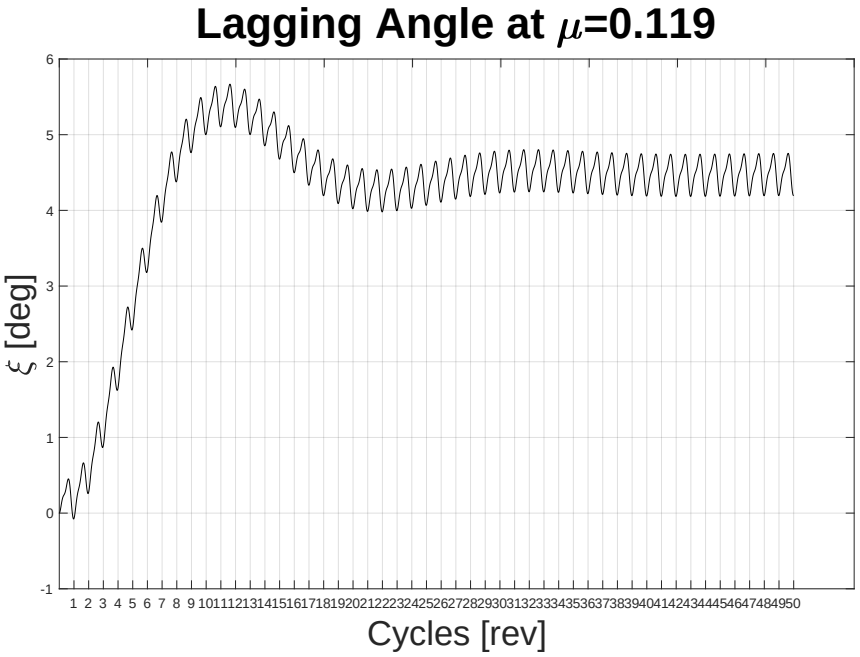

Figure C.14: Lagging angle at $\mu = 0.119$.

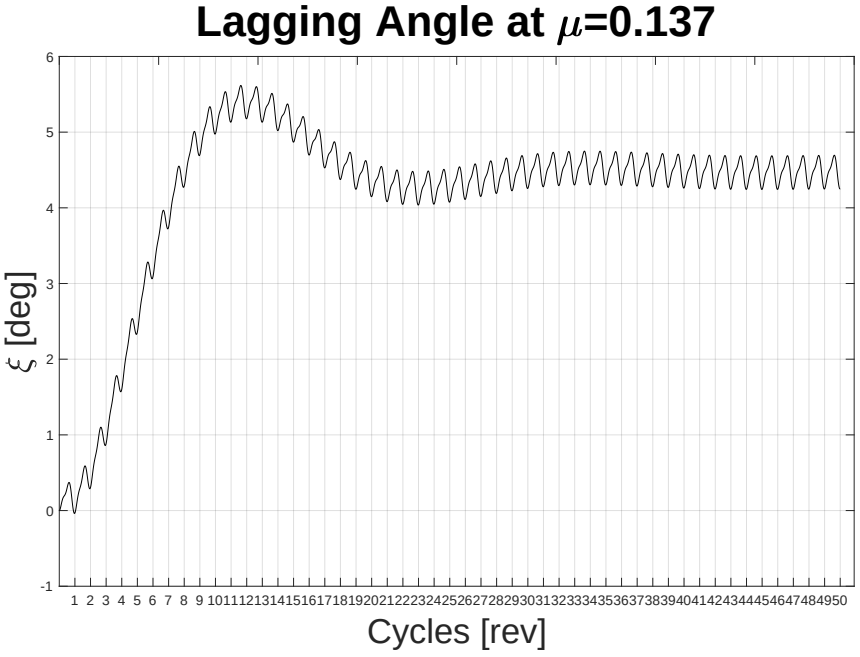

Figure C.15: Lagging angle at $\mu = 0.137$.

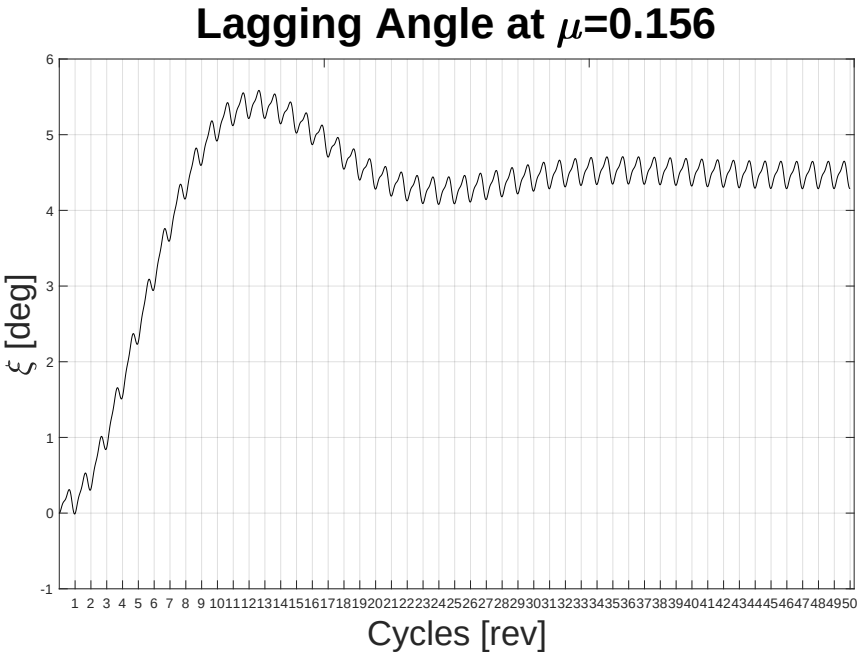

Figure C.16: Lagging angle at $\mu = 0.156$.

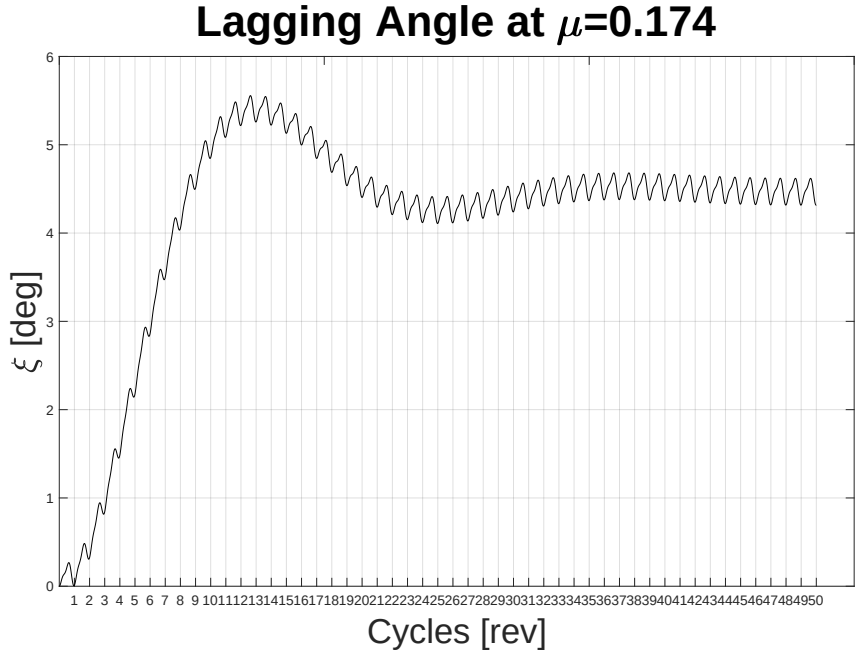

Figure C.17: Lagging angle at $\mu = 0.174$.

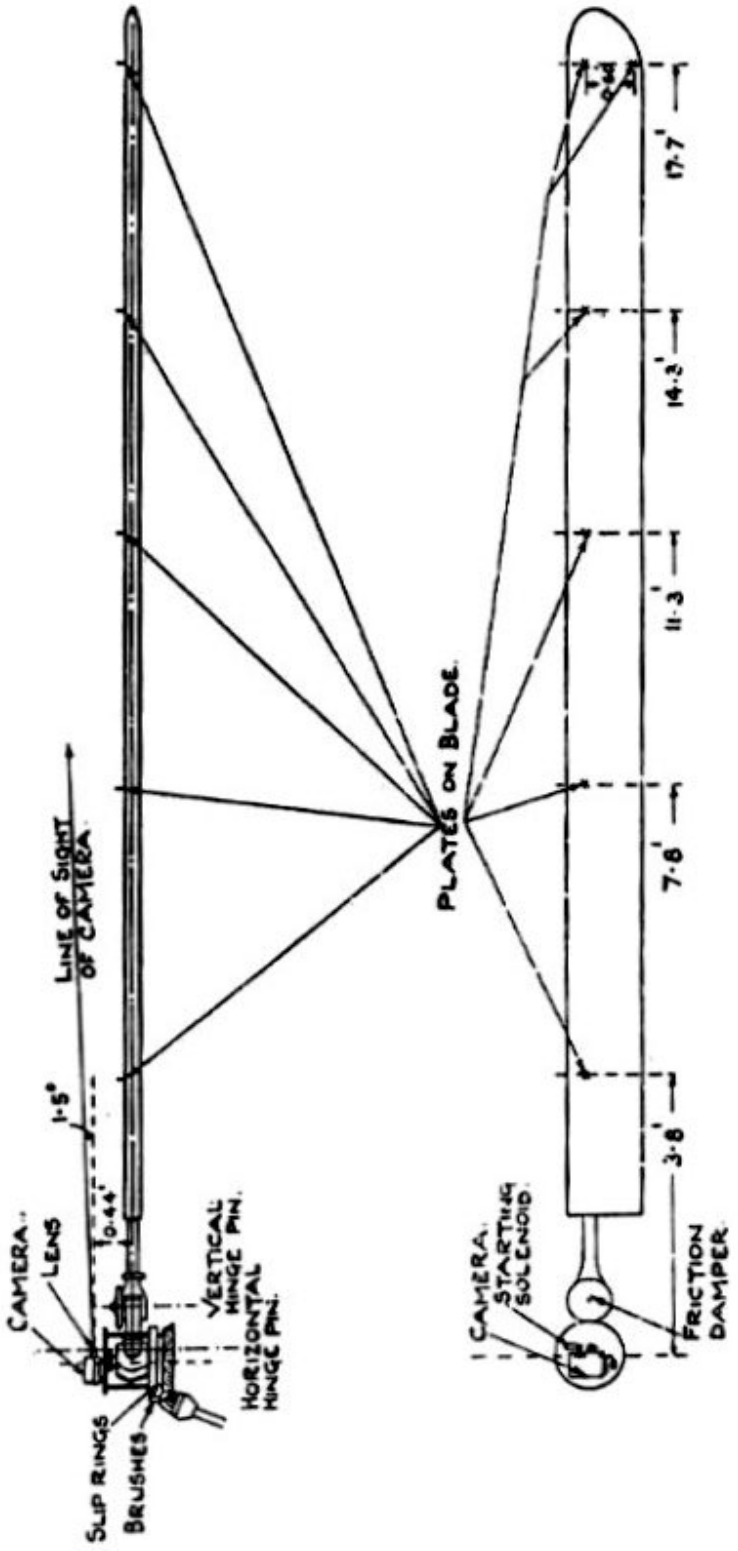

Figure C.18: Arrangement of ciné camera mount.

D Project Planning Appendix

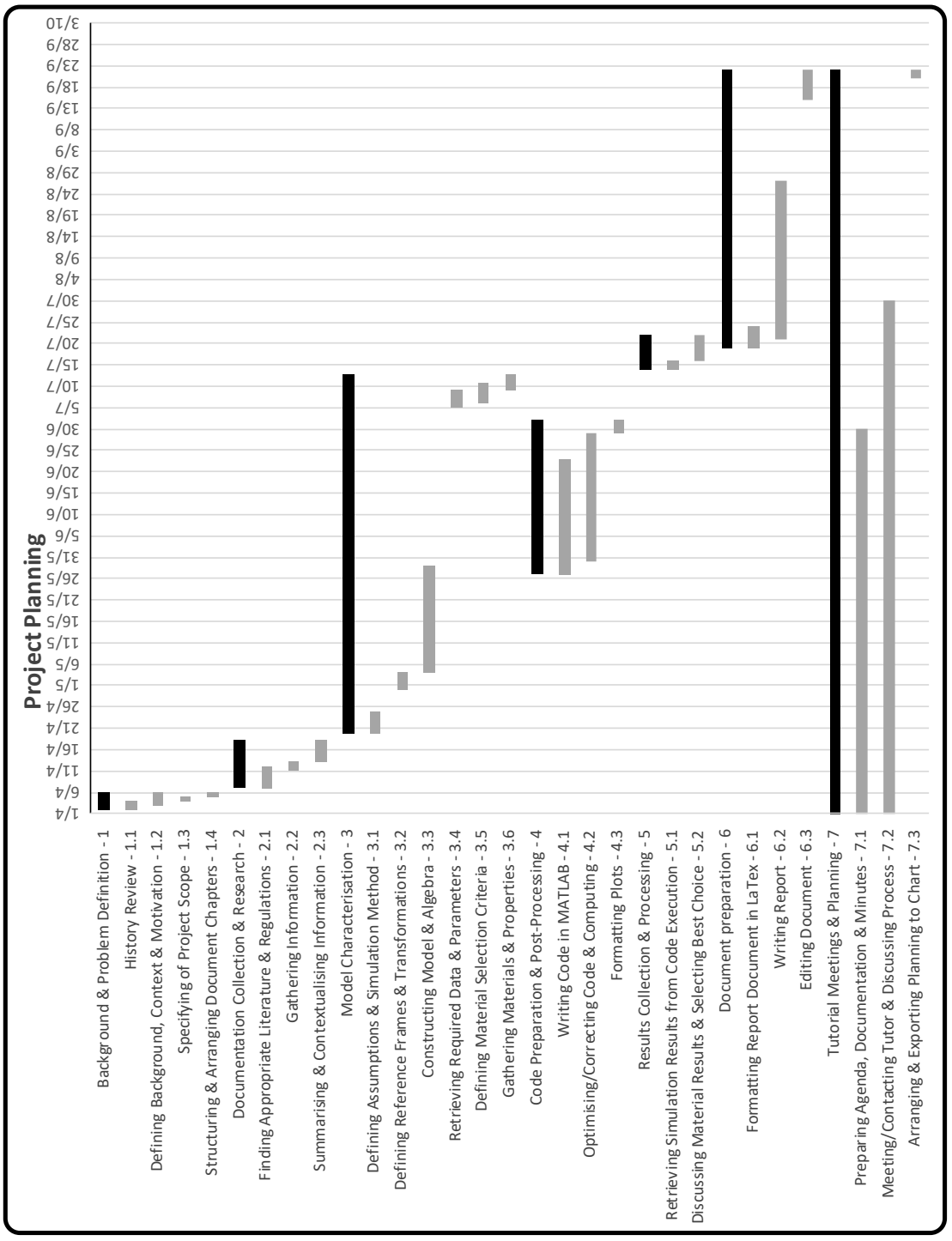

Figure D.1: Project planning and tasks distribution in time as a Gantt chart.